Motion prediction of a Semi-Submersible Crane Vessel at inconvenient draft

Identifying the cause of the discrepancies on an experimental basis

B.P.J. van der Kroft

TU Delft

MARINE CONTRACTORS

Motion prediction of a Semi-Submersible Crane Vessel at inconvenient draft

Identifying the cause of the discrepancies on an experimental basis

by

B.P.J. van der Kroft

to obtain the degree of Master of Science in the specialization of ship hydromechanics
at the Delft University of Technology,
to be defended publicly on Monday October 31, 2022 at 15:00.

Student number:	4565630	
Thesis number:	MT.22/23.009.M.	
Project duration:	November 15, 2021 – October 31, 2022	
Thesis committee:	Dr. Ir. P. R. Wellens,	TU Delft, chairman & supervisor
	Ir. A. D. Boon,	TU Delft
	Dr. Ir. H. J. de Koning Gans,	TU Delft
	Dr. R. M. Hartkamp,	TU Delft
	Ir. J. S. Bokhorst,	Heerema Marine Contractors, supervisor
	Ir. R. van Dijk,	Heerema Marine Contractors, supervisor

An electronic version of this thesis is available at `http://repository.tudelft.nl/`.

Cover image: Semi-Submersible Crane Vessel Sleipnir during transport of the Brent Alpha Jacket [4]

TU Delft

MARINE CONTRACTORS

Abstract

During specific operations, offshore marine contractor Heerema Marine Contractors reduces the draft of their Semi-Submersible Crane Vessel (SSCV) such that the floaters are submerged in close proximity to the free surface. This draft is also known as inconvenient draft. At this draft the motions of the vessel do not fully comply anymore with the computed prediction using linear diffraction theory. A proper motion prediction is required to ensure a safe execution of the offshore operation. The key issue is the submerged part of the floater, since discrepancies occur as soon as there is only a small water column on top of the floaters. Motion RAOs are computed via the hydrodynamic coefficients and wave loads. The reason why this leads to discrepancies in the motion RAO is not yet known. In addition, qualitative hydrodynamic data should be gathered for an object submerged in close proximity of the free surface.

Therefore, in this study the cause of the discrepancies in motion RAO is studied on an experimental basis for an object submerged in close proximity to the free surface. The scope is narrowed down to a two-dimensional cross-section of a SSCV-floater. Numerical simulations using linear diffraction theory are performed in WAMIT. The results are compared to experimental data obtained via model tests performed at the towing tank facilities at the faculty 3mE at Delft University of Technology.

Based on experimental data is concluded that linear diffraction theory does not predict physical phenomena that satisfy the boundary conditions and that underlie principles of the theory. Despite the fact that the experimental data does satisfy the boundary conditions of the numerical simulation, discrepancies occur at the hydrodynamic coefficients and wave load. As a result, it can be concluded that linear diffraction theory malfunctions at the inconvenient draft region, and therefore is not the correct theory to determine RAOs for an object on inconvenient draft.

Discrepancies in motion RAO are found to be dominated by the discrepancies the wave load, except for the frequency at which the added mass equals negative inertia of the body. Discrepancies for added mass are less significant than for the damping coefficient and wave load. At higher frequencies inertia becomes dominant over damping and damping deviations affect the RAO less.

The pitch motion about the center of the cross-section does not represent a rotational motion about same the degree of freedom for an SSCV. However, it allowed to experimentally investigate the global numerical extremes. In addition, it led to the finding that it seems that the rotational data is more affected than the heave data.

There is a strong suspicion that poles in the complex plane are the cause of the discrepancies in the hydrodynamic data, which result of the used Green's function by Wehausen and Laitone [36]. This suspicion is based on characteristics of the numerical data in combination with findings in literature and the experimental data, accumulate.

Currently, an approach that makes use of free surface damping is applied to predict the motion of an SSCV at inconvenient draft. Based on experimental data can be concluded that the use of free surface damping without further modifications does not result in an accurate motion prediction.

Lastly, the effect of nonlinearities when increasing the oscillation or wave amplitude. The wave load is found to be more prone to nonlinear effects than the hydrodynamic coefficients. The force signal remained dominantly harmonic, but higher harmonic forces did show up. Furthermore, with the exception of most tests at the largest tested submergence, higher harmonic waves were measured and visually observed during the tests. These higher harmonic waves arose at the transition from the shallow to deep water regime and vice versa. These forces were found to have hardly any effect on the force signal.

Preface

Throughout the course of my studies, it became clear that what fascinates me are vessels exposed to waves. The moment the topic about the motion prediction of an semi-submersible crane vessel came across, I knew this is the topic I want to graduate on. Almost a year after the start of the research, I am glad that I can finally present you my thesis with the topic: "Motion prediction of a Semi-Submersible Crane Vessel at inconvenient draft: Identifying the cause of the discrepancies on an experimental basis".

I could not have done this work without the help of a lot of people. I would like to thank Peter Wellens for being my supervisor and for offering me the possibility to develop and perform my own model tests. You were always open for discussion, and I enjoyed it to learn a lot from your enthusiasm and passion about hydromechanics. I also want to thank you for the effort you put in to make the model tests possible.

I would also like to thank Job Bokhorst and Radboud van Dijk from Heerema Marine Contractors for your supervision during the project. Your expertise in ship hydromechanics and model testing has taught me a lot. I have also learned a lot on from you on how to critically analyse findings and results. I am glad that I had the opportunity to perform my thesis in collaboration with Heerema Marine Contractors and want to thank all people I met there that helped me during my thesis.

The model tests could not have been performed without the help of Jasper den Ouden, Peter Poot, Anna Boon, Sebastian Schreier, Pascal Chabot, Frits Sterk and Jennifer Rodrigues Monteiro. Their expertise and knowledge on all topics related to conducting a model test has taught me a lot on this exiting journey. Also the help of Hugo Verhelst during the numerical analysis is highly appreciated. Furthermore, I want to thank Anna Boon, Henk de Koning Gans and Remco Hartkamp for taking place in my thesis committee.

Finally, I would like to thank my family, girlfriend and friends for their help and support not only during my thesis, but throughout the studies.

B.P.J. van der Kroft
Delft, October 24, 2022

Contents

List of Figures

List of Tables

Nomenclature

Abbrevations

BEM	Boundary Element Method
DoF	Degree of Freedom
HMC	Heerema Marine Contractors
RAO	Response Amplitude Operator
SSCV	Semi-Submersible Crane Vessel
2D	Two-dimensional
%D	Percent Deviation

Symbols

a	Added mass, heave: [kg], pitch: $[kgm^2]$
b	Damping, heave: $[\frac{kg}{s}]$, pitch: $[\frac{kgm^2}{s}]$
c	Restoring coefficient, heave: $[\frac{N}{m}]$, pitch: $[\frac{Nm}{rad}]$
d	Water depth [m]
e	Euler's number
$G(\vec{x}, \vec{\zeta})$	Green's function for potential located at $\vec{x}$ and source located at $\vec{\zeta}$
g	Gravitational constant $[\frac{m}{s^2}]$
H	Floater height [m]
I_{ii}	Mass moment of inertia in direction ii $[tonm^2]$
i	Imaginary number
J_0	Bessel function of the first kind of order zero
K	Deep water wavenumber $(\frac{\omega^2}{g})$ $[\frac{rad}{m}]$
k	Wavenumber $[\frac{rad}{m}]$
L	Floater length [m]
L	Arm of the applied moment [m]
m	Mass of the floater [kg]
$\boldsymbol{M}$	Mass matrix
$n_{panels,x}$	Number of panels over dimension x [-]
R	Horizontal distance to point of interest [m]
r	Bilge radius [m]
S_b	Body surface
$S_j(\omega)$	Variance density spectrum over frequency domain for variable j
s	Submergence [m]
T	Floater draft [m]
t	Time [s]
v_n	Velocity in normal direction of the body $[\frac{m}{s}]$
x	Displacement [m]
$\dot{x}$	Velocity $[\frac{m}{s}]$
$\ddot{x}$	Acceleration $[\frac{m}{s^2}]$
$\hat{x}$	Horizontal x-axis convention [-]
$\vec{x}$	Vector with directions (x,y,z)
x_a	Heave motion amplitude [m]
x_g	x-coordinate of center of gravity [m]
y_g	y-coordinate of center of gravity [m]
$\hat{z}$	Vertical z-axis convention [-]

z_g	z-coordinate of center of gravity [m]
Δ	Discrete stepsize between certain data points
ϵ	Free surface damping factor [-]
$\varepsilon_{a,b}$	Phase angle of the signal a relative to signal b $[rad]$
$\vec{\zeta}$	Vector with directions (ξ,η,ζ)
ζ_a	Wave amplitude [m]
θ_a	Pitch motion amplitude [°]
ϕ	Velocity potential $[\frac{rad}{s}]$
ω	Frequency $[\frac{rad}{s}]$
$\bar{\omega}$	Dimensionless frequency [-]

1 Introduction

A relatively new method for the transport of removed jackets or topsides, is to have them suspended in the cranes of a Semi-Submersible Crane Vessel (SSCV), instead of placing them on deck or a barge. This enables one to transport a large sized load in a single piece instead of multiple pieces. Besides the economic benefits, this method reduces the operating time offshore and thus improves the safety of the operation. Heerema Marine Contractors (HMC), a company specialised in transportation, installation and removal of offshore structures, uses this transport method frequently during operations nowadays.

For offshore operations, adequate prediction of the vessel's motion is important to determine the limiting sea states. The use of crane suspended transport offers the possibility to transport a relatively large sized load, see Figure 1.1a. Consequently, the draft of the vessel is such that the floaters are submerged relatively close to the water surface. This is called inconvenient draft and is schematically represented in Figure 1.1b. An SSCV can also be at inconvenient draft when lifting objects in shallow water. At inconvenient draft, it turns out that the motions of the vessel no longer fully comply with the prediction using linear diffraction theory.

(a) During crane suspended transport [4]

(b) Schematic view

Figure 1.1: Semi-Submersible Crane Vessel at inconvenient draft

1.1. Heerema Marine Contractors

Heerema Marine Contractors is a leading marine contractor in the offshore industry, specialised in the transportation, installation and removal of offshore-structures. Their fleet currently has three Semi-Submersible Crane Vessels; Balder, Sleipnir and Thialf. During offshore operations, they make use of crane suspended transport to be able to transport single pieced loads and therefore reducing the operating time offshore. As shown in Figure 1.1, the vessels often sail at inconvenient draft.

1.2. Problem statement

It is important to predict the motion response amplitude operator (RAO) correctly as the transformation of the incoming wave spectrum to predicted motion spectrum is a multiplication by the RAO squared. A background on this translation is given in subsection 1.3.3. In Figure 1.2, numerical results for an SSCV at inconvenient draft are compared to data retrieved from model tests. The numerical analysis is done in the commercial programme WAMIT. In both the heave and roll RAO, discrepancies can clearly be seen. Over the frequency domain, motions are mainly overestimated, but some clear underestimations, such as at 0.5 $\frac{rad}{s}$ in heave, also stand out. It is unknown what the cause of the deviations is, except for the suspicion of nonlinearities. However, these discrepancies are more severe than only nonlinearities.

Currently, the problems with overestimated motions are being tackled by the use of free surface damping, which is a feature in the used diffraction analysis program WAMIT. This theory will be explained in section 1.4. These results were validated against data from the Thialf that was computed by expensive model tests and computational fluid dynamics calculations performed by MARIN. These tests have been done only at one depth and that data got extrapolated to other depths, including a safety factor. While this seems to be a conservative approach, HMC seeks to better understand the discrepancies between the predicted motions from calculations and (full) scale measurements.

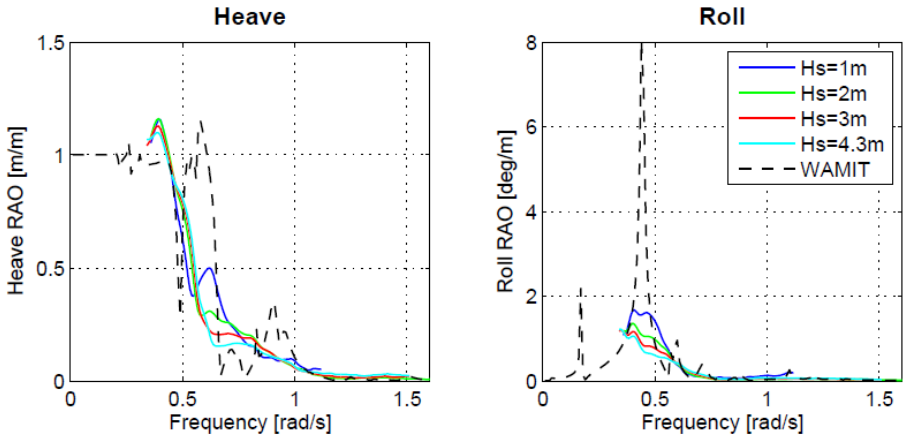

Figure 1.2: RAO for an SSCV at inconvenient draft in beam waves comparing model test data to numerical predictions

1.3. Theoretical background

Motion analysis of a vessel waves is normally done using a potential flow boundary element method to determine the RAOs under the assumption that the system in linear. In this method the Green's function an important function. The response in irregular waves can then be predicted via a spectral translation of the wave spectrum.

1.3.1. Potential flow method

Currently, a potential flow panel method is applied within HMC to calculate the motions of a vessel via the commercial package WAMIT. A potential flow is characterised by the assumption that it is an irrotational, inviscid, incompressible flow and is also known as an ideal flow. The gradient of potential function ϕ is the velocity vector field. As small motions and harmonic waves are assumed, the system can be linearized. The linear fluid potential can be split in three parts, a radiation potential, a diffraction potantial and an undisturbed wave potential. Due to the incompressibility assumption, the conservation of mass is satisfied by the Laplace equation as given in 1.1. The general solution of a Laplacian is a harmonic function.

$$\nabla^2\phi = \frac{\partial^2\phi}{\partial x^2} + \frac{\partial^2\phi}{\partial y^2} + \frac{\partial^2\phi}{\partial z^2} = 0 \tag{1.1}$$

There are several boundary conditions to be met to represent the desired situation. At the free surface the atmospheric pressure should be equal to the pressure of the fluid. On top of that, the vertical velocity of a particle at the free surface is equal to the vertical velocity of the free surface. Due to the linearisation, these boundary conditions can be combined and represented as shown in Equation 1.2.

$$\frac{\partial^2 \phi}{\partial t^2} + g\frac{\partial \phi}{\partial z} = 0 \quad \text{at } z = 0 \tag{1.2}$$

Solid surfaces such as the sea bottom and the body surface cannot be penetrated. Therefore the velocity in normal direction of the surface should be zero at the surface. At the sea bottom, with water depth d, this results in Equation 1.3. For the body surface Equation 1.4 can be applied, in which v_n is the velocity of the body in normal direction.

$$\frac{\partial \phi}{\partial z} = 0 \quad \text{at } z = -d \tag{1.3}$$

$$\frac{\partial \phi}{\partial n} = v_n \tag{1.4}$$

Far from the body the surface does not feel the presence of the studied body due to energy dissipation, which is satisfied using Equation 1.5. R is the horizontal distance between the body and the point of interest.

$$\lim_{R\to\infty} \phi = 0 \tag{1.5}$$

1.3.2. Green's function

The boundary value problem described in subsection 1.3.1, can be solved using a boundary element method (BEM) by dividing the body surface into panels. A pulsating point source is placed in the middle of each panel. The source strength of each source for each mode can be solved using Green's theorem as shown in Equation 1.6. Here, $G(\vec{x},\vec{\xi})$ is the Green's function; a mathematical function to determine the velocity potential at point $\vec{x}$ due to a point source located at point $\vec{\xi}$. The Green's function satisfies the linearised boundary conditions. Therefore, panels only need to be placed on the body surface S_b. The velocity potentials are used to calculate the added mass, potential damping and wave loads via a pressure integration. Background on the Green's function and the conversion of velocity potentials to hydrodynamic data is given in Appendix A.

$$\phi_i(\vec{x}) + \iint_{S_b} \phi_i(\vec{\xi}) \frac{\partial G(\vec{x},\vec{\xi})}{\partial n_\xi} d\vec{\xi} = \iint_{S_b} \frac{\partial \phi_i}{\partial n} G(\vec{x},\vec{\xi}) d\vec{\xi} \tag{1.6}$$

There are several possible alternatives for the Green's function for potential flow boundary element methods. The Green's function implemented in WAMIT, and thus used during this analysis, is based on the work of Wehausen and Laitone [36]. Robertson [29] found that there are regions for which no such function exists as they are hard to obtain and not universal due to their dependency on the boundary conditions.

Method of images

Potential flow methods use a combination of sources and sinks to model flow fields. A sink is a source with a negative strength. Obstacles, such as a solid wall, cannot be modelled directly with sources. To model a wall, a source is placed exactly mirror-inverted to the other side of the artificial wall. In this way, a flat surface streamline is created to represent the wall [37]. A graphical representation of this example can be found in Figure 1.3. This method is called the method of images.

The Green's function for infinite depth, defined in the work of Wehausen and Laitone [36], is shown in Equation 1.7. This version is less complex than the version for finite water depth. Since discrepancies are caused by the small layer of water on top of the floater, the problem can already be analysed using the Green's function for infinite water depth [8, 19, 26]. A derivation for both the finite as infinite water depth function is given in Appendix A. The first two terms in the Green's function represent the original and imaged source, which is confirmed by Newman [23] and is graphically represented in Figure 1.4 in which $r = \sqrt{(x-\xi)^2+(y-\eta)^2+(z-\zeta)^2}$ and $r' = \sqrt{(x-\xi)^2+(y-\eta)^2+(z+\zeta)^2}$, since $(z+\zeta)^2 = (-\zeta - z)^2$. This means that at the low frequency limit, the free surface is represented as a solid wall. The third term represents takes into account the free surface boundary conditions. Wave number k and deep water wave number K, equal to $\frac{\omega^2}{g}$, are the frequency dependent terms. Symbols ω and g are the frequency in $[\frac{rad}{s}]$ and gravitational constant. J_0 is a Bessel function of the first kind of order zero.

$$G(\vec{x},\vec{\xi}) = \underbrace{\frac{1}{\sqrt{(x-\xi)^2+(y-\eta)^2+(z-\zeta)^2}}}_{\text{Original source}} + \underbrace{\frac{1}{\sqrt{(x-\xi)^2+(y-\eta)^2+(z+\zeta)^2}}}_{\text{Imaged source}} + \underbrace{\frac{2K}{\pi}\int_0^\infty \frac{e^{k(z+\zeta)}}{k-K} J_0(kR)\, dk}_{\text{Free surface b.c.}} \tag{1.7}$$

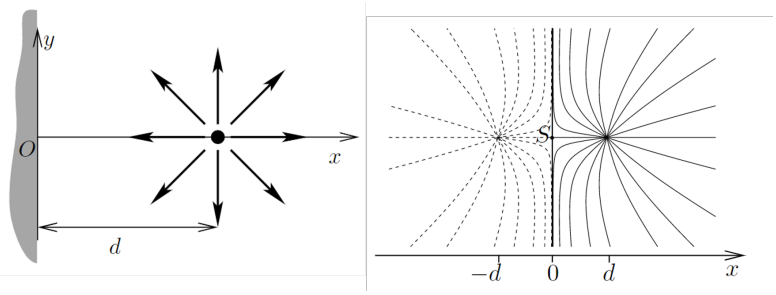

Figure 1.3: Implementation of the method of images for a point source placed near a wall [16]

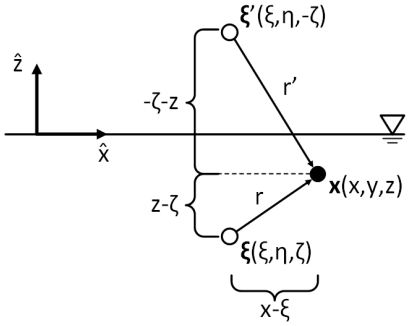

Figure 1.4: Graphical representation of the construction of the first two terms in the Green's function with point source $\vec{\xi}$, point $\vec{x}$ and imaged source $\vec{\xi}'$

There are several variants Green's function for the purpose of a body in waves. Another way to determine the unknown potentials is by the use of a Green's function based discrete eigenfunction expansion is by John [14]. However, at infinite depth this would become inefficient and the use of the Green's function by Wehausen and Laitone [36] is advantageous and mostly used [22].

1.3.3. Motion prediction in irregular waves

Motion behaviour of a vessel in irregular waves can be predicted by a spectral transformation. Over the years a lot of wave data has been gathered. The data of wave records at a specific site can be statistically described in a variance density spectrum. This is done using a Fourier Series Analysis. Multiplying the variance density spectrum $S_zeta(\omega)$ with the density and gravitational constant, will result in the energy density spectrum, therefore a variance spectrum is a good representation of the energy distribution of a wave record [10]. The variance density spectrum can be described using Equation 1.8. In case of regular waves, only one peak would be seen in the spectrum.

$$S_\zeta(\omega)\,d\omega = \frac{1}{2}\zeta_a^2(\omega) \tag{1.8}$$

The motion response spectrum of a vessel can be determined by combining the known wave spectrum and RAO of the desired degree of freedom (DoF). The definition of the motion response spectrum is the same as the definition of the wave spectrum only the wave amplitude ζ_a is replaced by the motion amplitude of the desired DoF. The derivation for calculating the spectrum transformation is given in Equation 1.9 [15]. A combination of the definitions of RAO, which is the motion amplitude over wave amplitude, and wave spectrum, lead to the transfer function for spectral transformations in Equation 1.10.

$$S_x(\omega)\,d\omega = \frac{1}{2}z_a^2(\omega) = \frac{1}{2}\left(\frac{x_a(\omega)\zeta_a(\omega)}{\zeta_a(\omega)}\right)^2 = RAO^2(\omega)\cdot\frac{1}{2}\zeta_a(\omega)^2 = RAO^2(\omega)\cdot S_\zeta(\omega)\,d\omega \tag{1.9}$$

$$S_x(\omega) = RAO^2(\omega)\cdot S_\zeta(\omega) \tag{1.10}$$

1.4. Gap analysis

The use of linear potential flow BEM, also known as diffraction theory, is a quick and efficient method to calculate RAOs of a floating or submerged vessel. Jiang et al. [13] and Van Santen [32] have shown that this method is applicable for the motion prediction of semi-submersibles at design draft. However, in research by De Bruijn et al. [6], Hong et al. [11], Ottens and Pistidda [27] and Van Winsen et al. [33], it is concluded that diffraction theory overpredicts the motions and wave loads of a semi-submersible at inconvenient draft. nonlinearities and unrealistically high water elevations are given as a cause of the discrepancies between diffraction theory results and model test results. However, the results also do not show a suitable approximation for motions which are still in the linear domain.

A modification on the theory by applying an artificial damping lid on the free surface by using the work of Chen [2] and Newman [25] still did not provide the correct answers. This damping lid is based on the French researcher Guével who assumes a fairly perfect fluid. This is an inviscid and irrotational fluid that has

a fictitious internal force proportional to the velocity of the fluid in opposite direction. The implementation of this fairly perfect fluid results in an adjustment to the free surface boundary condition, given in Equation 1.2. The adjusted version is given in Equation 1.11. It should be noted that, for this theory to be true, the value for damping lid ϵ must be small as such that it represents a small proportion of the fluid velocity. Note that this artificial damping lid is designed for side-by-side structures, which is a different situation than submerged structures.

$$\frac{\partial \phi}{\partial z} - \frac{\omega^2}{g}\phi - i\epsilon\frac{\omega^2}{g}\phi = 0 \quad \text{at z=0} \tag{1.11}$$

Research on more general bodies, instead of SSCVs or other vessels, mainly took the hydrodynamic coeffients into account. From studies by Chung [3], Farina [8], McCauley et al. [19], McIver and Evans [21] and Newman et al. [26], it can be concluded that negative added mass can occur for bodies submerged in close proximity to the free surface due to the contribution of the potential energy in the free surface. Despite the several approximations, they still conclude that computing the correct hydrodynamic coefficients is a challenge. They also acknowledge that nonlinearities can cause discrepancies, but mention the effects of the physical free surface as well.

Current literature shows that the different designed, adjusted, and used models cannot compute the right hydrodynamic coefficients and wave loads, and thus motion RAOs. There is no thorough research yet on why diffraction theory and other theories are not capable to compute correct answers and which assumptions are not met. A clear boundary when discrepancies start to occur has not been defined. All of this has not been researched on a floater without surface piercing columns.

Besides that, current research on SSCVs mainly focusses on RAOs and wave loads and does not specifically take hydrodynamic coefficients into account. Research on submerged bodies mainly focusses on hydrodynamic coefficients. However, there is no research available yet including both hydrodynamic coefficients and wave loads for a body in close proximity to the free surface that does not contain surface piercing elements. In addition, current research often has either a mathematical focus or a physics focus. Elaborating on both perspectives extensively in order to relate them to each other has not been done either.

1.5. Research question

The motions of an SSCV at inconvenient draft can not be predicted correctly yet. In previous research, several attempts have been done to compute the hydrodynamic data correctly for a body at inconvenient draft. Most research has been conducted on semi-submersible structures with a focus on the motion and wave force RAOs. In that way, the results are a combination of a surface piercing part, the vessel's columns, and a fully submerged part which is the floater. Hydrodynamic coefficients have mainly been investigated on a submerged cylinder or plate. Though, these are mainly quantitative results on the shape and behaviour of the data over frequency domain. There is not a lot of data available yet on the hydrodynamic coefficients for a body in close proximity to the free surface.

As explained in the gap analysis, section 1.4, there is no research yet that takes the hydrodynamic data, which is both hydrodynamic coefficients and wave loads, into account. The correct hydrodynamic data can be converted to motion RAOs when taking the correct equation of motion into account. To gain a better understanding of the discrepancies in motion prediction of an SSCV at inconvenient draft, qualitative hydrodynamic data should be gathered and an explanation on why the current motion prediction method shows deviations to reality should be developed. The main interest lies in the submerged part of a Semi-Submersible Crane Vessel. This all leads to the following research question for this study:

> "What is, based on experimental data, the cause of the discrepancies in motion RAO calculated using linear diffraction theory for an object submerged in close proximity to the free surface?"

Objectives have been defined of which, once performed, the results will lead to an answer of the research question.

1. Numerical modelling of the body using linear diffraction theory
2. Perform model tests to retrieve data for the added mass, damping and wave loads, which can be converted to RAO data
3. Compare the model test results to the outcome of the numerical simulations in linear diffraction theory.

4. Compare both numerical and experimental results of the hydrodynamic data and surface elevation to findings in literature.
5. Analyse the validity of the assumptions made and propose a method to become able to model the water column on top of the floater correctly.

1.5.1. Motivation

The execution of this project is relevant for both science and society.

The scientific contribution is that a next step will be taken into the understanding of hydrodynamic coefficients. By taking a fundamental approach the outcome is more widely applicable then just a specific type of vessel. Furthermore, if this research turns out to be effective, a lot less computational intensive CFD calculations or expensive and time consuming model tests have to be done. Besides, with CFD software problems occur when bodies emerge, a phenomenon that can occur at inconvenient draft as well.

The scientific contribution is that a next step will be taken into the understanding of the motion behaviour of an object at inconvenient draft. By taking a fundamental approach the outcome is more widely applicable then just a specific type of vessel. In this study a data set is generated which can be used as input for other studies. In addition, the limitations of linear diffraction theory will be better defined.

The most important societal contribution is that the safety onboard improves if the motion prediction improves. Hazards due to uncertainties in the vessels motion are then mitigated. Furthermore, the operational window of a vessel can be extended as a result of improved motion prediction, which increases the productivity and efficiency of the vessel. It can also result in bigger objects being able to be installed, which is very useful in the renewable energy markets where wind turbine sizes are still growing. The capabilities of vessels such as SSCVs can be better utilised. Future vessels can be designed more optimal by knowing what its lifetime will bring better. The outcome of this study is also applicable to other types of semi-submersibles.

1.6. Methodology and research outline

In order to achieve the goal of this research, a focus is placed on the key issue; the thin water layer on top of the floater. Therefore, the studied body will be a submerged floater instead of a complete SSCV. This way, no other effects occur from surface-piercing elements such as for instance columns.

Next to that a two-dimensional (2D) approach is applied, meaning that a cross-section of the floater is studied. Advantage of a 2D-approach is that it reduces the amount of DoF from six to three. The DoFs left can all give a different insight into the problem. Based on literature, it turns out that especially heave and pitch contribute to inconvenient draft phenomena. Therefore, surge will be left out of this research. A two-dimensional approach is less complicated and therefore easier to understand. In addition, the core of the problem can still be tackled, which makes the translation to 3D-domain easy to achieve later on.

First, the setup of the numerical simulations is discussed in chapter 2. The simulations are performed in WAMIT, a linear potential flow BEM solver. Then the model test setup is elaborated on in chapter 3. In this chapter the post-processing, experimental uncertainties and the sensitivity of the setup are discussed too. Both forced oscillation and captive tests have been performed to retrieve data on the hydrodynamic coefficients and wave loads. Model tests have been performed at the towing tank facilities at Delft University of Technology.

In chapter 4, the experimental results are compared to the numerical results. The observations and data from the model tests are analysed and a look is taken at the underlying principles of the linear diffraction theory, including free surface damping. The conclusions of the study are noted in chapter 5. Lastly, recommendations for further research is listed in chapter 6.

2

Numerical modelling using linear diffraction theory

In order to understand the shortcomings of diffraction theory for a body at inconvenient draft, a thorough numerical analysed is performed. In this chapter, the simulation setup for numerically modelling the submerged cross-section of the floater, as depicted in Figure 2.1, is discussed. Simulations are performed using the commercial package WAMIT [34].

First the simulation setup is discussed in section 2.1. A sensitivity analysis is stated in section 2.2. Both the effects of frequency and grid refinement are identified. The results of a parameter study are stated in section 2.3. The chapter will end with the simulation plan in section 2.4.

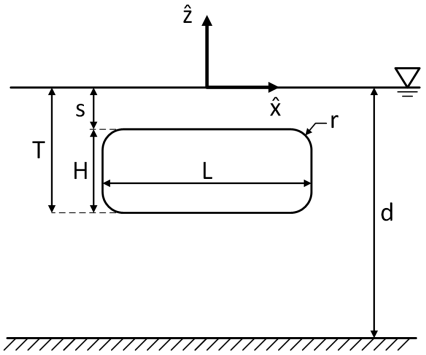

Figure 2.1: Schematic view of the modelled floater cross-section where L = 33.75 m, H = 13.5 m, radius r = 1.016 m and s is variable, water depth d = 48 m

2.1. Simulation setup in WAMIT

The modelled situation is comparable to the full scale version of the testing facilities at Delft University of Technology. This results in a water depth d of 48 m. A schematic representation of the cross section is given in Figure 2.1. The dimensions of the floater are derived from the floater dimensions of the SSCVs of HMC. The length L of the floater is 33.75 m and the height H is 13.5 m, the floater has bilge beams with a radius of 1.016 m. The draft T is variable. The draft is composed of the floater height and the submergence s. Since the submergence s is equal to the water column on top of the floater, in which the research interest lies, the vertical position of the floater is referred to in submergence s. The submergence range studied is from 0.5 to 5 m.

The simulated frequency domain is simulated is 0 to 2.05 $\frac{rad}{s}$. This covers the waves having a wave period longer than 3 seconds. During operation, SSCVs are mainly affected by 5 to 20 second waves, which are equivalent to 1.26 to 0.31 $\frac{rad}{s}$ waves. The frequency range also includes lower frequent swell waves and an extended range of wind waves.

The mesh created is symmetrical about the x and z axes. A total of 2280 panels are is used, which is elaborated on in the grid refinement study in section 2.2. Due to the relatively square shape of the object, square panels are easily created. However, the bilge radii require a more detailed description due to the round shape. The circular structure is created by dividing panels of equal length along the arc length of the bilge. The exact distribution of the panels is further discussed in the grid refinement study.

Originally, WAMIT is a programme designed for a three-dimensional environment. Currently, a two-dimensional situation is being studied. Since WAMIT does not include the ability to perform a 2D analysis, the effects into the third dimension should be excluded. Ideally, this is achieved by giving the structure an infinite width. However, this leads to very high computation times due to the large number of panels. A more practical solution is to model a channel with perfect reflections around the model, which is just a fraction

wider than the model. A check is done to see whether this method provides proper results. Four runs are performed of which in three runs the floater has been modelled with a different width in open water, and in the fourth run a channel with a width of 150.1 m was created around the model, which is 0.1 m wider than the model. The channel has a perfect reflection coefficient, so there is no friction or unwanted disturbance. The results are shown in Figure 2.2. A wider model leads to a smoother prediction with smaller extremes. Eliminating the third dimension makes the resulting curve even smoother. The application of a channel provides relatively comparable results to the situation with 1000 m width. On top of that, it better represents the situation during the model tests and saves computation computational time. Therefore, all simulations are performed with will be ran having a channel surrounding the model in the zx-plane.

The used mesh is visualised in Figure 2.3 and intentionally has open sides. The ends of the floater are parallel to the zx-plane, therefore these have no contribution to the considered DoFs in the two-dimensional situation, being heave and pitch. The first reason that they are omitted is that numerical deviations occur in the RAO at low frequencies when both sides and a channel are included in the simulation compared to the simulation without sides. This numerical deviation is probably due to the fact that the panels no longer have a rectangular shape at the bilges. The second reason is that it also saves a considerable number of panels and therefore computational time.

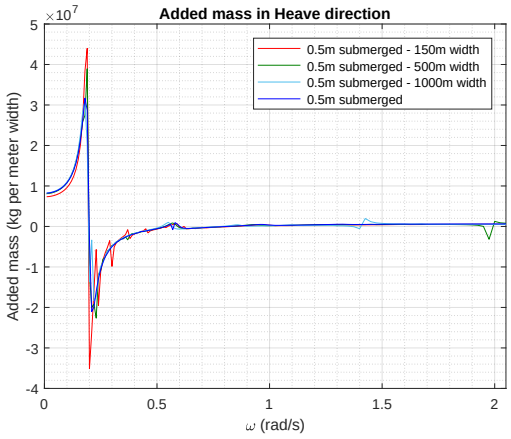

Figure 2.2: Results of adjustments of a 3D analysis to simulate a 2D analysis

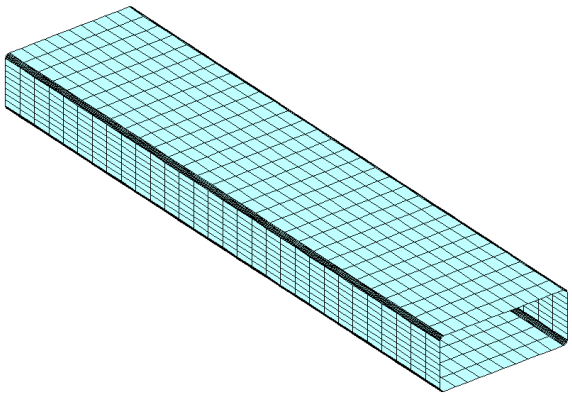

Figure 2.3: Visualisation of the used mesh

Lastly, the input for the body mass and center of gravity are required. This only affects the RAO, because the added mass, potential damping, and wave loads depend only on the shape of the object. The input is given for a submergence of 0 m with the origin of the coordinate system on the free surface, as shown in Figure 2.1. The submergence can be adjusted in the input of WAMIT, after which the program adjusts the center of gravity and the mass matrix itself. The center of gravity is positioned at the middle of the floater cross-section, which is also the center of buoyancy. This results in a rotation for the pitch motion about the center of the cross-section, which is not comparable to the pitch motion of a SSCV. Due to the chosen convention for the numerical analysis, what is referred to as pitch motion in this study is actually roll motion for a SSCV. The point of rotation about which a SSCV rolls is between the two floaters, resulting in a heave motion of both floaters in opposite directions. However, a pure pitch motion is chosen to investigate whether the effects are comparable to the heave or whether other interesting aspects can be observed.

The coordinates of the center of gravity $[x_g, \quad y_g, \quad z_g] = [0, \quad 0, \quad -\frac{H}{2}]$ and are used in the mass matrix. The mass is equal to the mass of the displaced volume, thus the volume of the box times the water density of 1000 $\frac{kg}{m^3}$. The model mass is 68211 ton. Mass matrix $\boldsymbol{M}$ is given in Equation 2.1, in this matrix I_{ii} equals the mass moment of inertia calculated with Equation 2.2 where x_1, x_2 and x_3 are respectively x, y and z. Values for the mass moments of inertia are I_{11} = 132039125 $tonm^2$, I_{22} = 10581581 $tonm^2$ and I_{33} = 134370017 $tonm^2$, where I_{22} is important for the pitch motion.

$$\boldsymbol{M} = \begin{pmatrix} m & 0 & 0 & 0 & mz_g & -my_g \\ 0 & m & 0 & -mz_g & 0 & mx_g \\ 0 & 0 & m & my_g & -mx_g & 0 \\ 0 & -mz_g & my_g & I_{11} & 0 & 0 \\ mz_g & 0 & -mx_g & 0 & I_{22} & 0 \\ -my_g & mx_g & 0 & 0 & 0 & I_{33} \end{pmatrix} \tag{2.1}$$

$$I_{ii} = \int x_i^2 dm \tag{2.2}$$

2.2. Sensitivity analysis

By using a panelled BEM, both the space and time scales are discretized. It is important to understand the consequences of discretization, especially since rapid fluctuations are expected in the data.

First, the refinement in the time domain. Usually, creating a data point every 0.025 $\frac{rad}{s}$ is sufficient to obtain a detailed enough description of the motions of a SSCV in the frequency domain. To see what the effect of a refinement, frequency steps of 0.01 and 0.005 $\frac{rad}{s}$ are also considered. This refinement should better reflect the rapidly changing peaks and troughs in data. This is seen reflected in the results in Figure 2.4.The disadvantage of a smaller frequency step is that the computation time increases significantly. The results show that a description with a frequency step of 0.025 $\frac{rad}{s}$ is too coarse to describe the extremes properly. A frequency step of 0.01 $\frac{rad}{s}$ gives almost the same results as a frequency step of 0.005 $\frac{rad}{s}$, while saving a significant amount of computation time. Note, however, that the finest frequency step gives a slightly higher peak around $\omega = 0.20$ $\frac{rad}{s}$, and thus a somewhat more detailed representation. Nevertheless, with the slightly coarser frequency step of 0.01 $\frac{rad}{s}$, a proper detailed representation of the data is given and the core of the problem is captured.

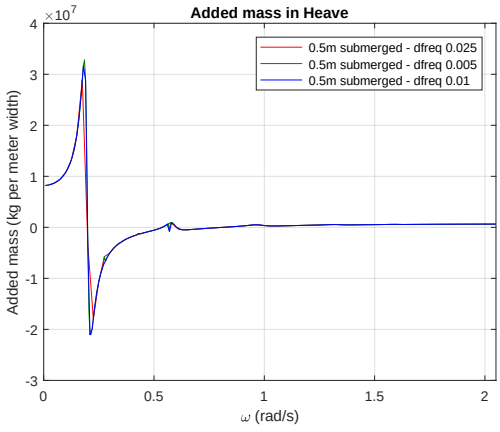

Figure 2.4: Refinement in frequency steps

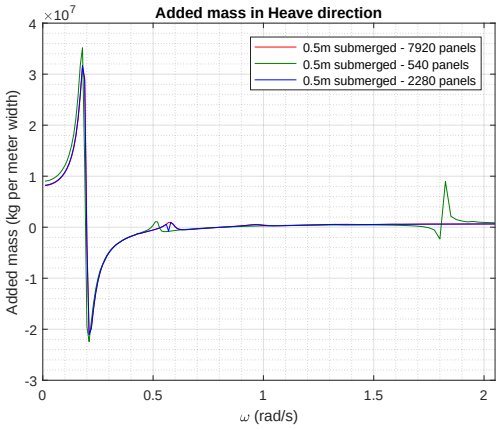

Figure 2.5: Grid refinement results for added mass in heave directions of mesh 540, 2280 and 7920 panels using $\Delta\omega = 0.01$ $\frac{rad}{s}$

Similar to frequency refinement, results are sensitive to mesh refinement. To examine the effect of grid refinement, a coarse, a medium, and a refined mesh with 540, 2280, and 7920 panels are considered. The distribution of panels for each mesh is given in Table 2.1. The number of panels in the radius is distributed over an arc length of 1.60 m. For the coarse mesh, the description of the bilge is fairly angular, for the medium and fine mesh a circular structure is more and more adopted. The number of panels in length, $n_{panels,length}$, is the number of panels in the zx-plane in the horizontal direction between the radii. The number of panels in the vertical direction between the radii is given by $n_{panels,height}$ and over the third dimension, width, by $n_{panels,width}$. Immediately noticeable in the results shown in Figure 2.5, is that on the coarse grid shows an offset in the low-frequency region up to the peak of the added mass compared to the medium and fine mesh. This is likely due to the angular representation of the bilges in the coarse mesh, as these are described with only 5 panels each. The other deviating parts of the graph are as well due to the angular representation. There are not many differences between the medium and fine meshes, except at 0.55 $\frac{rad}{s}$. Here, the distortion seen

in results of the medium mesh has become a smoother line at the finest mesh. Since, as with frequency refinement, a proper representation of the result of the numerical BEM is obtained, and insights can be gained with a medium mesh of 2280 panels, which is shown in Figure 2.3, the medium is used instead of the much more time-consuming fine mesh.

Table 2.1: Mesh description including accompanied panel distribution for mesh refinement study

Mesh	$n_{panels,radius}$	$n_{panels,length}$	$n_{panels,height}$	$n_{panels,width}$	$n_{panels,total}$
Coarse	5	4	4	15	540
Medium	10	10	8	30	2280
Fine	15	20	16	60	7920

2.3. Parameter study

A parameter study has already been performed by Van Winsen et al. [33]. They concluded that the submergence height over the horizontal length of the top plate is most important, and that discrepancies occur as soon as there is a submergence height. The latter conclusion was also made by Martin and Farina [18], who, among others, studied only a very thin submerged plate or disc. Thus, the height H does not affect the problem. It only affects the shape of the floater and accompanied change in mass and inertia. It is also possible to adjust length L and remain the same submergence s. However, this leads to an inconvenient situation when performing model tests, and in reality one changes the draft and cannot change the length of a body. By adjusting radius r, the effective length of the floater is altered. By effective length L_{eff} is meant the flat part of the top which is equal to L minus $2r$. Thus, the fraction $\frac{s}{L_{eff}}$ decreases as the radius increases, resulting in smaller extreme values in the motion RAO at constant submergence.

Van Winsen et al. [33] also found that reducing the water depth leads to lower peak values and even no peak value of wave load in extremely shallow water. This is a result of the elliptical trajectory of the fluid particles. For waves in deep water, the fluid particles flow on a circular trajectory, which becomes elliptical in shallow water due to the presence of the bottom. An elliptical trajectory reduces the vertical velocity of the fluid particles, and thus a smaller potential in the vertical direction [10]. A smaller potential leads to a smaller output for the wave loads and hydrodynamic coefficients, which makes it understandable that peaks can become smaller. The findings in literature from this parameter study were also been observed in the performed numerical simulations.

2.4. Simulation plan

The numerical simulations have several purposes. These are to acquire data to compare with the model test results. To gain insight in the impact on the hydrodynamic data by adjusting the submergence. To confirm or deny this impact based on the findings in the literature to eventually find why linear diffraction theory cannot generate the correct hydrodynamic data for a body at inconvenient draft.

Simulations were run over the submergence range of 0.5 to 5 m with a submergence step of 0.5 m over a frequency range of 0 to 2.05 $\frac{rad}{s}$. The simulation where the floater is surface piercing is not run, as the deviations are caused by water column on top of the floater. A maximum depth of 5 m submergence is used because from this depth the potential theory is believed to give correct results.

A look is taken at the effect of free surface damping, which is part of current practice for predicting SSCV motions at inconvenient draft. Simulations were run for the smallest submergence with multiple damping coefficients, providing the clearest insights in the effect of surface damping

3

Experiments

Model tests have been performed to obtain data for hydrodynamic coefficients and wave loads of a submerged body in close proximity to the free surface. A data set is created to learn to understand what happens physics wise in reality and to compare to the results of the numerical simulations. Forced oscillation tests are done performed to obtain data for the hydrodynamic coefficients, and the measured data in captive tests is used for the wave loads.

In this chapter, first the experimental setup is discussed in section 3.1. After that, the test method and programme are explained in section 3.2. The post-processing procedures for the measured data are discussed in section 3.3. Lastly, the uncertainties within the model tests and post-processing and its sensitivity are discussed in section 3.4.

3.1. Experimental setup

In this section, first the general setup in the tank is elaborated on, after which in more detail the model setup is discussed. Lastly, details of the used sensors and measurement equipment are given.

3.1.1. Tank setup

The tests were performed in the small towing tank at the faculty 3mE at Delft University of Technology. A schematic top view of the tank including setup is given in Figure 3.1. The selected location of the model in the tank is based on a trade-off between maximising test time in undisturbed water and site accessibility. Data must be recorded in undisturbed water, thus the time before the reflected waves are interfering the measurements should be as long as possible. For a proper measurement at least five undisturbed oscillation cycles or incident waves must be measured. The limiting frequencies at a location were calculated using the dispersion relation.

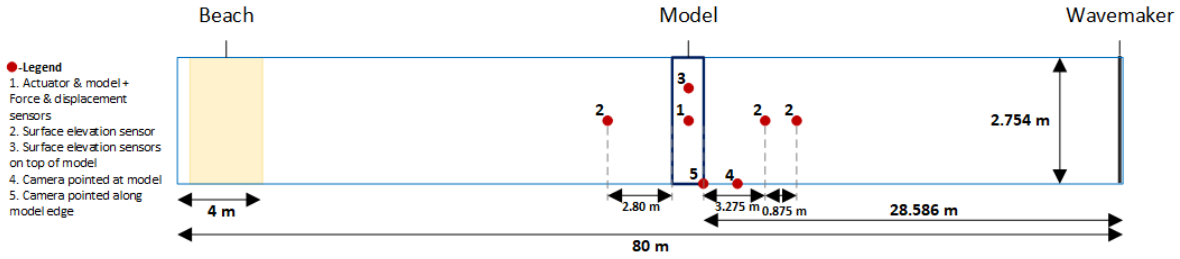

Figure 3.1: Schematic top-view of the setup of the tank

The width of the setup is equal to the tank width to eliminate reflections at the tank walls. In this manner a two-dimensional situation is recreated, such as desired. The elevations of the free surface are monitored by wave probes. Seven of them were spread on top of the model. Two wave probes were placed in front of the model to measure the incoming and reflected waves. Behind the model there is a wave probe to measure the radiated wave to the other side for oscillation tests and the transmitted wave over the model at wave load

tests. The locations are based on findings of Goda and Suzuki [9], who concluded that wave probes should at least be a two-tenths wavelength away from the model to retrieve clear data on incoming and reflected regular waves. The distance between wave probes should not be a multiplication of half a wavelength. The shown locations on the figure have been chosen taking into consideration the information listed above, in combination with the chosen frequency range, which is elaborated on in subsection 3.2.1.

The properties of the tank and wavemaker are given in Table 3.1. The water depth was kept 1.2 m and the measured water temperature was 21.5 $^{\circ}C$ for which the corresponding density is found.

Table 3.1: Properties of the towing tank (TU Delft [30])

Tank feature	Value
Water depth	1.2 m
Water temperature	21.5 $^{\circ}C$
Water density (Weast [35])	997.882 $\frac{kg}{m^3}$
Wavemaker type	Piston-type
Maximum possible wavelength	6.5 m
Shortest possible wavelength	0.4 m

3.1.2. Model setup

The model setup includes some challenges that are discussed first. Afterwards is elaborated on the chosen submergences. Lastly, the configuration for each test type is explained.

Scaling and accompanied challenges

Scaling is done according to Froude laws, which represents gravitational forces over inertia forces. Preferably, the model scale is as large as possible to make the scale effects as small as possible. However, the scaling factor is also limited by the test facilities and available equipment. Considering this, a scaling factor of 0.025 was chosen. This is a proper balance between accuracy of a small displacement and problems regarding scale effects. Besides, a model at scale 1:40 implies already a challenge by having a displaced volume of 0.771 m^3. Preferably, the model is neutrally buoyant during the tests for the following safety related and practical reasons.

- There is no risk that the model launches itself once a connection is (intentionally) loosened. Loosening a connection, i.e. at the force sensor, would otherwise cause the buoyancy force to not be counteracted anymore resulting in an unsafe situation.
- It is easier to actuate the model as the motor does not have to overcome additional buoyant forces.
- The force sensor has no preload, thus no larger force range is needed on the sensor to accommodate for this.

The buoyant force is compensated by filling the model with water, this leaves a little buoyant force due to the difference in density of water and plywood. This remaining buoyant force is counteracted with some blocks of lead. No sloshing occurred in the model as there was no air present inside the model at all times during testing.

Chosen submergences

The most important objective of model test, is to gain as many valuable insights as possible in a limited amount of time. Therefore, it has been chosen to study three submergences. The largest chosen submergence is 5 meter in full scale, which is 125 mm on model scale. As already mentioned in section 2.4, it is believed one is still able to predict the correct hydrodynamic data for the cross-section of the floater at this submergence with linear diffraction theory for operational sea states. Then a full scale submergence of 1.5 m, 37.5 mm on model scale, is chosen as approximately this submergence is used mostly in practice by SSCV-operations at inconvenient draft. The shallowest submergence chosen is 0.5 m on full scale, translating to 12.5 mm on model scale. At this submergence the most distinct results were seen in the numerical analysis.

Configuration for heave motions and wave load tests

Two different configurations were needed be able to measure data for both heave and pitch hydrodynamic coefficients and wave loads. One setup was designed for the heave motion and wave load tests. At the configuration for pitch the model must be able to make a rotational motion. During the model tests, the same

conventions are used as during the numerical analysis. This results that the positive x-axis is points in longitudinal tank direction towards the wave maker, see Figure 3.1. The z-axis is positive vertically upward and the y-axis is perpendicular to the width of the tank. The most important specifications of the model are given in Table 3.2.

Table 3.2: General properties of the model

Model feature	Model scale value	Full scale value
Scale factor	0.025	1
Width	2706 mm	108.24 m
Length	843.75 mm	33.75 m
Height	337.5 mm	13.5 m
Bilge radius	25.4 mm	1.016 m
Displaced volume	0.771 m^3	49344 m^3
Submergences	12.5, 37.5 and 125 mm	0.5, 1.5 and 5 m
Oscillation and wave frequencies	1.60 - 7.59 $\frac{rad}{s}$	0.253 - 1.2 $\frac{rad}{s}$

The model and setup for heave and wave load tests including annotations for equipment, is shown in Figure 3.2. More drawings and details of the model can be found in Appendix B. In the configuration for heave oscillation and wave load tests the actuator is placed exactly above the horizontal middle of the floater. The actuator is a FESTO linear positioning drive with an accuracy in displacement of 0.1 mm, external weight restriction of 30 kg and external force restriction of 600 N. The suspension system is connected to the model using three vertical plates. The middle vertical plate is used transfer the excitation force directly to the model and thereby avoid elasticity due to deflection in the profiles that cover the distance between both ends of the model.

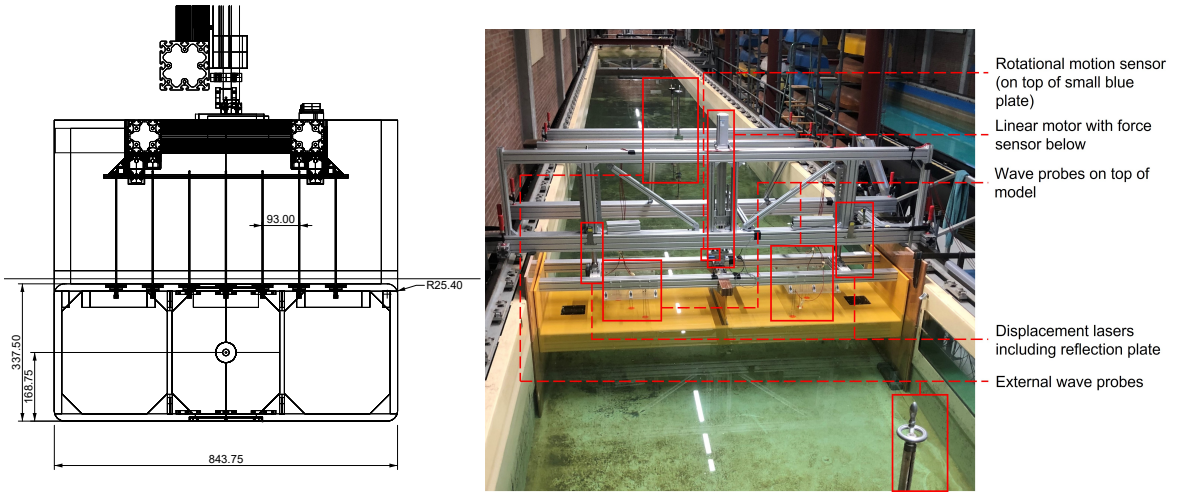

Figure 3.2: Model configuration for heave and waveload tests including annotations on the different equipment

Item-profiles are attached to the vertical end plates to create the largest possible undisturbed area on top of the model. Divided over both areas, wave probes are placed parallel to the tank width such that the location in x-direction is defined. The probes have a small diameter and their presence will diffract water in an accepted small amount. Inside the model three longitudinal and two transverse bulkheads are placed for extra stiffness. The vertical motion is guided by two large linear guides, with neglectable resistance, which also help to withstand horizontal wave loads. At the bottom of the model two hatches are placed to facilitate water inflow and outflow of water into the model. The hatches on top of the model are required for the pitch tests. Both the side plates and vertical middle plate will have flattened vertical edges to reduce the amount of undesired diffraction. The gap between the model and the large brown plates, required during pitch tests, was 6 mm at each side. The center of rotation for pitch tests is placed 168.75 mm above the keel.

Adjustments to setup for wave load tests

During the wave load tests two extra 80 N force sensors have been added to keep the model fully restrained. Otherwise, the model made small undesired pendulum motions around the frame on top of the tank, when exposed lower frequent waves. At lower frequent waves, and thus longer waves, the orbital velocity at depth is larger than for shorter waves considering a constant amplitude [10]. These higher velocities cause larger horizontal loads, resulting in small pendulum motions. To counteract this phenomena, one extra for the horizontal force sensor and one sensor for vertical loads have been added. These are located as close as possible to the middle of the model at the side of the wave maker, and are shown in Figure 3.3.

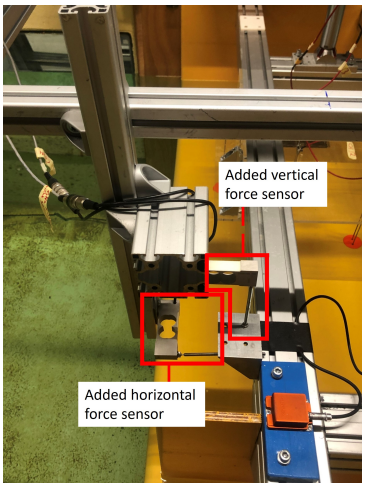

Figure 3.3: Added vertical and horizontal force sensors to prevent pendulum motions during wave load tests

Configuration for pitch motions

To create a pitch motion equal to the numerical analysis a center of rotation is created at the center of the cross-section of the floater. It is known that this does not represent a rotational motion of a SSCV, since in reality the center of rotation is located in between the two floaters. For an SSCV this motion is a roll motion, but due to the used coordinate system in this study it is named a pitch motion. In reality, a roll motion for an SSCV will result more in a kind of counteracting heave motions of both floaters. During the model tests a pure rotational motion was applied.

Details of the model in pitch configuration is shown in Figure 3.4. In each of the large wooden plates at the tank side, a stainless steel plate is integrated in which a bolt can be mounted from the model in the three chosen different submergence depths of 0.5, 1.5 and 5 m in full scale. The hatches on top of the model, which can be better seen in Figure 3.2, allow to make the bolted connection reachable from inside the model. In Figure 3.4a. the adjusted location for the linear motor can be seen. It is attached to the model using a double jointed construction. This construction is needed as the point of application of the model also has a small horizontal displacement as a result of the imposed vertical motion by the motor. The linear motor does not allow for out of plane movements and can therefore only move up and down. The double joint mechanism, of which a close up can be seen in Figure 3.4b, makes it possible to actuate pitch motions with the linear motor. The downside of such a mechanism is that the rotational motion is not a perfect sinusoid anymore. The smaller the angle, the better a perfect sinusoidal rotational motion is approached. This has been taken into account in the test matrix and is discussed in subsection 3.2.1. The horizontal distance between the center of rotation and the point of application of the linear motor, thus the arm of the applied moment, is 0.47 m.

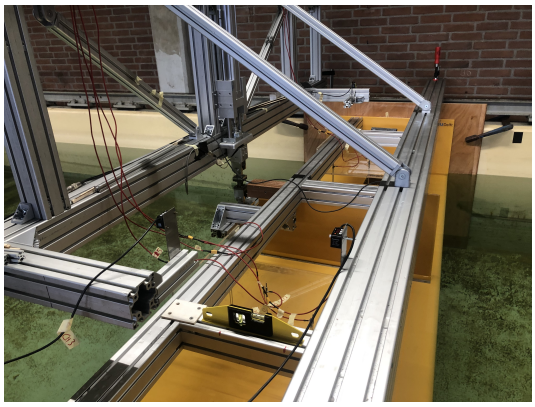

(a) Closeby look on top of the model

(b) Close up of the double hinge system

Figure 3.4: Configuraton for pitch tests

3.1.3. Details on used sensors

A light has already been shed on the different sensors that have been used. Emphasis is placed to properly record what physically occurs on top and around a large object at inconvenient draft, when oscillating the object and expose it to waves. Essential to measure are the radiation force and displacement during forced

oscillation tests, and wave forces and incoming wave characteristics for the captive tests. This data can be converted to hydrodynamic coefficients, wave loads and ultimately a motion RAO, which is an objective of this study. As said, the actuator of the model is a linear positioning drive by FESTO. Between the motor and the model a cube containing the force transducer is placed to measure the forces. The input of the linear motor may be used to measure the displacement, however it is chosen to use the mean out of three laser signals as displacement signal in heave direction. The reason is that the linear motor and the force sensor cause an inaccuracy in displacement that cannot be detected by input to the linear motor. The force sensor causes inaccuracy due to elastic deformation on which a transducer is based.

For the pitch motion, the measured force will have to be converted into a moment for the momentum balance around the pivot point in order to obtain correct hydrodynamic coefficients. The rotational motion was measured using an angular motion sensor. This signal can be checked using the laser signals, however these are not chosen for the angular displacement as they are less accurate for angular motions. Details on the used sensors can be found in Table 3.3.

Table 3.3: Details of the implemented sensors to measure the requested data

Device	Type	Amount	Range model scale	Range full scale	Accuracy model scale
Force sensor	Force transducer home-made at TU Delft	1	± 800 N	± 51.2 MN	few Newton 0.1 mm displ.
Additional force sensor	Not specified	2	± 80 N	± 5.12 MN	few Newton
Wave height meter	Wave probe home-made at TU Delft	3	≈ ± 200 mm	≈ ± 8 m	0.1 mm
Embedded wave height meter on top of model	Wave probe home-made at TU Delft	7	≈ ± 100 mm	≈ ± 4 m	0.1 mm
Displacement laser	Panasonic HG-C1400	3	± 200 mm	± 8 m	0.3 mm
Angular motion sensor	XSens MTi-20-2A5G4	1	velocity: ± 450° s^{-1} acceleration: ±20g	velocity: ± 71.2° s^{-1} ±20g	0.2°

To get a better understanding of the behaviour of radiated and diffraction waves, wave probes are placed to monitor the free surface on top, in front of and behind the model as discussed in the previous sections. Visual recordings have been made to gain more insight into the behaviour of the water. This data may also be interesting for further research. The point of view of the two cameras can be seen in Figure 3.5.

(a) Camera 1: Recording of the complete model

(b) Camera 2: Recording of the transition from deep to undeep water region

Figure 3.5: Point of view of the cameras which make a visual recording of the tests

3.2. Test method

The two types of desired data require different test methods. In order to obtain hydrodynamic coefficients, forced oscillation tests were performed, which is explained in subsection 3.2.1. Captive tests were performed to obtain wave load data, on which is elaborated in subsection 3.2.2.

3.2.1. Forced oscillation tests

During a forced oscillation test the model is, as the name implies, forced to oscillate at a specific frequency with a specific amplitude in a desired direction in still water. This results in radiation forces which can be

redirected to added mass and damping. The goal of doing these tests is to obtain data on the displacement, force and surface elevation over time for specified frequencies. By changing the amplitude the non-linear effects and possibly the effect of surface breaking can be seen. The linear domain is approached better using a smaller amplitude.

Tests for both heave and pitch were performed frequency range of $\omega_{fullscale}$ = [0.253, 1.20] $\frac{rad}{s}$, resulting in a $\omega_{modelscale}$ = [1.60 , 7,59] $\frac{rad}{s}$. The conversion is done using the non-dimensional frequency relation given in Equation 3.1. The limits are determined using the dispersion relation. The lower limit is based on the minimum number of oscillations to be performed in undisturbed water, in combination with the location of the model in the tank. The upper limit is determined as by then the maximum allowable force of the actuator has almost been reached and the numerical data, which is elaborated on in chapter 4, shows convergence.

$$\bar{\omega} = \frac{\omega^2 L}{g} \tag{3.1}$$

The test matrices for the forced oscillation tests are shown in Tables 3.4 and 3.5. The matrix is four dimensional, taking into account the degree of freedom, submergence, oscillation amplitude and frequency. This allows to gain insights in the hydrodynamic coefficients for a specific submergence over the frequency domain and the level of nonlinearity involved by increasing the oscillation amplitude. Only the unique frequency points have been displayed, as some tests are repeated to be able to discuss the sensitivity of the setup in section 3.4.

The test matrices are arranged such that the interesting numerical data points over the complete frequency domain are tested. Symbols x_a and θ_a represent the oscillation amplitudes in heave and pitch. Focus is placed such that extremes and rapid numerical data fluctuations over frequency domain are covered to retrieve a clear view of the physical reality. The numerical outcome can be seen in chapter 4. An extra benefit for performing the pitch tests is that global numerical extremes at the smallest submergences are covered properly. The global extremes for heave are located at a too low frequency to properly analyse them. The amplitudes were chosen with the idea of making the best possible linear approximation and gradually increased at interesting frequencies. Consequently, they were mainly kept small during the tests and larger amplitudes were also applied at frequencies with an interesting numerical value, such as an extreme.

Table 3.4: Test matrix for forced oscillation heave tests, in total 40 unique heave tests have been performed

Submergence	x_a (mm) model sc.	x_a (m) full sc.	Full scale frequencies (rad/s)									
0.5 m full sc. 12.5 mm model sc.	2.5	0.1	0.253	0.40	0.48	0.51	0.54	0.60	0.75	0.91	1.00	1.20
	6.25	0.25	0.40	0.75								
	18.75	0.75	0.40	0.75								
1.5 m full sc. 37.5 mm model sc.	2.5	0.1	0.26	0.29	0.33	0.40	0.52	0.63	0.81	1.00	1.20	
	6.25	0.25	0.40	0.63								
	18.75	0.75	0.40	0.63								
5 m full sc. 125 mm model sc.	2.5	0.1	0.253	0.32	0.40	0.44	0.60	0.75	1.00	1.20		
	6.25	0.25	0.40	0.60	0.75							
	18.75	0.75	0.40	0.60								

Table 3.5: Test matrix for forced oscillation pitch tests, in total 32 unique pitch tests have been performed

Submergence	θ_a (deg)	Full scale frequencies (rad/s)								
0.5 m full sc. 12.5 mm model sc.	0.5	0.253	0.30	0.37	0.38	0.39	0.50	0.67	1.00	1.20
	1	0.37	0.67							
	2	0.37	0.67							
1.5 m full sc. 37.5 mm model sc.	0.5	0.253	0.37	0.49	0.55	0.61	0.87	1.00		
	1	0.55	0.87							
	2	0.55	0.87							
5 m full sc. 125 mm model sc.	0.5	0.253	0.49	0.88	1.00					
	1	0.49	0.77							
	2	0.40	0.49							

3.2.2. Captive tests

During the captive tests, the model is restrained while waves are exposed to it. The goal of these tests is to capture wave loads on a submerged body over frequency range at specific submergences. The desired data for these tests are the vertical force on the body and the free surface elevation in front, behind and on top of the model.

Captive tests are limited in frequency range by the wave maker. As presented in Table 3.1, the maximum possible wavelength is 6.5 m, resulting in a minimum model scale frequency of 2.79 $\frac{rad}{s}$, equal to 0.441 $\frac{rad}{s}$ on full scale. The minimum wavelength that can be produced is 0.5 m which corresponds a frequency that does not affect the upper limit of 1.20 $\frac{rad}{s}$.

The test matrix for the captive tests is shown in Table 3.6, in which ζ_a represents the incident wave amplitude. The rationale behind the matrix is the same as for the forced oscillation tests. In addition, emphasis has been placed that, if possible, the frequency matches a frequency of the forced oscillation test so that an RAO can be determined for that frequency.

Table 3.6: Test matrix for wave load tests, in total 44 unique wave load tests have been performed.

Submergence	ζ_a (mm) model sc.	ζ_a (m) full sc.	Full scale frequencies (rad/s)							
0.5 m full sc. 12.5 mm model sc.	3.25	0.13	0.441	0.51	0.54	0.67	0.75	0.91	1.00	1.20
	8.00	0.32	0.441	0.51	0.67	0.75	0.91	1.00		
	23.0	0.92	0.51	0.67						
1.5 m full sc. 37.5 mm model sc.	3.25	0.13	0.441	0.52	0.55	0.63	0.81	0.87	1.00	
	8.00	0.32	0.441	0.55	0.63	0.87	1.00			
	23.0	0.92	0.63	0.87						
5 m full sc. 125 mm model sc.	8.00	0.32	0.441	0.49	0.60	0.77	1.00	1.20		
	16.0	0.64	0.441	0.60						
	32.5	1.3	0.441	0.60						

3.3. Post-processing

The gathered data cannot be implemented immediately. In order to make it understandable, it must first be processed. This includes a part of general data processing that applies to each test. In addition, there are specific processing steps for the forced oscillation and wave load tests.

3.3.1. General data processing

The measured data is in time domain, while the desired representation is in frequency domain. This means that a harmonic fit has to be made of each test to get a magnitude of each signal at a specific frequency. Before one can make a proper fit, the data has to be filtered. Measurements are performed with a sampling frequency of 1000 Hz and include noise which can be divided in low- and high-frequent noise.

Low frequent noise can be present as a result of long waves which were still present in the tank when conducting the tests. These waves do not affect the final results as they are really long and have a low amplitude, however they do affect the surface elevation signals with a relatively low frequent wave which should get filtered out in order to make a proper harmonic fit. Another occurrence of low frequent noise is seen in the angular motion measurements in which the noise is caused by the internal reference system of the XSens-sensor.

The high frequent noise in the signal are caused by attachment of the model to the linear motor and the accuracy of the sensor. The force sensor measures forces through voltage differences across the sensor as a result of elastic deformation of the sensor. As a result, the force sensor can be seen as a spring and the system acquires a kind of eigenfrequency which is in the domain between 3 and 5 Hz depending on the type of test and set-up. This can be seen when comparing the force signal of a test and zero measurement using a Fourier transform, as shown in Figure 3.6.

In the first subplot both the transform of the full force signal as a signal of the same time length as the performed zero measurement are shown. The transform over a time domain equal to zero measurement is required for a proper comparison. In the complete measured force signal, the ramp up and ramp down period are included as well, causing a lot of variance. The energy in the system during the zero measurement

is low, which results in a small variance. Therefore, in the second subplot a close up of this specific variance density spectrum is shown. The peak frequency is higher for the zero measurement than for the measured force signal, which is a result the motion of the model during the tests. At the bottom subplot a graph can be seen of the force signal during the tests and zero measurement over time domain, which have been used in the analysis. When comparing Figures 3.6a and 3.6b, it can be seen that the frequency region for pitch is at a higher frequency than at the heave test. A proof that the eigen frequency of the system is causing this hump. As in heave tests the mass which is actuated is larger than the weight at the pitch test. A higher mass causes the natural frequency to be lower. The cause of the actuation of the model at the zero measurements is the remaining buoyancy in heave and stability in pitch.

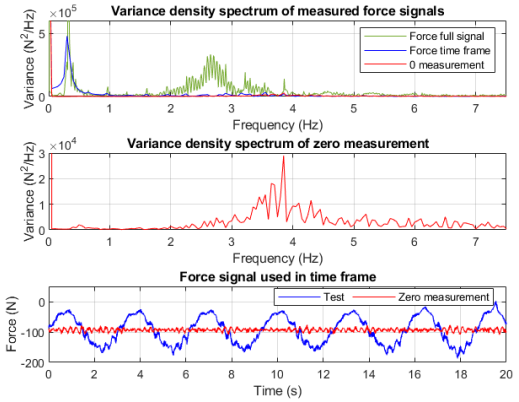

(a) $s_{modelscale}$ = 125 mm, $\omega_{modelscale}$ = 2.02 $\frac{rad}{s}$ = 0.32 Hz and $x_{a,measured}$ = 2.62 mm

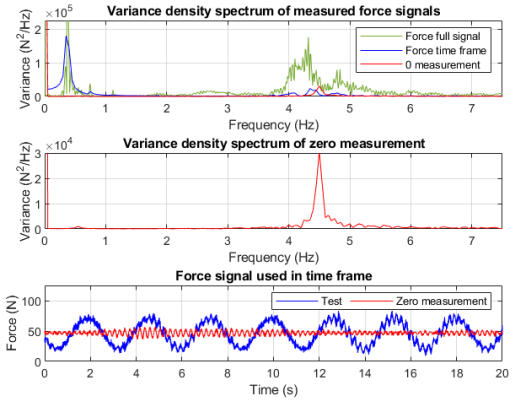

(b) $s_{modelscale}$ = 37.50 mm, $\omega_{modelscale}$ = 2.34 $\frac{rad}{s}$ = 0.37 Hz and $\theta_{a,measured}$ = 0.57°

Figure 3.6: Comparison of a Fourier Transform of a zero measurement and its accompanied measurement for both a heave and pitch forced oscillation test

A band pass filter is used to filter the signal before a harmonic will be fitted. Frequency limits of 0.2 Hz and 3 Hz are set, which are equivalent to 1.26 $\frac{rad}{s}$ and 18.85 $\frac{rad}{s}$. These limits ensure that unwanted noise is filtered out and are also still distant from the frequency domain in which we are interested in this study. Sometimes, the upper limit of filter was too high to filter all the noise, for those tests the cut-off frequency at the upper limit was reduced. In addition to the force signal, the free surface elevation required filtering too due to a bandwidth over the signal. The displacement lasers do not require filtering.

In Figure 3.7, a force signal is displayed from a heave forced oscillation test, in which the model is oscillated at a model scale frequency of 2.51 $\frac{rad}{s}$ and a model scale amplitude of 2.5 mm. The force signal shows large forces at the beginning and at the end. These are caused by the manual ramp up and ramp down of the model motion signal. An effect of these forces is not seen in the surface elevation signals, thus it is assumed that these do not affect the results. It can be seen that the signal is noticeably affected by the reflected waves from 40 seconds and onwards. It remains harmonic, however the amplitude is reduced. To make the transformation from time to frequency domain, a sine fit is made over the data using the built-in function in MATLAB. This fit is made over a specific time span within the measurement where complete oscillation or wave load occur in undisturbed water and the force signal is not affected by the ramp up. Figure 3.8 shows a harmonic fit belonging to the force signal in Figure 3.7. The sine fit, based on a nonlinear least squares method, computes a resultant fitted amplitude, frequency and the fitted phase angle with respect to t = 0. The sine fit function is found to be sensitive for the phase angle, a frequency difference of a couple of thousandths could vary the phase angle by tenths of radians.

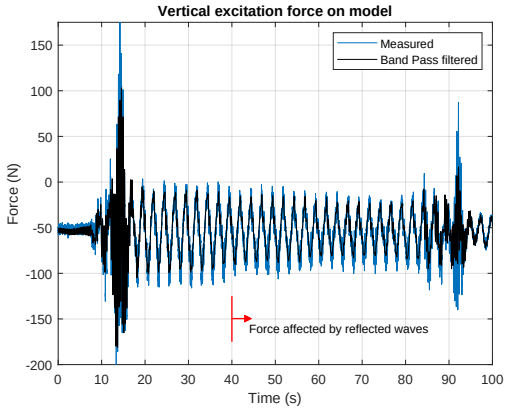

Figure 3.7: Filtering of data using a band pass filter having a lower limit of 0.2 Hz and upper limit of 3 Hz

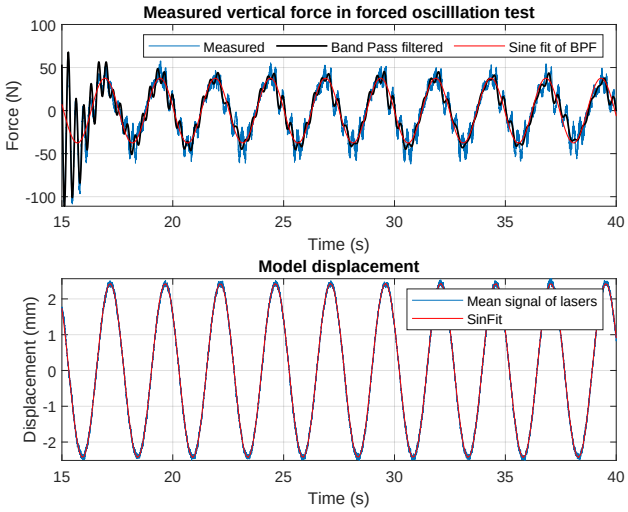

Figure 3.8: Harmonic fit over the filtered data signal for a test with $s_{modelscale}$ = 12.5 mm, $\omega_{modelscale}$ = 2.53 $\frac{rad}{s}$ and $x_{a,modelscale}$ = 2.5 mm. The presented data is the time domain $[t_{fit,start} - 5\,;\, t_{fit,end} + 5\,]$ s

The obtained amplitude and frequency can be used directly, while the phase angle requires some adjustment. The description of a harmonic in the linear domain is given by a cosine, as shown in Equation 3.2. To arrive at a correct phase angle with respect to time, the relationship between a sine and cosine given in Equation 3.3 is used. This means that the phase angle resulting from the sine fit must be subtracted from $\frac{\pi}{2}$ to achieve a correct phase angle with respect to time, $\varepsilon_{x,t}$. Furthermore, the convention of the measured force signal is positive downward, while the displacement and surface elevation sensors have a positive convention upwards. Hence, an extra factor of π rad is added to the force phase angle to have its convention upwards too, which is also equal to the global coordinate system used in this study.

$$x = x_a \cos(\omega t + \epsilon_{x,t}) \tag{3.2}$$

$$\sin(\varepsilon) = \cos(\frac{\pi}{2} - \varepsilon) \tag{3.3}$$

As indicated above, the phase angles are given with respect to time. However, the phase angle of force and its related displacement are given relative to each other in representation in the frequency domain. This enables the signal properties to be independent of time. The relation between the two phase angles is given in Equation 3.4. Using this relation, one redefines the time vector such that the displacement signal is zero at t = 0. Subsequently, the force signal is adjusted by $\varepsilon_{F,x}$, which is related to the displacement signal, and therefore the phase angle is now independent of time in the measurement. Eliminating the time dependency of the phase angle by relating the signals to each other makes the earlier performed translation from sine fit to cosine fit irrelevant at first sight. However, it is still performed to know the correct phase angle for comparing the results over time to the numerical results in time domain later on.

$$\varepsilon_{F,x} = \varepsilon_{F,t} - \varepsilon_{x,t} \tag{3.4}$$

The implementation of the phase angle of force relative to the displacement alters the mathematical description of the harmonic displacement x, its time derivatives and force F. The used harmonic descriptions for these physical quantities are shown in Equations 3.5 to 3.8.

$$x = x_a \cos(\omega t) \tag{3.5}$$

$$\dot{x} = -\omega x_a \sin(\omega t) \tag{3.6}$$

$$\ddot{x} = -\omega^2 x_a \cos(\omega t) \tag{3.7}$$

$$F_z = F_a \cos\left(\omega t + \epsilon_{F,x}\right) = F_a \cos\left(\varepsilon_{F,x}\right)\cos(\omega t) - F_a \sin\left(\varepsilon_{F,x}\right)\sin(\omega t) \tag{3.8}$$

The procedure presented is used to process the raw data into frequency domain properties for both forced oscillation and wave load tests. Thereafter, specific post-processing for forced oscillation tests and wave load tests was applied.

3.3.2. Forced oscillation tests

A force balance is set up to obtain the correct formula to convert the retrieved frequency domain data into hydrodynamic coefficients. The force balance, based on Newton's second law, is set using the free body diagram in Figure 3.9, resulting in Equation 3.9.

The force F_z represents the measured force. The radiation force is broken down in three parts as represented in Equations 3.10 to 3.12. F_a is the in-phase hydrodynamic radiation force, F_b the out-phase hydrodynamic radiation force and F_s the hydrostatic radiation force. The substitution of the latter equations results in the equation of motion given in Equation 3.13.

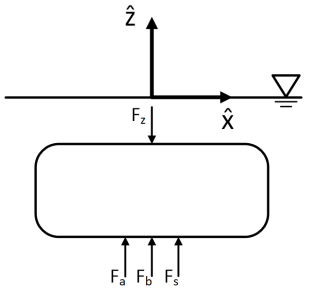

Figure 3.9: Free Body diagram of the neutral buoyant forced oscillated body

$$\sum F = -F_z + F_a + F_d + F_s = m\ddot{x} \tag{3.9}$$

$$F_a = -a\ddot{x} \tag{3.10}$$

$$F_d = -b\dot{x} \tag{3.11}$$

$$F_s = -cx \tag{3.12}$$

$$(m+a)\ddot{x} + b\dot{x} + cx = -F_z \tag{3.13}$$

The general mathematical description of the harmonic displacement and force as given in Equations 3.5 to 3.8 can be substituted in the equation of motion resulting in Equation 3.14. Subsequently, added mass and damping equations are derived by examining the time steps where the time-dependent sine is 0 and cosine is 1 and vice versa, as shown in Equations 3.15 to 3.18. The realized mass m of the model is 767.45 kg and the restoring coefficient c is 378 $\frac{N}{m}$. The restoring coefficient is a result of the waterline area of 0.0386 m^2 that is present due to the vertical plates connecting the box to the suspension system.

$$-(m+a)\omega^2 x_a \cos(\omega t) - b\omega x_a \sin(\omega t) + cx_a \cos(\omega t) = -F_a \cos\left(\varepsilon_{F,x}\right)\cos(\omega t) + F_a \sin\left(\varepsilon_{F,x}\right)\sin(\omega t) \tag{3.14}$$

if $\omega t = 0$

$$-(m+a)\omega^2 x_a + cx_a = -F_a \cos\left(\varepsilon_{F,x}\right) \tag{3.15}$$

$$a = \frac{\frac{F_a}{x_a}\cos\left(\varepsilon_{F,x}\right) + c}{\omega^2} - m \tag{3.16}$$

if $\omega t = \frac{\pi}{2}$

$$-b\omega x_a = F_a \sin\left(\varepsilon_{F,x}\right) \tag{3.17}$$

$$b = -\frac{F_a \sin\left(\varepsilon_{F,x}\right)}{\omega x_a} \tag{3.18}$$

Data of the pitch forced oscillation tests can be processed in the same manner, starting with Newton's second law for rotation. The equations for added mass and damping are similar to those for heave, however force F_a is replaced by moment amplitude M_a, displacement x_a by angular amplitude θ_a, $\varepsilon_{F,x}$ by $\varepsilon_{M,\theta}$ and mass m by mass moment of inertia I_{yy}. The measured force F_z is multiplied by the horizontal distance L to obtain a measured moment around the y-axis M_{yy}. Horizontal distance L is the distance between the center of rotation and the point of application of the force which is equal to 0.47 m. The mass moment of inertia in the center of rotation has been determined for the model, excluding water inside, using a pendulum test, see Appendix C, and resulted in a value of 27.08 kgm^2. With the use of Rhinoceros, the mass moment of inertia of the added water is calculated and added up to the experimental mass moment of inertia resulting in a total I_{yy} = 65.33 kgm^2. The vertical center of gravity of the model including water is 0.205 m measured from the bottom of the model. This led to a hydrostatic restoring coefficient c in pitch equal to -259.35 $\frac{Nm}{m}$.

3.3.3. Captive tests

Wave load data is represented as a ratio of force per meter wave amplitude combined with an associated phase angle compared to the incoming wave. The incoming wave is fitted to the surface elevation signal of the wave probe located the closest to the wave maker. This wave probe is at a distance of 4.15 m in front of the model, as can be seen in Figure 3.1. To adjust for the location a factor $k\Delta x$ is added to the fitted phase angle, as shown in Equation 3.19. In this formula Δx = -4.15 m since the positive x-direction is pointed in the direction of the wave maker and the wave probe is closer to the wave maker than the model is. The fitted surface elevation signal is used for the wave frequency and phase angle relative to time. No adjustments for the difference in timescale is needed as the sine fit in MATLAB calculates the phase angle relative to t = 0.

The phase angle adjusted for location can then be subtracted from the force phase angle as already explained with Equation 3.4.

$$\epsilon_{\zeta,t} = \epsilon_{\zeta,t_{fit}} + k\Delta x \tag{3.19}$$

The wave load per meter wave amplitude is determined by dividing the measured force amplitude by the measured wave amplitude. A small adjustment is made to the measured force signal due to the placement of the additional vertical force sensor. As the positive convention of the extra sensor could only be installed contradictory to the positive convention of the main force sensor, the extra measured vertical load is subtracted from the measured force at the sensor at the linear motor to lead to a correct total vertical load on the model during wave load tests.

To check what the exact wave amplitude was at each tests, undisturbed wave tests have been performed. Due to time limitations not all waves could be ran, the results including the mean per amplitude group are graphically represented in Figure 3.10. A measurement of the disturbed surface elevation signal, thus measured signal during the tests, is not accurate and reliable enough for a proper wave amplitude. Therefore, the force amplitude is divided by the mean of the wave amplitude group in case the undisturbed wave amplitude has not been measured. In total 16 out of 35 unique undisturbed waves could be tested. In the figure, it can be seen that the amplitude of the undisturbed wave is not constant over frequency range. The linear approximation of the wave height to stroke transfer function for piston-type wave makers by Ursell et al. [31] has been used for the input to the wave maker. This is a proper transfer function, but it is still a theoretical approach and therefore the wave heights may differ in practice, something which is also shown in the paper itself.

An example of the resultant wave load and surface elevation of a regular wave captive test is shown in Figure 3.11. It also shows that the disturbed wave amplitude is over 25% larger than the undisturbed wave.

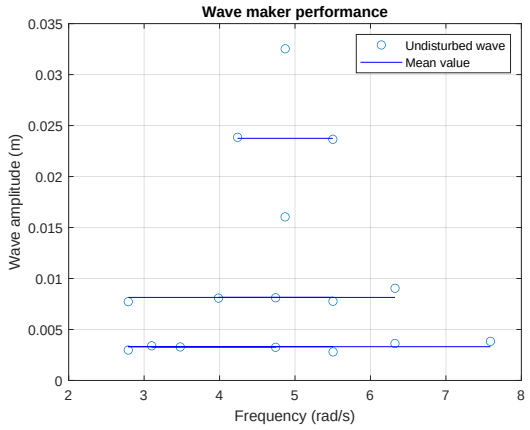

Figure 3.10: Wave maker performance measured with undisturbed waves

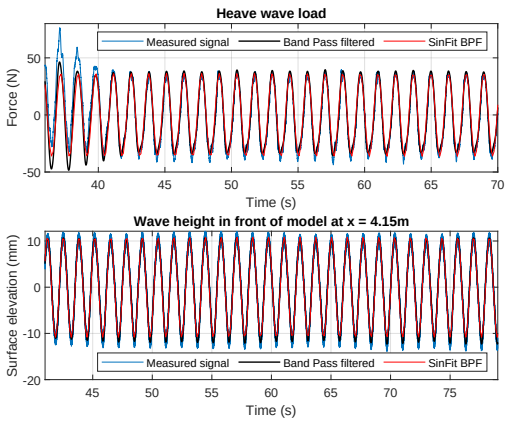

Figure 3.11: Measured force and surface elevation for wave load test at frequency of 4.74 $\frac{rad}{s}$ and an undisturbed wave amplitude of 7.91 mm, representation of the domain $[t_{fit,start} - 5\,;\, t_{fit,end} + 5\,]$ s

3.3.4. RAO

The main objective of this study concerns the motion prediction for a body at inconvenient draft. Experimental RAO data points in heave are created at frequencies at which both hydrodynamic coefficients and wave loads are measured. The data is then converted to a complex RAO, using Equation 3.20. The same formula, but with adjusted data is used for the pitch RAO. Its absolute value is the amplitude of the RAO and is used in the comparison with numerical data.

$$\frac{x_a}{\zeta_a} = \frac{F_{a,waveload} \cdot e^{i\epsilon_{F,\zeta}}}{c - (m+a)\omega^2 + ib\omega} \tag{3.20}$$

3.4. Uncertainties and sensitivity

Model test always do include uncertainties. Hence, emphasis is placed on making the uncertainties as small as possible. This was considered in the design of the model already. The vertical plates, required to connect the model to the suspension system, have been placed such that the largest possible undisturbed area was created on top of the model. The vertical plate in the middle, placed directly under the point of application of the motor, connects the suspension system with the model to reduce possible elasticity in the suspension system. All vertical plates have been flattened to reduce diffraction, and for the wave probes is tried to reduce diffraction issues as far as possible.

Part of the uncertainty lies in the sensitivity of the setup. The actuation of the model is sensitive because of the relatively small displacement amplitudes, in combination with the accuracy of the actuator and stiffness of the force sensor. To quantify this, several test have been replicated and the results are shown in Table 3.7. It turned out that during tests at the same frequency the oscillation amplitude deviated by up to 0.5%, except for one small outlier in pitch test. This shows a proper repeatability for the oscillation amplitude. It should be noted that for lower amplitude tests the smallest aimed model scale oscillation amplitude in heave was 2.5 mm. During most of the tests the measured amplitude remained within the inaccuracy limits of the actuator, which is including the stiffness of the force sensor 0.2 mm. However, at higher frequencies measured amplitudes of 2.94 mm have been seen, deviating up 17.6% from the intended amplitude. Frequency dependent deviations had a gradual progression towards higher frequencies, but more important is that the displacement amplitude is rather constant when repeating a tests.

Table 3.7: Model scale test data of the replicated tests including the sensitivity of the most important measured signals

Type	Subm. (mm)	ω ($\frac{rad}{s}$)	x_a, ζ_a (mm) or θ_a (deg)	Δa_{mean} [1]	F_a (N) or M_a (Nm)	ΔF_{mean} [1]	$\epsilon_{F,x}$ (deg)	$\Delta\epsilon_{mean}$ [2] (deg)
Heave forced oscillation	12.5	3.225	2.502	0.03%	25.04	0.45%	-81.3	1.15
		3.226	2.504		24.81		-83.6	
		4.743	6.438	0.02%	134.31	0.25%	-27.1	0.75
		4.744	6.436		133.64		-28.6	
	37.5	2.529	18.424	-0.33%	436.83	-3.40%	-110.1	0.67
		2.529	18.511	0.15%	462.16	2.21%	-108.2	-1.23
		2.530	18.518	0.18%	457.58	1.19%	-110.0	0.57
	125	2.023	2.624	0.04%	59.81	4.63%	-11.8	2.35
		2.024	2.621		65.62		-16.5	
		3.795	2.560	0.19%	100.55	0.57%	-74.7	0.90
		3.796	2.570		101.70		-76.5	
		6.324	2.818	0.09%	173.65	0.86%	-4.0	0.35
		6.325	2.813		170.70		-3.3	
Captive tests	37.5	5.502	23.654 [3]	0.00%	159.19	0.91%	43.0	0.10
		5.503	23.654 [3]		156.33		42.8	
Pitch forced oscillation	12.5	2.341	0.557	1.05%	22.59	6.39%	-90.2	-5.08
		2.339	0.549	-0.44%	20.87	-1.70%	-95.6	0.33
		2.339	0.551	-0.11%	20.60	-2.97%	-96.8	1.53
		2.338	0.549	-0.50%	20.87	-1.72%	-98.5	3.33
	37.5	5.503	0.573	0.02%	10.83	0.48%	-23.3	0.20
		5.503	0.573		10.93		-23.7	

[1] Percentage compared to mean at frequency, if only two tests performed an absolute value of the percent deviation to the mean value is given

[2] Deviating angle from mean at frequency, given as absolute value since percent deviation results in a misleading view for angles

[3] Assumed that an identical wave was sent from wave maker

Yet, the measured force signal showed a more significant deviation. The accuracy of the 800-Newton force sensor causes deviation of a few Newtons on replication tests. The impact is minor on tests if large forces are measured. However, there are also tests where the average measured force is 63 N, such as at ω = 2.023 $\frac{rad}{s}$ on s = 125 mm. Here, the difference between the forces amplitudes is almost 6 N, which then suddenly does

have an impact of 9.26%. The results will therefore have to be examined taking this into consideration.

Furthermore, there is an uncertainty for the wave loads of the waves that do not have a measurement of the undisturbed wave. Although an average wave amplitude has been taken into account at these tests, this can cause small deviations. At lower frequencies, the wave load can be underestimated due to the small pendulum motions which could not fully be remedied at larger submergences.

Due to the relatively small water column on top of the floater, it was important to check the water level frequently, as the water at the test facilities vaporizes and lost approximately 0.5 mm each day. If a too low water level was noticed, it had to be corrected immediately. Especially at the smaller submergence tests, this can quickly lead to an incorrect modelled scenario.

Lastly, it is important when post-processing to make a proper harmonic fit. The frequency of both the force and displacement signal are fitted to thousandths as the fitted phase angle is very sensitive and may differ by tenths of radians for a slightly different frequency. At the replicated tests, the phase angles can deviate multiple degrees from the mean, as shown in the last column in Table 3.7. It is chosen to represent absolute values for the deviating phase angles as a percent deviation is misleading for angles. Emphasis has been placed to fit the data very precise as the phase angle has a significant impact on especially the hydrodynamic coefficients.

4

Results

In this chapter the results of the numerical analysis and model tests are discussed and compared to each other. The locations where discrepancies occur become clear. Both a physics-related and mathematical reasoning are given on the cause of the discrepancies. In this chapter, also the numerical and experimental data is compared to findings in literature and the validity of the underlying principles of the linear diffraction theory is discussed. This will eventually lead to an answer on the research question of this study.

In section 4.1 all results related to the heave motion RAO are discussed. Including a reasoning on the cause of the discrepancies and the validity of the theory. The pitch related data is discussed in section 4.2. The correctness of the use of free surface damping is discussed in section 4.3. Lastly, the nonlinear effects that arose at the tests with a larger amplitude are discussed in section 4.4.

4.1. Motion prediction in heave

All data related to the heave motion is discussed. First is started in subsection 4.1.1 with the comparisons of the numerical and experimental results, in which the RAO is discussed first and then the underlying hydrodynamic data. After that, the physics-related reasons are discussed in subsection 4.1.2 on why discrepancies do occur. In the last subsection, subsection 4.1.3, the suspected mathematical reasons are discussed. All results in are given on full scale unless otherwise mentioned. Also are all in this section results given for the smallest amplitude. The smallest oscillation amplitude is in full scale 0.1 m and a wave amplitude of 0.13 m during captive tests. The hydrodynamic data is given in 2D, which means that the data is per meter width of the body.

4.1.1. Numerical and experimental results

In this study, we are interested to understand the motion behaviour of an object submerged in close proximity to the free surface. Hence, we will first look at the numerical prediction of the motion RAO shown in Figure 4.1. Immediately noticeable are the predicted maxima at the smaller submergences, that seem unrealistic. At larger submergences the RAO values tend to become better physically interpretable. It is however surprising that the expected motions at smaller submergences seem not to be realistic even for small waves at which linear motions can be assumed. Before considering the experimental data, the expected motion behaviour is first explained, in order to ensure understanding of what is expected and thus to facilitate interpretation of the results.

The expected behaviour in the frequency domain is divided into three subdomains, where restoring, damping and inertial forces are dominant. The restoring forces are dominant at the lower frequencies, resulting in a motion where the object motions almost equal the wave motion, leading to a RAO ≈ 1 $\frac{m}{m}$. In addition, the low frequency limits for the heave RAO are reducing for larger submergences. This is to be expected since the fluid velocity decreases at increasing depth and thus the wave load decreases with increasing submergences, resulting in a lower RAO [10]. Then the damping terms become dominant around the natural frequency of the body. Damping decreases significantly around the natural frequency, leading to a peak in the RAO [15]. However, a fully submerged body does not have a natural frequency because it has no waterline area. Therefore, contrary to the numerical predictions, no peak in the RAO is expected at smaller submergences. At higher frequencies, the inertia becomes increasingly dominant with respect to the progressively

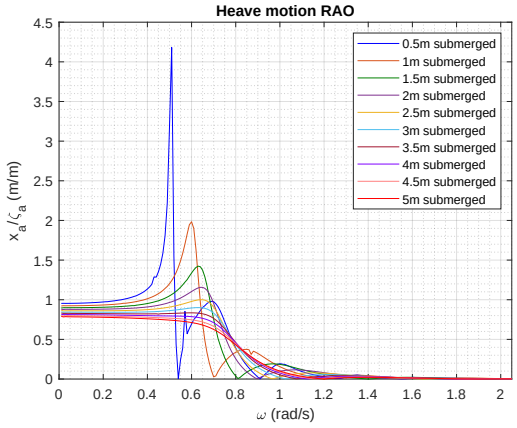

Figure 4.1: Heave motion RAO over submergence range resulting from diffraction theory

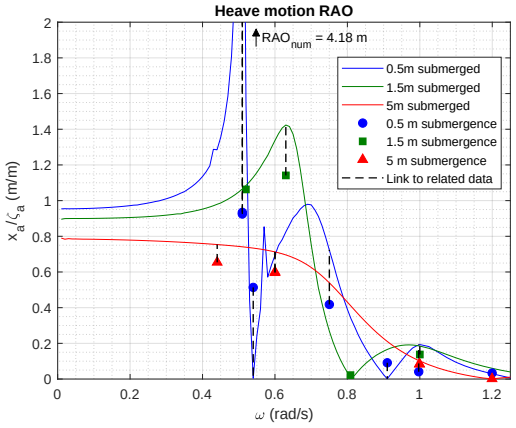

Figure 4.2: Heave motion RAO over submergence range comparison of numerical, solid lines, and experimental, markers, data

shorter waves, resulting in decreased values for the RAO. The same observations can be made considering the mathematical definition of an RAO in a linear system, shown in Equation 4.1.

$$\frac{x_a}{\zeta_a} = \frac{F_{a,waveload} \cdot e^{i\varepsilon_{F,\zeta}}}{c-(m+a)\omega^2 + ib\omega} \tag{4.1}$$

A comparison of the numerical prediction and experimental results is shown in Figure 4.2, in which also dashed lines are plotted to clarify the numerical data point to which the experimental data correspond. The most notable discrepancies are seen at the RAO for 0.5 m submergence. In Table 4.1, the corresponding experimental data at 0.5 m submersion is given including a percentage deviation from experimental to numerical data. A percent deviation is denoted in the table as %D plus an associated subscript. A negative percent deviation means that the numerical value is less than the experimental value, and a positive percent deviation means that the numerical prediction is larger than the experimental value. At the comparison for added mass, a difference is made between the actual percent deviation and the deviation of the inertial term, $(m+a)\cdot\omega^2$. Due to the occurrence of negative added mass, a discrepancy in added mass can have a significant opposite impact on the inertia term as can be seen at 0.51 $\frac{rad}{s}$. The damping coefficient is proportional to frequency, therefore the damping coefficient and damping term, $b\omega$, have the same percent deviation. Furthermore, the radiation force is determined to gain an insight on dependency of the damping and added mass term. The radiation force is determined using Equation 4.2. A negative deviation can maximum be -100%, meaning that the numerical prediction is zero. The mass m of the cross-section is 454.7 ton per meter width.

$$\frac{F_a}{x_a} = \sqrt{\left(c-(m+a)\omega^2\right)^2 + (-b\omega)^2} \tag{4.2}$$

Table 4.1: The experimental results at 0.5 m submergence for which RAO predictions are obtained including a percent deviation, %D, to the associated numerical data point. Data is, if applicable, given per meter width of the body

ω	RAO_{exp}	RAO_{num}	$\%D_{RAO}$	a_{exp}	$\%D_{addm}$	$\%D_{inertia}$	b_{exp}	$\%D_{damp}$	$F_{wl,exp}$	$\%D_{F_{wl}}$	$F_{rad,exp}$	$\%D_{F_{rad}}$
$[\frac{rad}{s}]$	[m]	[m]	[-]	[ton]	[-]	[-]	$[\frac{ton}{s}]$	[-]	$[\frac{kN}{m}]$	[-]	$[\frac{kN}{m}]$	[-]
0.51	0.92	4.18	352.0%	-347.4	23.6%	-76.5%	287.3	-85.2%	137.1	-28.1%	149.1	-84.8%
0.51	0.93	4.18	347.6%	-370.7	15.9%	-70.0%	286.0	-85.1%	137.1	-28.1%	147.5	-84.6%
0.54	0.51	0.004	-99.1%	-200.4	-128.4%	101.2%	361.8	-100.0%	106.3	-97.5%	209.0	-28.6%
0.75	0.42	0.72	73.2%	-37.24	354.6%	-31.6%	218.0	-18.3%	117.7	33.2%	286.3	-27.0%
0.91	0.09	0.001	-98.6%	256.2	18.2%	6.6%	102.1	-99.7%	53.8	-97.5%	596.2	5.3%
1.00	0.04	0.19	372.6%	353.3	-0.6%	-0.3%	86.9	241.9%	33.0	428.1%	807.7	5.7%
1.20	0.03	0.03	-11.1%	461.7	-10.6%	-5.3%	30.0	-37.6%	43.7	-6.3%	1319.4	-5.4%

In Figure 4.2, it can be seen that the first two deviations at 0.51 and 0.54 $\frac{rad}{s}$ are an overprediction followed by an underprediction. The results in Table 4.1 show that the discrepancy at 0.51 $\frac{rad}{s}$ is due to a significant

underprediction of the radiation force, which is predicted to be nearly 85% smaller than the experimental data point. Both the damping and inertia term are underpredicted. In Figure 4.5, which is discussed further in subsection 4.1.2, it can be seen that in the numerical prediction the added mass coefficient $a \approx -m$. This almost eliminates the inertial component in the denominator of the RAO. Together with an underpredicted damping term, the radiation force is significantly reduced, which is not compensated by the wave load that is 28.1% smaller. This results in an RAO that is predicted to be 350% too high compared to the experimental data point. The wave load in heave can be seen in Figure 4.8, and is discussed in more detail in subsection 4.1.2.

At 0.51 $\frac{rad}{s}$, the discrepancy is dominated by the wave load which differs by 97.5% in the numerical prediction. Although, the inertia term is 101% larger than the numerical predicted value, the damping term is underestimated so much that the denominator of the RAO in the numerical prediction is still smaller than the experimental result. Because the wave load was smaller it has no effect on the RAO. At 0.75 $\frac{rad}{s}$ an overpredicted numerical wave load in combination with an underestimated radiation force causes the RAO to be overpredicted. In the remaining frequencies the discrepancies are governed by the wave load. Despite the discrepancies seen in damping which are still significant, these do not affect the radiation force such due to the dominance of the added mass.

At a submergence of 1.5 m, there are four data points available of which the data is presented in Table 4.2. The RAO at 0.52 $\frac{rad}{s}$ is predicted well as both the wave load and radiation force have a comparable deviation. The percent deviation of the wave load at 0.81 $\frac{rad}{s}$ seems like an influential difference. However, the wave load is so small compared to the radiation force, that the RAO is small in both experimental and numerical prediction. The experimental RAO is only slightly higher than its numerical equivalent, which also can be seen on Figure 4.2. What is interesting, that in the numerical simulation no damping is present at this frequency but at the experimental results it is. Although, it has almost no influence on the RAO due to the wave load, it is a notable difference. Lastly, the RAO at 1 $\frac{rad}{s}$ is overpredicted due to an overpredicted wave load. The effect of the overpredicted wave load is tempered by the overpredicted damping and added mass term. This causes the numerical RAO to be only 34.4% larger than the experimental RAO of 0.14 m.

Table 4.2: The experimental results at 1.5 m submergence for which RAO predictions are obtained including a percent deviation, %D, to the associated numerical data point. Data is, if applicable, given per meter width of the body

ω	RAO_{exp}	RAO_{num}	$\%D_{RAO}$	a_{exp}	$\%D_{addm}$	$\%D_{inertia}$	b_{exp}	$\%D_{damp}$	$F_{wl,exp}$	$\%D_{F_{wl}}$	$F_{rad,exp}$	$\%D_{F_{rad}}$
$[\frac{rad}{s}]$	[m]	[m]	[-]	[ton]	[-]	[-]	$[\frac{ton}{s}]$	[-]	$[\frac{kN}{m}]$	[-]	$[\frac{kN}{m}]$	[-]
0.52	1.06	1.08	2.1%	-973.5	15.1%	28.3%	432.8	2.8%	285.0	10.7%	346.0	10.1%
0.63	1.14	1.42	24.7%	-359.8	24.2%	-91.7%	186.8	14.9%	139.2	38.3%	185.1	20.5%
0.81	0.02	0.006	-71.6%	351.1	-23.8%	-10.4%	970.8	-99.9%	11.6	-80.8%	242.6	-27.9%
1.00	0.14	0.18	34.4%	362.4	11.0%	4.9%	198.1	47.7%	114.9	48.5%	413.0	20.4%

The deviations in RAO at 5 m submergence are both in the lower frequency range. These deviations are due to an underestimation of the wave load, as shown in Figure 4.8. These underestimations are due to the sensitivity of the test set-up, which allowed a small pendulum movement during the captive tests that resulted in a reduction of the exposed wave load. At larger submergences, a combination of increased force and larger arm around the suspension structure above the model caused higher deviations. Also, when considering the predictions of hydrodynamic coefficients at 5 m submergence, almost all data points match, see Figure 4.5. Only at 0.253 and 0.44 $\frac{rad}{s}$, deviations in both the damping and added mass coefficient are present. The reason is thought to be due to a deviation in phase angle as a result of the sensitivity of the used fit function, as explained in section 3.4. Therefore, the motion prediction at 5 m submergence is assumed to be correct.

Overall can be concluded that discrepancies for the wave load are dominant for the deviations in heave RAO, except for the frequency at which a ≈ -m. A graphical representation of the percent deviations over frequency domain is shown in Figures 4.3 and 4.4. At higher frequencies inertia becomes dominant over damping and damping deviations affect the RAO less. Nevertheless, the damping terms still deviate from the numerical predictions and much more than the, at higher frequencies, dominant inertia term.

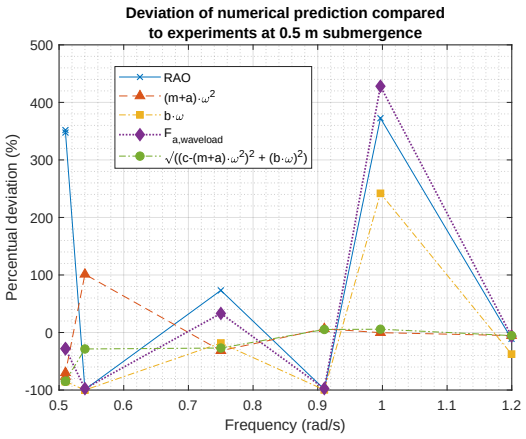

Figure 4.3: Visualisation of the deviations of each term at 0.5 m submergence

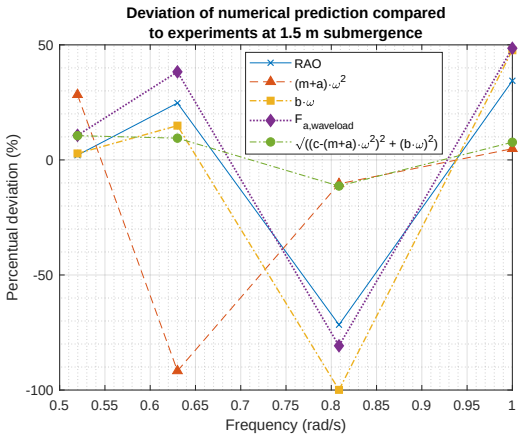

Figure 4.4: Visualisation of the deviations of each term at 1.5 m submergence

4.1.2. Physics-related motives for discrepancies

The reason why the hydrodynamic coefficients and wave loads deviate from the numerical data can now be discussed, since the cause of the RAO discrepancy at each frequency is known. First the results for the hydrodynamic coefficients are discussed and afterwards the wave load. In this section the reasoning will be based on the experimental data. The shown figures have a limited range to make them better readable. The complete figure without adjusted axes-limitations can be found in Appendix D.

Hydrodynamic coefficients

The results for added mass, shown in Figure 4.5, fit the numerical prediction relatively well, except for the smallest two frequencies at 1.5 m submergence. The rapid fluctuations, such as between 0.25 and 0.35 $\frac{rad}{s}$ at 1.5 m submergence, are due to the influence of the potential energy of the fluid that is more important compared to deeper submergences [21]. The potential energy of the fluid is related to the fluid velocities at the free surface that become more significant. Furthermore, a noticeable hump is seen in added mass around 0.55 $\frac{rad}{s}$ for 0.5 m in the numerical prediction. Right in front of the location of this hump, the largest deviations in RAO are located. It can also be seen in the damping coefficient graph, that there is a large deviation in damping at this frequency.

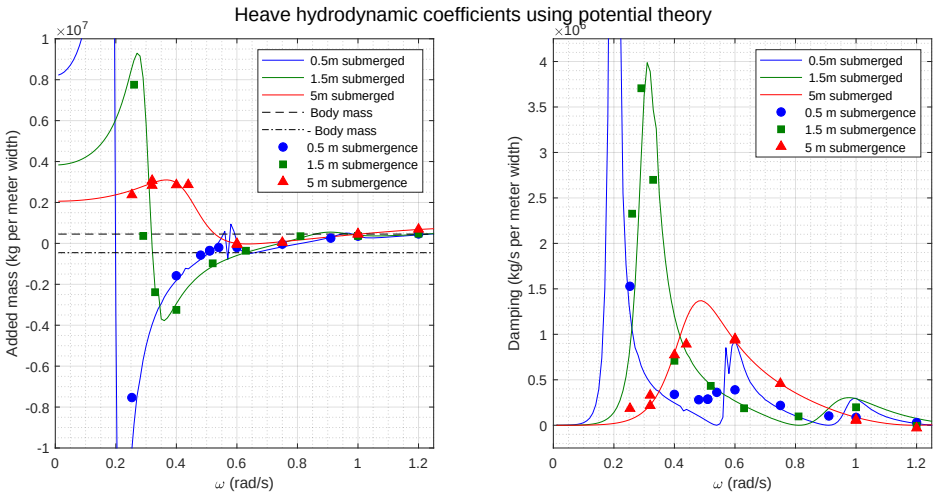

Figure 4.5: Comparison of the numerical results, solid lines, compared to the experimental data, markers, for hydrodynamic coefficients in heave

In linear diffraction theory only pressure related forces are present. Thus, damping is dominated by the generation of waves and viscous effects are neglected. Therefore, no waves should be expected according to linear diffraction theory at the frequencies at which damping reduces to zero. Though, when investigating

the surface elevation at 0.54 and 0.91 $\frac{rad}{s}$ at 0.5 m submergence and 0.81 $\frac{rad}{s}$ at 1.5 m submergence, surface elevations were both measured and visually observed. In Figure 4.6, the measured surface elevation, after filtering, is shown for the data point at the first zero prediction in the numerical damping coefficient for both 0.5 and 1.5 m submergence. In the figure the measured elevation on top of the model is shown. This measurement is performed exactly in the middle of the top plate. The measurement is relative to the model as the sensor is fixed in the model. The signal is compensated for the model motion to retrieve surface elevation relative to the global coordinate system. Motion compensation is done by subtracting the model motion from the measured signal. The lack of supposed damping as well has its impact on the frequencies located around the location where no damping is predicted. This can be seen at the predicted damping coefficients between 0.4 and 0.6 $\frac{rad}{s}$, which are all showing discrepancies. The measured surface elevation is a proof that a damping coefficient should be present in the numerical prediction and that the measured damping is not a result of viscous effects alone.

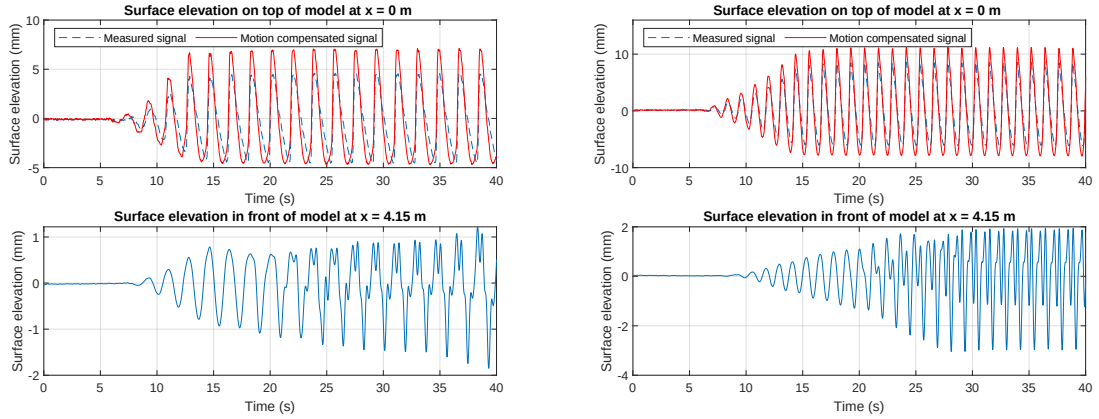

(a) s = 0.5 m, ω = 0.54 $\frac{rad}{s}$, $x_{a,modelscale}$ = 2.5 mm, $x_{a,fullscale}$ = 0.1 m, first 40 seconds

(b) s = 1.5 m, ω = 0.91 $\frac{rad}{s}$, $x_{a,modelscale}$ = 2.5 mm, $x_{a,fullscale}$ = 0.1 m, first 40 seconds

Figure 4.6: Surface elevation at frequencies where no damping coefficient is predicted, measured on top and in front of the model

In the surface elevation signals shown in Figure 4.6, higher harmonics can be seen. At the surface elevation top of the model an increased peak is observed that is consistently present over time in the motion compensated signal. This peak is caused by the intersection of the waves which are generated as a result of the water flow onto the model at both model ends. Besides that, higher harmonic waves were also created at

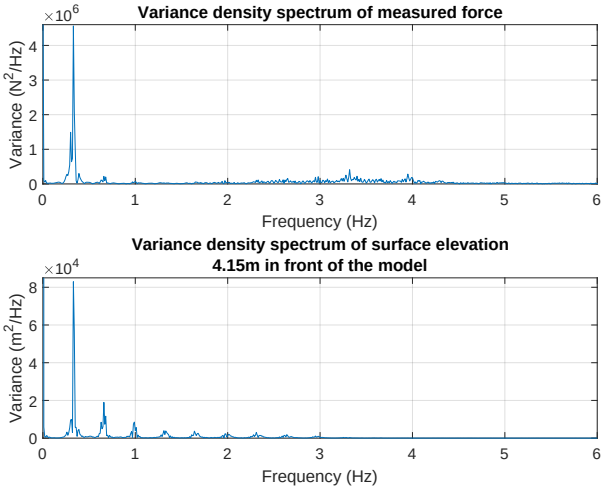

Figure 4.7: Variance density spectrum of force signal and surface elevation signal in front of model showing higher harmonics of a test at s = 1.5 m, ω = 0.33 $\frac{rad}{s}$, x_a = 0.1 m

the transmission from the shallow water region, on top of the model, to the deep water region, aside of the model. This is also seen in the measurement at the external surface elevation sensor. It, however, also has been found that these higher harmonics have hardly any effects on the measured force signal. This can also be seen when looking at the variance density spectra in Figure 4.7, in which both a force signal and accompanied surface elevation signal are analysed.

Wave loads

The measured wave loads can be seen in Figure 4.8. As already observed in the presented data in Table 4.1, there is no to hardly any wave load predicted at the RAO discrepancies at 0.54 and 0.91 $\frac{rad}{s}$ for 0.5 m submergence. This has a significant influence on the RAO, since the wave load is dominant at nearly all discrepancies in RAO, as concluded in subsection 4.1.1. It is interesting that at both frequencies where the wave load is predicted to be zero, also the damping is predicted to be zero. The same boundary conditions are met by both types of simulations as they have a related system. The only difference is the origin of the energy entering the system. It is therefore also not surprising that when no wave related force is predicted in one of the simulations, that there is a high probability that in the other simulation this force is not predicted either McIver [20] confirms that this often coincides in this manner, but not necessarily always. For instance, it can also be seen that at 0.81 $\frac{rad}{s}$, a correct wave force is predicted where the damping is overpredicted. As with damping, the data point at the frequencies after both zero predictions is overpredicted by the numerical BEM. These results show that the result for damping coefficient can be a proper indicator whether a wave load is predicted correctly and vice versa.

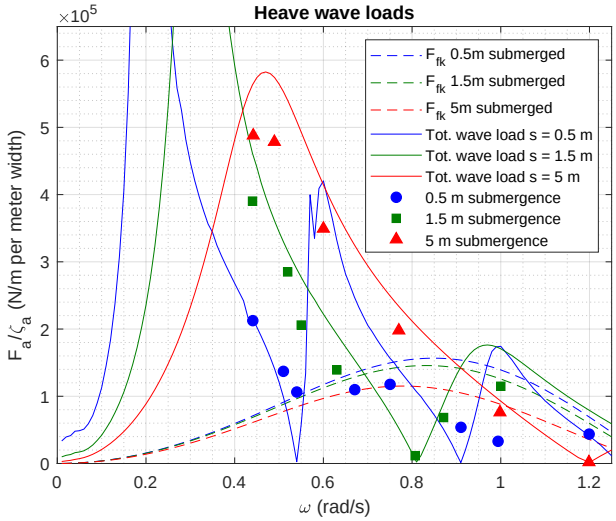

Figure 4.8: Comparison of the numerical results, solid lines, compared to the experimental data, markers, for wave load in heave

In Figure 4.9 the time domain signals corresponding to the underpredicted RAO at 0.54 $\frac{rad}{s}$ for 0.5 m submergence are given. In the wave load signal, Figure 4.9a, it is interesting to see that the numerically predicted phase angle $\epsilon_{F,\zeta}$ is -2.96 rad, while the phase angle of the experimental data is 0.10 rad. This means that when there is a numerical maximum, there is an experimental minimum almost at the same location. Furthermore, as can be seen there, nearly no wave load is predicted by theory while the test results show that there is actually a wave load present. No higher harmonic waves are reflected from the model as can be seen in the bottom figure. In Figure 4.9b, the time domain signal for the oscillation at this point can be seen. The deviation in phase angle and force are purely due to the lack of damping. The neat displacement signal is shown in the bottom figure. The higher harmonics at the minima and maxima of the force signal are due to the sensitivity of the setup, as explained in subsection 3.3.1.

Concluding remarks

It is clear from the time domain signals, in combination with the observed surface elevation, that in linear diffraction theory physical phenomena, that satisfy the boundary conditions, are not predicted. The smaller the submergence becomes, the larger the deviations. Based on these experiments it can be concluded that linear diffraction theory is not applicable to predict the vessels motions at these frequencies. Robertson [29]

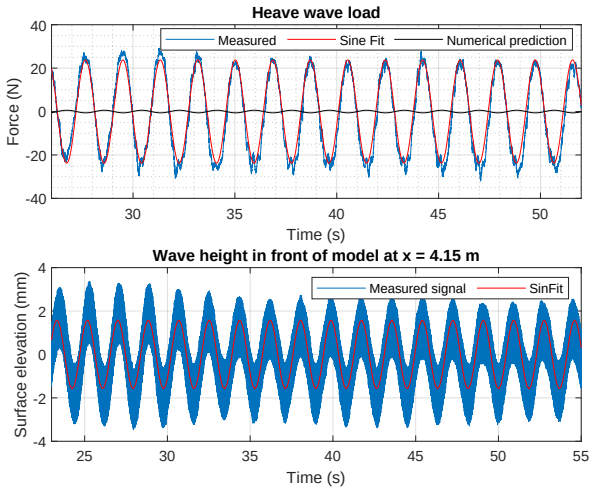

(a) Measure wave force for an undisturbed $\zeta_a = 0.13\ m$, fitted time domain

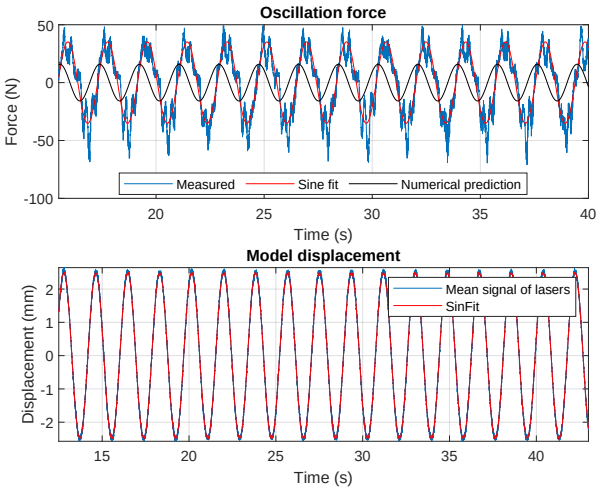

(b) Measured heave oscillation force for $x_a = 0.1\ m$, fitted time domain

Figure 4.9: Time domain signals of the captive test and forced oscillation test at 0.5 m submerged and $\omega = 0.54\ \frac{rad}{s}$, corresponding predicted numerical RAO of 0.004 $\frac{m}{m}$

stated already that there are regions for which a Green's function does not exists. A region has been found in which the used Green's function is not applicable, although it satisfies the boundary conditions. Further research to other numerical models is needed to see whether a Green's function in general is not applicable for an inconvenient draft situation, or that it is only the one by Wehausen and Laitone [36]. An alternative solution is by developing an alternative BEM in which, next to the model, the free surface, sea bottom and sides of the fluid domain are discretised. This is a boundary element method based on the work of Yeung [38].

4.1.3. Poles in the complex frequency domain

Multiple indications have been found in literature that can illustrate what goes wrong in mathematics behind the numerical modelling. Unfortunately, the author's mathematical knowledge is not sufficient to prove the upcoming indications. They are still discussed as it can give relevant insights for this and further studies.

There is a strong suspicion that poles in the complex frequency domain are a cause of the discrepancies in the hydrodynamic data as a result of the used Green's function. Linton and Evans [17] state that a result of a singularity is that the damping coefficient goes to zero. Exactly at the locations where the damping goes towards zero, a discrepancy is seen. This is true at both 0.5 and 1.5 m submergence. Linton and Evans [17] also noticed that it is easier to observe singularities when presenting the coefficients in the complex plane. Added mass and damping are a representation of the hydrodynamic radiation force. Jefferys [12] found that there is a certain dependency between the two coefficients which makes them better predictable when plotting them in the complex plane.

In Figure 4.10, a representation of the hydrodynamic coefficients in complex domain is shown, with each data point representing a frequency step. The large circle represents the low frequency part, for increasing frequencies smaller and smaller circular motions can be seen. The relation between added mass and damping is relatively similar over submergence range. Therefore, it is not surprising that a hump in added mass has been observed at the locations where damping goes to zero.

When comparing this to the experimental results, at locations where damping was underpredicted it, the added mass was overpredicted. For frequencies at which negative added mass occurs, an overprediction means that the numerical value is less negative than the experimental value or even a positive value. Farina [8] concluded that the added mass is related with poles in the complex frequency domain. This can be a reason why the added mass seems to be affected when the damping goes to zero and a pole is suspected. Moreover, Farina [8] also concludes that there is a high probability that a rapid fluctuation, as at 0.2 rad/s for 0.5 m submergence, contains a pole.

The discrepancies in the wave loads can be a result of poles in the complex plane too. Namely, McIver [20] concludes that often, but not by definition, a pole in the diffraction potential has a corresponding pole in

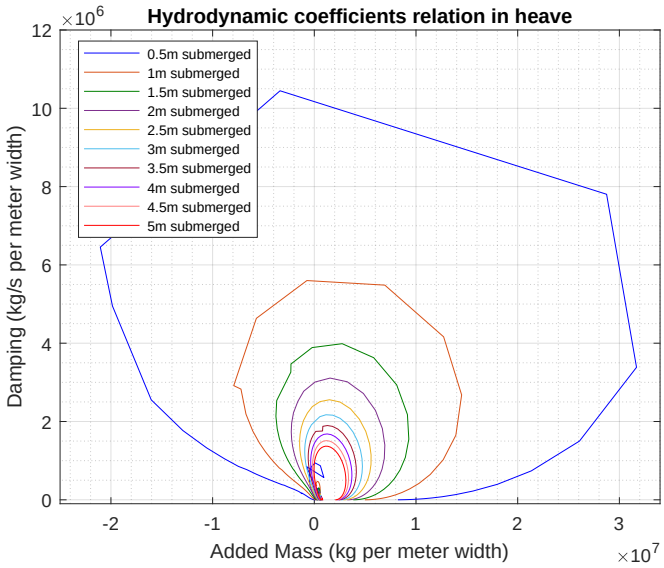

Figure 4.10: Graphical representation in the complex plane of the relation between added mass and damping over the frequency domain

the radiation potential. This would therefore also explain why the experimental wave load deviates from the numerical prediction at 0.54 and 0.91 $\frac{rad}{s}$ at 0.5 m submergence and not at 0.81 $\frac{rad}{s}$ at 1.5 m submergence. A reason why data points around the frequency of poles also show discrepancies, is that a pole also affects the data at the frequencies surrounding it.

In literature unrealistically high surface elevations are, as raised in section 1.4, often mentioned as a reason for the overpredicted motions. The surface elevations are determined using the radiation and diffraction potential. It is therefore interesting that McIver [20] found that the unrealistic surface elevations are caused by poles. On top of that he adds that poles specifically occur by analysing the wave loads separately from the radiation forces and occur when a portion of the free surface is restricted. Restrictions occur between side-by-side structures [7], a torus [24] and apparently also for a large body submerged in close proximity to the free surface.

4.2. Pitch hydrodynamic coefficients

Pitch forced oscillation tests were performed to study the rotational motion. An extra motivation for the pitch tests, is the possibility to better examine the global extremes at the smallest submergences compared to heave tests. Also in this section are all results given for the smallest amplitude. The smallest oscillation amplitude is 0.55°. The hydrodynamic data is given two-dimensional.

The results for the hydrodynamic coefficients are shown in Figure 4.11, a representation without a limited range is shown in Appendix D. Immediately it is noticeable that, for both added mass and damping, the numerical extremes around 0.38 $\frac{rad}{s}$ at 0.5 m submergence are not met by the experimental data. At this submergence, the numerical global maximum and minimum added mass coefficients are located at 0.37 and 0.39 $\frac{rad}{s}$, and the maximum damping coefficient is located at 0.38 $\frac{rad}{s}$. Four repetition test were performed at a frequency of 0.37 $\frac{rad}{s}$. First of all, these results emphasise the discrepancy at a frequency of which Farina [8] noted that it can be affected by a complex pole. In addition, the results of the repetition tests show effect of the sensitivity of the phase angle in the sine fit mentioned in section 3.4.

In the figure, lines have been added representing the mass moment of inertia around the center of rotation both positively and negatively. At the heave motion prediction, it has already been found that a peak in RAO is found around the frequency at which the negative added mass equals the mass of the body. The same observation can be made for the pitch RAO of which the numerical prediction is shown in Figure 4.12. The peaks in RAO at a submergence of 0.5 and 1.5 m are both located at the frequency where the added mass a $\approx -I_{yy}$.

In the subplot for damping, in Figure 4.11, the damping coefficient reaches zero after numerical peaks

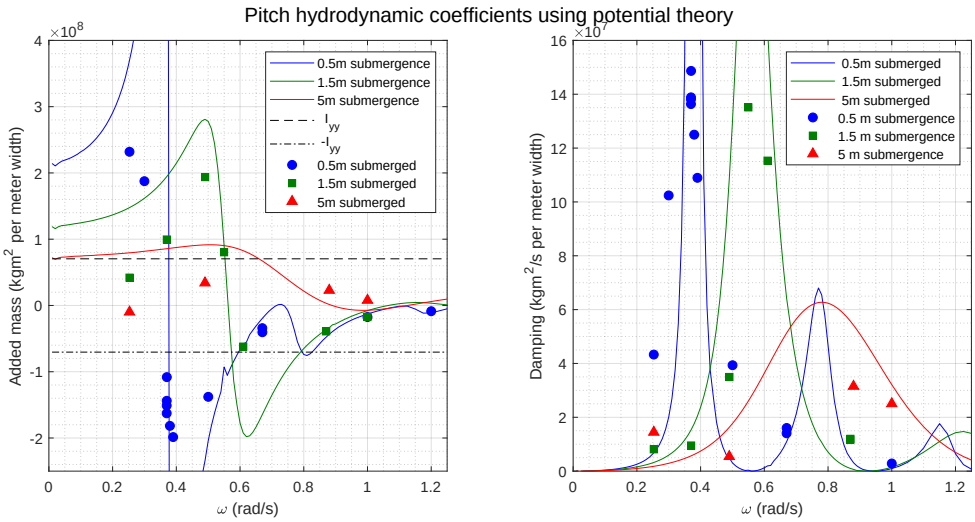

Figure 4.11: Comparison of the numerical results, solid lines, compared to the experimental data, markers, for hydrodynamic coefficients in pitch

at both 0.5 and 1.5 m submergence. In contrast to heave, the locations at which damping reaches zero are not well reflected in the RAO. This can be a result of the dominance of the wave load, as observed in subsection 4.1.1. However, it is still interesting to check the surface elevation at a location where nearly no damping is predicted.

In Figure 4.13, the surface elevation corresponding the data point at 0.5 $\frac{rad}{s}$ at 0.5 m is shown. At this frequency the experimental value for the damping coefficient is 3058.3 $\frac{tonm^2}{s}$, while the numerical prediction is more than ten times as large, 39338.7 $\frac{tonm^2}{s}$. For the surface elevation measurement on top of the model, the motion is compensated by multiplying the measured surface elevation at each time step with the cosine of corresponding angle of the model at that time step. No translation for location is taken into account, because the used sensor is located above the center of the cross-section. Barely a difference with the measured signal is seen due to the small angle of rotation. More important, noticeable surface elevations have been measured and visually observed. Also small higher harmonic waves can be seen at the external surface elevation signal. Surface elevations are also measured and observed at a frequency of 0.87 $\frac{rad}{s}$ at 1.5 m, where the numerical predicted damping is also very small. Rotational tests are more prone to viscous related forces than transnational tests. However, the observed and measured surface elevations are such that can be concluded that a damping coefficient should be more significantly present than results from linear diffraction theory.

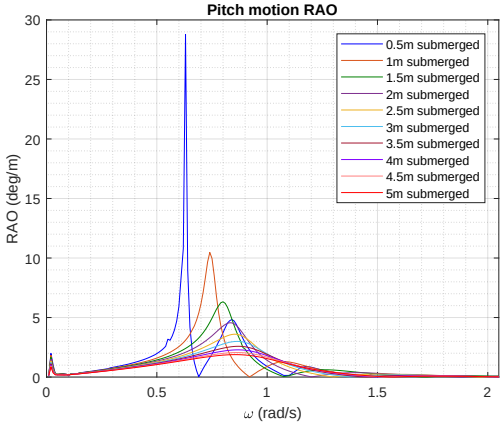

Figure 4.12: Pitch motion RAO over submergence range resulting from diffraction theory

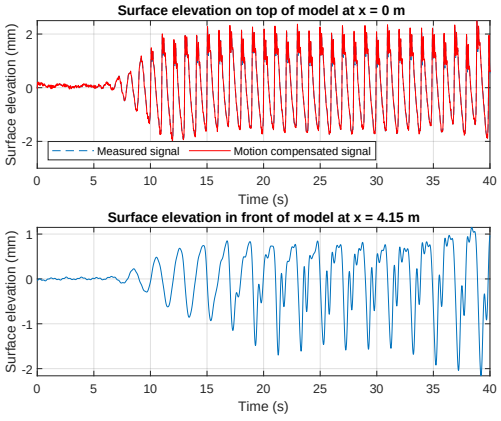

Figure 4.13: Surface elevation at s = 0.5 m, ω = 0.50 $\frac{rad}{s}$ and θ_a = 0.56°, almost no damping is predicted at this frequency

At a submergence of 1.5 m, the experimental data of the hydrodynamic coefficients follows the trend

of the numerical predictions. The interesting aspect is that at the numerical peak around 0.55 $\frac{rad}{s}$ also an experimental peak is located, despite the extremes being smaller. It is a bit unexpected that the results at 5 m submergence do not match the numerical predictions. This can indicate that discrepancies are more present in rotational motions than to heave motions. However, this can as well be a result of viscous effects.

A closer look is taken of a deviation at 1.5 and 5 m submergence in Figure 4.14. Both represented tests are at a frequency of 0.49 $\frac{rad}{s}$, and in both tests the numerical prediction has a larger magnitude than the experimental result. At 1.5 m submergence, Figure 4.14a, a clear phase shift is seen. This means that aside from the force amplitude, the ratio between the real and imaginary part of the radiation force, represented in added mass and damping, is incorrect. At 5 m submergence, Figure 4.14b, only a slight phase shift is seen which is almost negligible. The overestimation of force is not due to the mass moment of inertia. If it was, the damping coefficient, which is determined independently of inertia, should have matched the numerical value. This data point is located in the global peak of the damping coefficient, which is numerically overestimated, see Figure 4.11. As a result, the force amplitude at this frequency is also overestimated. Due to the smaller force amplitude of the applied moment at 5 m submergence, noise is pro rata more present in Figure 4.14b compared to Figure 4.14a.

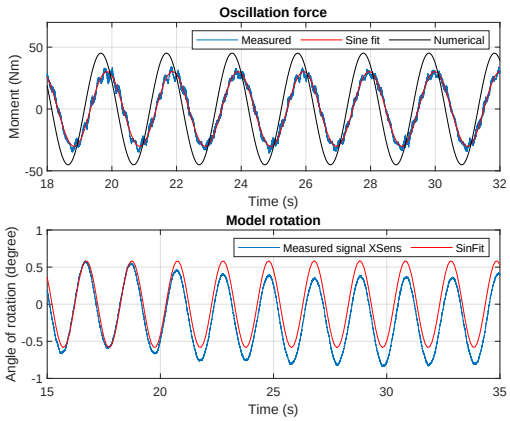

(a) s = 37.5 mm, ω = 0.49 $\frac{rad}{s}$ and $\theta_{a,measured}$ = 0.587 rad
$F_{a,num}$ = 45.1 Nm, $F_{a,exp}$ = 30.2 Nm

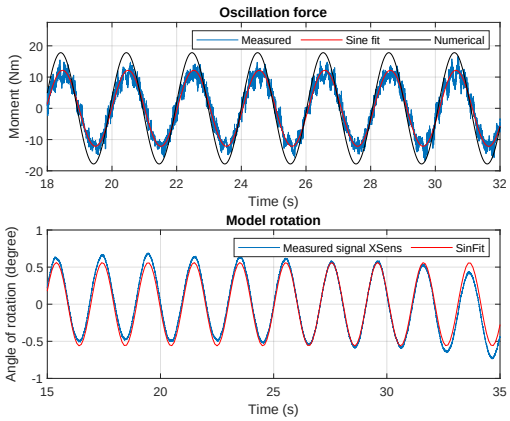

(b) s = 5 m, ω = 0.49 $\frac{rad}{s}$ and $\theta_{a,measured}$ = 0.563 rad
$F_{a,num}$ = 17.8 Nm, $F_{a,exp}$ = 12.1 Nm

Figure 4.14: Time domain representation of the force signal during pitch forced oscillation tests including the harmonic fit and numerical prediction converted to time domain

Lastly, it is notable that the lower frequency limit of the added mass for both pitch and heave increases significantly for smaller submergences, see Figures 4.5 and 4.11. The reason is that, as shown in subsection 1.3.2, the free surface is modelled as a solid wall in the low-frequency limit when using the Green's function by Wehausen and Laitone [36]. The same phenomenon is seen at the lower frequency limit of the heave wave load in Figure 4.8. Discrepancies are expected at the lower frequency limit as both, Brennen [1] and De Boer and Buchner [5], concluded that results for hydrodynamic data computed using potential flow theory for an object in close proximity to a wall are deviating from reality due to lack of viscosity. Besides, the correctness of modelling the free surface at the low frequency limit as a solid wall is at all debatable.

4.3. Free surface damping

Currently, a conservative approach that makes use of free surface damping is applied to predict the motions of a SSCV at inconvenient draft. Theoretically, this modification is only valid for small values of damping lid ϵ as the damping lid represents a fictitious internal force proportional to the fluid velocity in opposite direction [2]. The effect of free surface damping on the damping coefficient and wave load, both in heave, is shown in Figure 4.15. In the figure also data points for larger amplitudes are presented. These will be discussed in section 4.4.

For both heave and wave load a damping lid of 0.6 is not sufficient, while this is already a large value for a damping lid. A damping lid of 2.0 shows better convergence, however there are still deviations seen with almost all frequencies. In an extreme case of ϵ = 10.0, it can be seen that the damping coefficient will not reach values that are initially quite overestimated. Example of this is for both damping and wave load the data point

at 1 $\frac{rad}{s}$ with the smallest amplitude. But it is also already questionable at 0.6 $\frac{rad}{s}$ for damping and 0.67 $\frac{rad}{s}$ for the wave load. It is interesting to see that at increasing damping lid values the damping coefficient graph goes away from the data without damping, while the wave force tends to cover the mean.

Van Winsen et al. [33] have already shown that the wave load can not be predicted well using a damping lid. In this study the same observation is made based on experimental data, and the same conclusion is made too for the damping coefficient. The use of a damping lid reduces the sometimes severe discrepancy. However, it does also affect data which was initially predicted correct, such as for damping at 0.75 $\frac{rad}{s}$. Therefore, it can be concluded that purely the use of damping lid will not result in the correct answer.

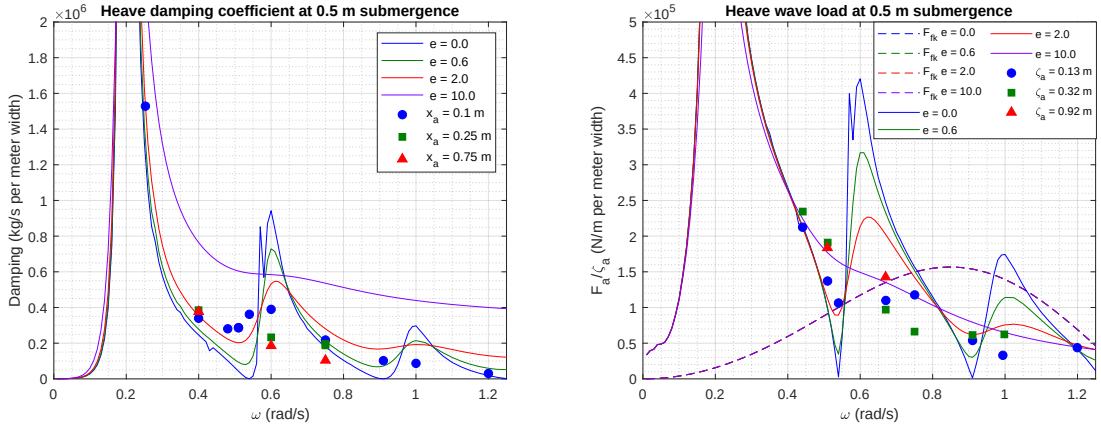

(a) Damping Coefficient

(b) Wave load

Figure 4.15: Free surface damping applied at the heave damping coefficient and heave wave load for submergence of 0.5 m, damping lid ϵ is presented as the letter e in the legend

4.4. Nonlinear effects

Larger oscillation and incident wave amplitudes have been applied during tests in order to gain insights on the effect of possible nonlinearities. All larger amplitude figures can be seen in Appendix D.

At smaller submergences, smaller amplitudes are needed in order to discover nonlinearities. It can already be seen in Figure 4.15 that the data at larger amplitudes of 0.25 m and 0.32 m is affected nonlinearities. This is a result of the waves on top of the floater that showed solitary wave behaviour and started breaking. In addition, viscous are effects are present at the largest oscillation amplitude because the amplitude of 0.75 m is larger than the submergence of 0.5 m. It was observed that these oscillations were still too small to actually dry out the top of the floater. Nevertheless, the measured force remained harmonic. Though, it was seen that the amplitude of the did not scale in a linear way. This especially happened when wave breaking started to occur.

The results for hydrodynamic coefficients and wave loads at 1.5 m submergence are shown in Figs. 4.16 and 4.17. The hydrodynamic coefficients already show a pretty harmonic behaviour except for the test at 0.75 m amplitude at 0.4 $\frac{rad}{s}$, which is discussed later this section. The wave load is less linear at this submergence. Slight offsets are seen for increasing wave amplitudes as a result of wave breaking on top of the model.

At 5 m submergence the same observations can be made at a larger amplitude. The figures can be seen in Appendix D, as well as the results for pitch. The pitch results did not lead to different insights compared to the already discussed matter.

When wave breaking occurred, and also at the largest amplitude force oscillation tests, often the force signal had a translation along the force-axis. This is shown in Figure 4.18, in which the mean of the signal is annotated with the thick red line. The first impact of the incident wave with an amplitude of 0.31 m is at 32 seconds. Right after the wave with a frequency of 0.87 $\frac{rad}{s}$ starts breaking, which results in a vertical translation of the mean of the force. At approximately 87 seconds the wave train has passed the model and the remaining loads are a result of reflected waves. Wave breaking impact also results in a higher harmonic force signal. Therefore, for the tests with a larger amplitude can be debatable if a harmonic fit is still suitable. The harmonic fits have been made around the translated mean of the signal.

Then the test at 0.4 $\frac{rad}{s}$ for 1.5 m submergence with an oscillation amplitude of 0.75 m. A notable phe-

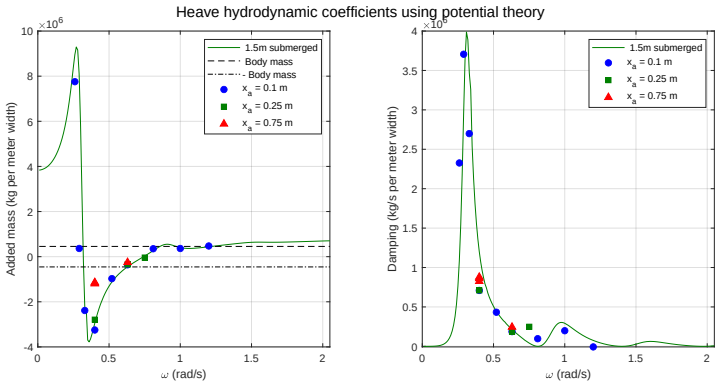

Figure 4.16: Heave hydrodynamic coefficients at 1.5 m submergence including the experimental results with a larger amplitude

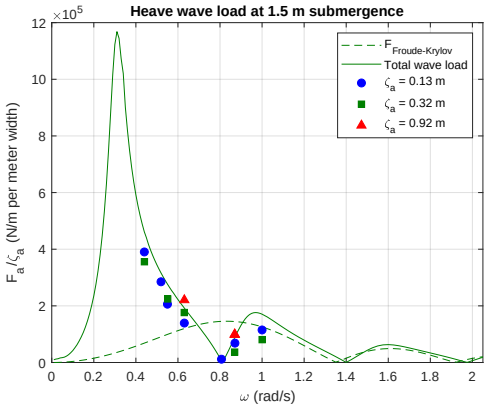

Figure 4.17: Heave hydrodynamic coefficients 1.5 m submergence including the experimental results with a larger amplitude

nomenon was observed during this test, which was not present in any of the other tests. The interaction between the deep water radiated wave and the undeep water radiating wave off the top of the model, resulted in a suction gap when the model is at its highest position. A visualisation from the camera footage can be seen at the left side of Figure 4.19. At the right side of the figure air captured in the gap arises as bubbles once the model moves downwards. Besides a different force amplitude, also a change in phase angle is observed compared to the smallest tested amplitude. The force amplitude became 5.4 times as large, i.e. 457.6 N versus 84.32 N, and the phase angle shifted 0.66 rad, in other words from -2.58 to -1.92 rad. The force amplitude became 5.4 times as large, while the measured oscillation amplitude became 7.9 times as large, thus as expected it is not linear anymore.

That the system is nonlinear is seen in the hydrodynamic coefficients, the damping coefficient remains almost the same while the added mass coefficient increases significantly, see Figure 4.11. The shift in damping coefficient is from 709 $\frac{ton}{s}$ at $x_a = 0.1$ m to 860 $\frac{ton}{s}$, and the shift in added mass from -3245 ton at $x_a = 0.1$ m to -1173 ton. Examining these differences in this manner, it seems that the suction gap creates a reduced viscous resistance as there is a mixture of water of air along the sides of the model. This reduces the in phase force contribution which is represented via the added mass coefficient. It is expected that this phenomenon can also occur at other submergences with combinations of frequency and oscillation amplitude which have not been tested. As this test has been repeated twice and showed exactly the same phenomenon at the rep-

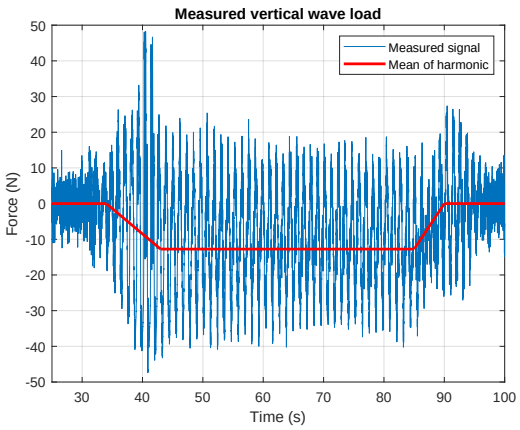

Figure 4.18: Heave waveload at s = 1.5 m, $\omega = 0.87$ $\frac{rad}{s}$ and $\zeta_a = 0.31$ m, harmonic vertical translation due to wave breaking

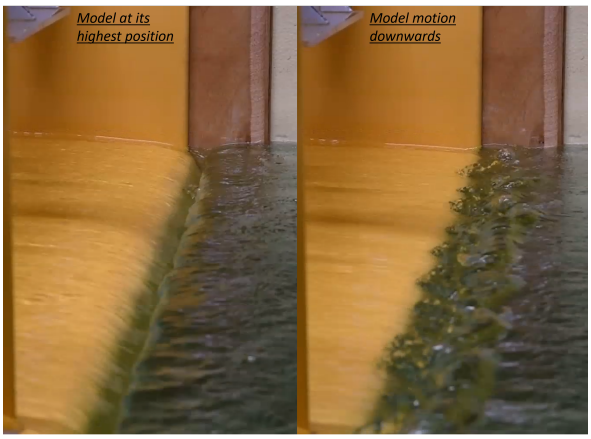

Figure 4.19: Water behaviour at s = 1.5 mm, $x_a = 0.75$ mm and $\omega = 0.4$ $\frac{rad}{s}$.
Left: a suction gap forms alongside edge of undeep-deep water regime when model is at its highest position.
Right: Air captured in suction gap rises and bubbles form when model moves down.

etitions, it can be argued that if this phenomenon arises in practice that it reduces the radiation force which may cause the RAO to increase with the assumption that the wave force remains the same.

Overall, it can be concluded that data at 0.5 m is sensitive for nonlinearities when oscillation or wave amplitudes increase. Furthermore, the wave load is more prone to non linear effects than the hydrodynamic coefficients due to wave breaking effects. When viscous effects occur, such as wave breaking, the force signal can make a vertical translation along the force-axis.

5

Conclusions

During operation, situations occur where a Semi-Submersible Crane Vessel (SSCV) has to reduce its draft to what is called inconvenient draft. At this draft, the floaters are submerged in close proximity to the free surface. At this draft, motion prediction using linear diffraction theory shows discrepancies compared to the actual motions of the vessel. A proper motion prediction is required to ensure a safe execution of the offshore operation. The key issue is the submerged part of the floater, since discrepancies occur as soon as there is only a small water column on top of the floaters. The reason why this leads to discrepancies in the motion RAO is not yet known. In addition, qualitative hydrodynamic data should be gathered for an object submerged in close proximity of the free surface. A two-dimensional cross-section of an SSCV-floater has been used to answer the following research question in this thesis:

> "What is, based on experimental data, the cause of the discrepancies in motion RAO calculated using linear diffraction theory for an object submerged in close proximity to the free surface?"

Model tests have been performed at to gather data for heave of the added mass, damping and wave load of a body in close proximity to the free surface and for pitch of the added mass and damping. The heave data was then redirected to a motion RAO. These results have been compared to the results of numerical simulations. This led to the following conclusions.

Based on experimental data can be concluded that linear diffraction theory does not predict physical phenomena that satisfy the boundary conditions and that underlie principles of the theory. Despite the fact that the experimental data does satisfy the boundary conditions of the numerical simulation, discrepancies occur at the hydrodynamic coefficients and wave load. The RAO is calculated using the hydrodynamic coefficients and wave load. Thus can be concluded that linear diffraction theory malfunctions at the inconvenient draft region, and therefore is not the correct theory to determine RAOs for an object on inconvenient draft. For a semi-submersible, the magnitude of the discrepancies is expected to be tempered due to the presence of the surface piercing columns.

Numerically, no potential damping and wave loads are predicted at frequencies where experimental data demonstrates that they should be present. Additionally, experimental data reveals that the potential damping and wave load data is overestimated at the frequencies subsequent these zero predictions. There are also deviations in the predicted added mass. Due to the relation between added mass and damping, these are mostly seen at the frequencies where damping causes a discrepancy. However, the discrepancies of added mass are less significant than for the damping coefficient and wave load.

Discrepancies in motion RAO are found to be dominated by the discrepancies the wave load, except for the frequency at which the added mass equals negative inertia of the body. At these frequencies the absence of the inertia term in the calculation of the RAO causes a, sometimes, significant peak. At higher frequencies inertia becomes dominant over damping and damping deviations affect the RAO less. Nevertheless, the damping terms still deviate from the numerical predictions and much more than the, at higher frequencies, dominant inertia term.

Result for the damping coefficient are found to be a proper indicator whether a wave load is predicted correctly and vice versa. Most of the times, experimental data showed discrepancies at the same frequency

for both wave load and damping. Nor was this surprising, given that both forces are related to waves. The simulation only has a different origin of the energy entering the system, given that both calculations satisfy the same boundary conditions. The amount of discrepancies are observed to increase at smaller submergence,

The pitch motion around the center of the cross-section does not represent a rotational motion about the same degree of freedom for an SSCV. However, it allowed to experimentally investigate the global numerical extremes. In addition, it led to the finding that it seems that the rotational data is more affected than the heave data.

There is a strong suspicion that poles in the complex plane are the cause of the discrepancies in the hydrodynamic data, which result of the used Green's function by Wehausen and Laitone [36]. This Green's function is implemented in the foremost computational programmes that make use of linear diffraction theory. This suspicion cannot be proven due to the insufficient mathematical knowledge of the author. However, characteristics of the numerical data in combination with findings in literature and the experimental data, accumulate to this suspicion.

For example, Linton and Evans [17] concluded that a property of a pole that the numerical damping goes to zero. On top of this, McIver [20] adds that a pole in the radiation potential often, but not by definition, has a corresponding pole in the diffraction potential. Both these characteristics were observed in the data at locations of the discrepancies. Furthermore, Farina [8] showed that the numerical global extreme in added mass and damping also tends to include a pole. The frequency associated with global extreme was too low to test in heave, but the numerical global extremes related to a pitch motion could be tested. Here, these predicted peaks were found to be present, but not as extreme as predicted in the numerical simulation.

Currently, an approach that makes use of free surface damping is applied to predict the motion of an SSCV at inconvenient draft. The applicability of free surface damping is analysed. Free surface damping reduces, as expected, the significance of the discrepancies. However, it does also affect data that is predicted correct without the use of surface damping. There are also data points which still do not correspond to the corresponding experimental data point after the use of free surface damping. Therefore, based on experimental data can be concluded that the use of free surface damping without further modifications does not result in an accurate motion prediction.

Lastly, the effect of nonlinearities when increasing the oscillation or wave amplitude. The wave load is found to be more prone to nonlinear effects than the hydrodynamic coefficients. At smaller submergences nonlinear effects start to occur at smaller wave and motion amplitudes. On top of that, the force signal can make a vertical translation along the force-axis when viscous effects occur, such as wave breaking. The force signal remained dominantly harmonic, but higher harmonic forces did show up. Furthermore, with the exception of most tests at the largest tested submergence, higher harmonic waves were measured and visually observed during the tests. These higher harmonic waves arose at the transition from the shallow to deep water regime and vice versa. These forces were found to have hardly any effect on the force signal.

6

Recommendations

The current study leaves a potential for further research. This potential is for follow-up study, but also for application in other areas of expertise and to investigate specific phenomena. The recommendations for further study are listed into three categories; recommendations related to the computational method, the test data and follow-up model tests.

Computational method

- A mathematical study to clarify whether the suspicion of complex poles is correct. This allows from a mathematical point of view to understand the cause of the discrepancies.
- Further research to other numerical models is needed to see whether a Green's function in general is not applicable for an inconvenient draft situation, or that it is only the Green's function by Wehausen and Laitone [36].
- Developing an alternative boundary element method in which, besides the model, also the free surface, sea bottom and sides of the fluid domain are discretised. This is a boundary element method based on the work of Yeung [38].

Test data

- Analyse the reflection and transmission coefficients over the submerged floater. A large amount of data is gathered, including video material, that can be used to analyse the wave propagation over the floater. This recommendation can also be useful for research into, for example, floating breakwaters.
- Investigate the phenomenon of negative added mass. In literature, not much experimental based research is found on the topic of negative added mass. The obtained data, in combination with the video footage, can be a proper starting point for a study to this special characteristic.

Follow-up model tests

- Perform extra wave load tests at lower frequency in order to capture the global extremes. In this study the lower frequency limit for captive tests was limited. Extra captive tests at lower frequencies will give relevant insights on the global extremes of the wave loads. Besides, it allows to make predictions for the lower frequent RAOs. During these the body must be restrained properly as the loads are expected be larger than in the current study,
- Perform extra forced oscillation and wave load tests at frequencies up to 2 $\frac{rad}{s}$ to see whether the damping coefficient and wave loads do start to match the numerical data or not at all. Extra data points can also be created in the tests frequency domain to get a more detailed overview in frequency domain. Make sure to actuate the model with multiple linear motors and an increased range of the force sensor, to make the setup less sensitive when it is exposed to even larger loads than in this study.
- Perform extra tests at other submergences, frequencies and larger amplitudes to get create a larger data set for validation of future models. In addition, a better overview of the possible nonlinear effects and their cause can be obtained.

Bibliography

[1] C.E. Brennen. A Review of Added Mass and Fluid Inertial Forces. Technical report, Naval Civil Engineering Laboratory, Port Hueneme, 1982.

[2] Xiaobo Chen. Offshore hydrodynamics and applications. The IES Journal Part A: Civil & Structural Engineering, 4(3):124–142, 2011. doi: 10.1080/19373260.2011.595903. URL http://www.informaworld.com.

[3] Jin S. Chung. Forces on Submerged Cylinders Oscillating Near a Free Surface. Journal of Hydronautics, 11(3):100–106, 1977. ISSN 0022-1716. doi: 10.2514/3.63081.

[4] Heerema Marine Contractors. Brent Alpha Jacket Removal, 2022. https://www.heerema.com/heerema-marine-contractors/offshore-decommissioning/brent-alpha Accessed: 12-02-2022.

[5] Gerrit De Boer and Bas Buchner. Viscous Damping of Vessels Moored in Close Proximity of Another Object. In Proceedings of The Fifteenth (2005) International Offshore and Polar Engineering Conference, pages 381–387, 2005. ISBN 1880653648. URL http://onepetro.org/ISOPEIOPEC/proceedings-pdf/ISOPE05/All-ISOPE05/ISOPE-I-05-295/1845982/isope-i-05-295.pdf/1.

[6] Rogier De Bruijn, Fons Huijs, Tim Bunnik, René Huijsmans, and Marc Gerritsma. Calculation of wave forces and internal loads on a semi-submersible at shallow draft using an iVoF method. In ASME 2011 30th International Conference on Ocean, Offshore and Arctic Engineering, Rotterdam, 2011. ASME. URL http://asmedigitalcollection.asme.org/OMAE/proceedings-pdf/OMAE2011/44397/175/4601628/175_1.pdf.

[7] D.V. Evans and R. Porter. Near-trapping of waves by circular arrays of vertical cylinders. Applied Ocean Research, 19:83–99, 1997.

[8] Leandro Farina. Water wave radiation by a heaving submerged horizontal disk very near the free surface. Physics of Fluids, 22(5):22–31, 5 2010. ISSN 1070-6631. doi: 10.1063/1.3403478. URL https://aip.scitation.org/doi/abs/10.1063/1.3403478.

[9] Yoshimi Goda and Yasumasa Suzuki. Estimation of incident and reflected waves in random experiments. In Coastal Engineering, pages 828–845, 1976.

[10] L.H. Holthuijsen. Waves in oceanic and coastal waters. Cambridge university press, 2010.

[11] Sa Young Hong, Bo Woo Nam, Nam Woo Kim, and Yoon Sang Cho. Investigation of Nonlinear Roll Motion Characteristics of a Shallow Draft Semi-submersible. International Ship Stability Workshop, 2013.

[12] E R Jefferys. Interpolation and extrapolation of hydrodynamic coefficients. Applied Ocean Research, 5 (3):145–149, 1983.

[13] Sheng-Chao Jiang, Wei Bai, Ankit Choudhary, Anis Hussain, and Wei Xu. Optimization of Heave RAO and Mean Drift Force on FourColumn Semi-submersible Hull in Waves. Proceedings of the Twenty-sixth International Ocean and Polar Engineering Conference, pages 1001–1008, 2016. URL http://onepetro.org/ISOPEIOPEC/proceedings-pdf/ISOPE16/All-ISOPE16/ISOPE-I-16-177/1336650/isope-i-16-177.pdf/1.

[14] Fritz John. On the motion of floating bodies II. Simple harmonic motions. Communications on Pure and Applied Mathematics, 3(1):45–101, 1950. ISSN 10970312. doi: 10.1002/CPA.3160030106.

[15] J.M.J. Journée and W.W. Massie. Offshore hydromechanics. CITG Section Hydraulic Engineering, second edition, 2008.

[16] Evy Kersalé. Math2620: Fluid dynamics 1. Course reader, School of Mathematics, University of Leeds, 2020.

[17] C. M. Linton and D. V. Evans. Hydrodynamic characteristics of bodies in channels. Journal of Fluid Mechanics, 252:647–666, 1993. ISSN 14697645. doi: 10.1017/S0022112093003921. URL https://doi.org/10.1017/S0022112093003921.

[18] P. A. Martin and L. Farina. Radiation of water waves by a heaving submerged horizontal disc. Journal of Fluid Mechanics, 337:365–379, 1997. ISSN 00221120. doi: 10.1017/S0022112097004989. URL https://doi.org/10.1017/S0022112097004989.

[19] Guy McCauley, Hugh Wolgamot, Jana Orszaghova, and Scott Draper. Linear hydrodynamic modelling of arrays of submerged oscillating cylinders. Applied Ocean Research, 81:1–14, 12 2018. ISSN 01411187. doi: 10.1016/J.APOR.2018.09.012. URL https://doi.org/10.1016/j.apor.2018.09.012.

[20] P McIver. Complex resonances in the water-wave problem for a floating structure. Journal of Fluid Mechanics, 536:423–443, 2005. doi: 10.1017/S0022112005005021. URL https://doi.org/10.1017/S0022112005005021.

[21] P McIver and D V Evans. The occurrence of negative added mass in free-surface problems involving submerged oscillating bodies. Journal of Engineering Mathematics, 18:7–22, 1984.

[22] Chiang C Mei. The applied dynamics of ocean surface waves, volume 1. World scientific, 1989.

[23] J. N. Newman. The approximation of free-surface Green functions. Meeting in honour of Professor Fritz Ursell, (Wave Asymptotics):107–135, 1991.

[24] J.N. Newman. The motions of a floating slender torus. Journal of Fluid Mechanics, 83(4):721–735, 1977. doi: 10.1017/S0022112077001426. URL https://doi.org/10.1017/S0022112077001426.

[25] J.N. Newman. Progress in wave load computations on offshore structures. In Invited Lecture, 23th OMAE Conference, Vancouver, Canada, http://www. wamit. com/publications, 2004.

[26] J.N. Newman, B. Sortland, and T. Vinje. Added Mass and Damping of Rectangular Bodies Close to the Free Surface. Journal of Ship Research, 28(4):219–225, 1984. URL http://onepetro.org/JSR/article-pdf/28/04/219/2230172/sname-jsr-1984-28-4-219.pdf/1.

[27] Harald Ottens and Alessio Pistidda. Motion RAO's of a SSCV at deep and inconvenient draft. In ASME 2015 34th International Conference on Ocean, Offshore and Arctic Engineering, St. John's, Newfoundland, 2015. URL http://asmedigitalcollection.asme.org/OMAE/proceedings-pdf/OMAE2015/56482/V002T08A043/2528605/v002t08a043-omae2015-41917.pdf.

[28] W.J. Parnell. Math34032: Greens functions, integral equations and applications. Course reader, Department of Mathematics, University of Manchester, 2013.

[29] James Mueller Robertson. Hydrodynamics in Theory and Application. Prentice-Hall, 1965.

[30] 3mE TU Delft. Towing tank no. 2. https://www.tudelft.nl/3me/over/afdelingen/maritime-and-transport-technology/research/ship-hydromechanics/facilities/towing-tank-no-2 Accessed: 23-09-2022.

[31] F Ursell, R G Dean, and Y S Yu. Forced small-amplitude water waves: a comparison of theory and experiment. Journal of Fluid Mechanics, 7(1):33–52, 1960. doi: 10.1017/S0022112060000037. URL https://doi.org/10.1017/S0022112060000037.

[32] J.A. Van Santen. Approximate Formulae for Calculating the Motions of Semi-Submersibles. Ocean Engineering, 12(3):235–252, 1985.

[33] Ivan Van Winsen, Job S Bokhorst, and René H M Huijsmans. Calculation of wave height dependent force RAO's on Submerged bodies in close proximity to the free surface. In ASME 2013 32nd International Conference on Ocean, Offshore and Arctic Engineering, Nantes, 2013. ASME. URL http://asmedigitalcollection.asme.org/OMAE/proceedings-pdf/OMAE2013/55317/V001T01A017/4427658/v001t01a017-omae2013-10340.pdf.

[34] Inc WAMIT. Wamit user manual version 7.4. WAMIT Inc.: Chestnut Hill, MA, USA, 2020.

[35] R.C. Weast. Handbook of Chemistry and Physics 53rd Edition. Chemical Rubber Company, 1972. URL http://jupiter.plymouth.edu/~jsduncan/courses/2012_Spring/Techniques/Exams/DensityOfWater-vs-Temp.pdf.

[36] J.V. Wehausen and E.V. Laitone. Surface Waves, volume 9. Springer-Verlag, 1960.

[37] F. M. White. Fluid Mechanics. McGraw-Hill series in mechanical engineering. McGraw Hill, 2011. ISBN 9780073529349.

[38] Ronald Wai-Chun Yeung. A singularity-distribution method for free-surface flow problems with an oscillating body. Technical report, College of Engineering, University of California, Berkeley, 8 1973.

A

Green's function

Linear differential problems, of which a general form is given in Equation A.1, can be easily solved for f(x) when y(x) and linear differential operator $\mathcal{L}$ are known. However, when the forcing term f(x) and the linear differential operator are known one can not directly calculate the values for y(x). To tackle that, a Green's function can be used. A Green's function is an inverse operator that depends on two points, point of interest $\vec{x}$ and point of the source $\vec{\xi}$.

$$\mathcal{L}y(x) = f(x) \tag{A.1}$$

An example of a linear differential problem is shown in Equation A.2 which represents a forced mass spring system. The derivation of each component in the linear differential problem is shown in Equations A.3-A.5.

$$m\frac{d^2x(t)}{dt^2} + \omega^2 x(t) = F(t) \tag{A.2}$$

$$\mathcal{L} = m\frac{d^2}{dt^2} + \omega^2 \tag{A.3}$$

$$y(x) = x(t) \tag{A.4}$$

$$f(x) = F(t) \tag{A.5}$$

A characteristic of the Green's function is the relationship with a dirac delta function $\delta(x)$ as given in Equation A.6. A dirac delta function is a function representing a concentrated pulse located at a single point and is often termed a generalised function Parnell [28].

$$\mathcal{L}G(\vec{x},\vec{\xi}) = \delta(\vec{x}-\vec{\xi}) \tag{A.6}$$

A property of the Dirac delta function is that it $\delta(x) = \delta(-x)$ and thus is symmetric. Therefore, it can be stated that $G(\vec{x},\vec{\xi}) = G(\vec{\xi},\vec{x})$. The Green's function for a specific problem can be constructed by satisfying the accompanied boundary conditions.

Green's theorem

Potential theory boundary element method solvers make use of Green's theorem as shown in Equation A.7

$$\iiint_\Omega (\phi\nabla^2 G - G\nabla^2\phi)\, d\Omega = \iint_{\delta\Omega} (\phi\frac{\partial G}{\partial n} - G\frac{\partial \phi}{\partial n})\, dS \tag{A.7}$$

Due to the conversation of mass, which is a Laplacian, the term $G\nabla^2\phi = 0$. The term $\phi\nabla^2 G$ can be rewritten when use is made of the definition of a Green's function as given in Equation A.6. In this term the Laplace operator is the linear differential operator, $\mathcal{L} = \nabla^2$. Implementing these two steps will alter the Green's theorem to Equation A.8.

$$\iiint_\Omega \phi(\vec{\xi})\delta(\vec{x}-\vec{\xi})\, d\Omega = \iint_{\delta\Omega} (\phi(\vec{\xi})\frac{\partial G(\vec{x},\vec{\xi})}{\partial n} - G(\vec{x},\vec{\xi})\frac{\partial \phi(\vec{\xi})}{\partial n})\, dS \tag{A.8}$$

This can be simplified due to the filtering property of a delta function as stated by Parnell [28] in Equation A.9.

$$\int_S f(\vec{\xi})\delta(\vec{x}-\vec{\xi})\,dS = \begin{cases} f(\vec{x}) & \vec{x}\in S \\ 0, & \vec{x}\notin S \end{cases} \tag{A.9}$$

Both $\vec{x}$ and $\vec{\xi}$ are on S, which will result in Equation A.10

$$\phi(\vec{x}) = \iint_{\delta\Omega} (\phi(\vec{\xi})\frac{\partial G(\vec{x},\vec{\xi})}{\partial n} - G(\vec{x},\vec{\xi})\frac{\partial \phi(\vec{\xi})}{\partial n})\,dS \tag{A.10}$$

Derivation of the Green's function for deep water

The following derivation based on the work of Wehausen and Laitone [36], extra clarification placed where needed. A stationary pulsating source at location (a,b,c) is considered, in which the vertical coordinate c < 0. Infinite depth has been assumed. The boundary conditions for potential theory are defined in Eqs. A.11 to A.15.

$$\nabla^2\phi_i = 0 \quad \text{except at (a, b, c)} \qquad i = 1,2 \tag{A.11}$$

$$\frac{\partial\phi}{\partial z} + K\phi = 0 \quad \text{at c} = 0, \quad K = \frac{\omega^2}{g} \qquad i = 1,2 \tag{A.12}$$

$$\Phi(x,y,z,t) = r^{-1}\cos\omega t + \Phi_0(x,y,z,t) \quad \text{where } \Phi_0 \text{ is harmonic for z<0} \tag{A.13}$$

$$\lim_{z\to-\infty}\frac{\partial\phi_i}{\partial z} = 0 \quad i = 1,2 \tag{A.14}$$

$$\lim_{R\to\infty}\sqrt{R}\left(\frac{\partial\phi_1}{\partial R} + K\phi_2\right) = 0, \lim_{R\to\infty}\sqrt{R}\left(\frac{\partial\phi_2}{\partial R} - K\phi_1\right) = 0 \tag{A.15}$$

The definition of are r can be seen in Equation A.16 and the definition of R is shown in Equation A.17,

$$r^2 = (x-a)^2 + (y-b)^2 + (z-c)^2 \tag{A.16}$$

$$R^2 = (x-a)^2 + (y-b)^2 \tag{A.17}$$

Assumption is made that Φ will have the form as in Equation A.18.

$$\Phi(x,y,z,t) = \left[r^{-1} + \phi_0(x,y,z)\right]\cos\omega t + \phi_2(x,y,z)\sin\omega t \tag{A.18}$$

The boundary condition in Equation A.13 is satisfied by Equation A.19.

$$\phi = Re(\Phi(x,y,z,t)) \tag{A.19}$$

The mathematical definition of a Fourier transform and its inverse are given in Equation A.20 and A.21. A potential $\phi(x,y,z)$ can be described as an inverse Fourier transform $\mathscr{F}^{-1}(\widetilde{\phi}(k,\theta,z))$, as shown in Equation A.22. The range for wavenumber k is adjusted to $[0,\infty]$ as the wavenumber is treated as a positive number. For the wave angle θ the range is $[-\pi,\pi]$, representing the angular domain.

$$\widetilde{f}(\omega) = \mathscr{F}(f(x)) = \int_{-\infty}^{\infty} f(x)e^{i\omega x}\,dx \tag{A.20}$$

$$f(x) = \mathscr{F}^{-1}(\widetilde{f}(\omega)) = \frac{1}{2\pi}\int_{-\infty}^{\infty}\widetilde{f}(\omega)e^{i\omega x}\,d\omega \tag{A.21}$$

$$\phi(x,y,z) = \frac{1}{2\pi}\int_0^{\infty}\int_{-\pi}^{\pi}\widetilde{\phi}(k,\theta,z)\mathrm{e}^{ik(x\cos\theta+y\sin\theta)}\,d\theta dk \tag{A.22}$$

Next, a solution is found for the conservation of mass, Equation A.11, and the boundary in Equation A.14 that states that the vertical velocity at infinite depth is zero. The Fourier transform of ϕ_0 should have the form shown in Equation A.23 to satisfy these two conditions.

$$\widetilde{\phi}_0 = A_0(k,\theta)\mathrm{e}^{kz} \tag{A.23}$$

Wehausen and Laitone [36] state that the inverse Fourier transform $\mathscr{F}^{-1}(\frac{1}{\widetilde{r}(k,\theta,z)})$, where $r(x,y,z) = \sqrt{x^2+y^2+z^2}$, is as given in Equation A.24. By hanging the input of the function $\frac{1}{r(x,y,z)}$ to $\frac{1}{r(x-a,y-b,z-c)}$,the Fourier transform for the distance between source point $\vec{\xi}(a,c,b)$ and point $\vec{x}$ is described and thus our interest. Using the definition of an inverse Fourier transform as described in Equation A.22, $\frac{1}{\widetilde{r}(k,\theta,z)}$ can then be determined of which the result is shown in Equation A.25.

$$\frac{1}{r(x,y,z)} = \frac{1}{\sqrt{x^2+y^2+z^2}} = \frac{1}{2\pi}\int_0^\infty \int_{-\pi}^{\pi} \mathrm{e}^{-k|z|}\mathrm{e}^{ik(x\cos\theta+y\sin\theta)}\,d\theta\,dk \tag{A.24}$$

$$\frac{1}{\widetilde{r}(k,\theta,z)} = \mathrm{e}^{-k|z-c|}\mathrm{e}^{-ik(a\cos\theta+b\sin\theta)} \tag{A.25}$$

The unknown function $A_0(k,\theta)$ can now be determined by substituting $\widetilde{\phi}_0 + \widetilde{r}^{-1}$ in the Fourier transform of the free surface boundary condition in Equation A.12. The result, Equation A.26, can be implemented in Equation A.23 and substituted into Equation A.22, resulting in Equation A.27.

$$A_0(k,\theta) = \frac{k+K}{k-K}e^{kc}e^{-ik(a\cos\theta+b\sin\theta)} \tag{A.26}$$

$$\phi_0(x,y,z) = \frac{1}{2\pi}\int_0^\infty \int_{-\pi}^{\pi} \frac{k+K}{k-K}\mathrm{e}^{k(z+b)}\mathrm{e}^{ik[(x-a)\cos\theta+(y-c)\sin\theta]}\,d\theta\,dk \tag{A.27}$$

The integrand of $\phi_0(x,y,z)$ has a singularity when $k=K$ thus has to be redefined to make it meaningfull. Therefore, the integral is interpretted as a Cauchy principal value. Wehausen and Laitone [36] state that the second equation in Equation A.28 can be derived by suitibly modifying Equation A.24.

$$\begin{aligned}\phi_1(x,y,z) &= \frac{1}{r} + \frac{1}{2\pi}\mathrm{PV}\int_0^\infty \int_{-\pi}^{\pi} \frac{k+K}{k-K}\mathrm{e}^{k(z+b)}\mathrm{e}^{ik[(x-a)\cos\theta+(y-c)\sin\theta]}\,d\theta\,dk \\ &= \frac{1}{r} + \frac{1}{r_1} + \frac{K}{\pi}\mathrm{PV}\int_0^\infty \int_{-\pi}^{\pi} \frac{1}{k-K}\mathrm{e}^{k(z+b)}\mathrm{e}^{ik[(x-a)\cos\theta+(y-c)\sin\theta]}\,d\theta\,dk\end{aligned} \tag{A.28}$$

The implementation of polar coordinates the allows to rewrite Equation A.28 into Equation A.29. The only difference with the Green's function as given in the WAMIT manual [34], Equation A.30, is that it seems that the principle value term is replaced by a derivation by π. In both the literature behind WAMIT and the work by Wehausen and Laitone [36] no reason could be found why this can be done. This step as well as the simplification in Equation A.28 are beyond the author's mathematical knowledge.

$$\phi_1(x-a,y-c,z-b) = \frac{1}{r} + \frac{1}{r_1} + 2K\mathrm{PV}\int_0^\infty \frac{\mathrm{e}^{k(z+b)}}{k-K}J_0(kR)\,dk. \tag{A.29}$$

$$G(\vec{x},\vec{\xi}) = \frac{1}{\sqrt{(x-\xi)^2+(y-\eta)^2+(z-\zeta)^2}} + \frac{1}{\sqrt{(x-\xi)^2+(y-\eta)^2+(z+\zeta)^2}} + \frac{2K}{\pi}\int_0^\infty \frac{e^{k(z+\zeta)}}{k-K}J_0(kR)\,dk \tag{A.30}$$

Lastly, in the paper by Wehausen and Laitone [36], a derivation is shown in which the radiation boundary condition far from the body is satisfied. This boundary condition is represented in Equation A.15. The resultant, complete, function for Φ is given in Equation A.31 and has the form of Equation A.18

$$\begin{aligned}\Phi(x,y,z,t) &= \left[\frac{1}{r} + \mathrm{PV}\int_0^\infty \frac{k+K}{k-K}\mathrm{e}^{k(z+b)}J_0(kR)\,dk\right]\cos\omega t + 2\pi K\mathrm{e}^{K(z+b)}J_0(KR)\sin\omega t \\ &\text{Where}\quad K = \omega^2/g\end{aligned} \tag{A.31}$$

Computing forces and hydrodynamic coefficients from potentials

The conversion to hydrodynamic coefficients and wave load can be made when the source strengths of the potentials are known using the diffraction theory. These potentials have been computed using the Green's function. A force can be determined using the potential by integrating the pressure over the body surface. The pressure on the body can be determined using Bernoulli's law. The linear unsteady pressure is shown in Equation A.32. In which p is the pressure and ρ the density.

$$p = -\rho\frac{\partial\phi}{\partial t} \tag{A.32}$$

Forces can then be determined using a pressure integration as presented in Equation A.33. In this formula, F and M represent the force and moment, $\hat{n}$ is the normal vector and $\hat{r}$ the location vector of the analysed part of the hull. S_b is the mean wetted body surface.

$$\begin{aligned} F &= -\iint_{S_b} (p \cdot \hat{n}) dS_b \\ M &= -\iint_{S_b} p \cdot (\hat{r} \times \hat{n}) dS_b \end{aligned} \tag{A.33}$$

The wave loads can directly be determined form the pressure integration of the diffraction and incident wave potential. The added mass and damping coefficient are related to the real and imaginary part of the radiation force. It can be redirected that the hydrodynamic coefficients can be calculated using Equation A.34. In this formula ϕ_{rj} is the radiation potential in direction j. For example, added mass a_{ij} represents the added mass in direction i due to a radiation force in direction j.

$$\begin{aligned} a_{ij} &= -\mathrm{Re}\left[\rho \iint_{S_b} \phi_{rj} \cdot \hat{n}_i \cdot dS\right] \\ b_{ij} &= -\mathrm{Im}\left[\rho\omega \iint_{S_b} \phi_{rj} \cdot \hat{n}_i \cdot dS\right] \end{aligned} \tag{A.34}$$

B

Model test details

In this section drawings and details of the model used in the model tests are given. First a couple of drawings are shown, followed by pictures of the realised model. The final drawings of the model are made by Jasper den Ouden.

Drawings

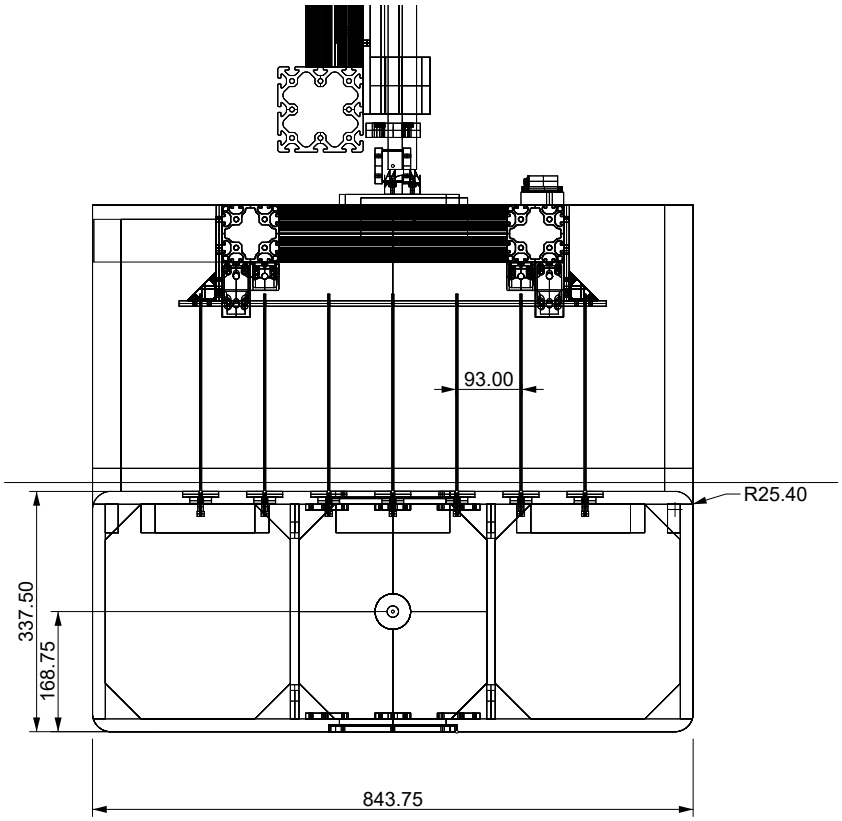

Figure B.1: Side views of the model

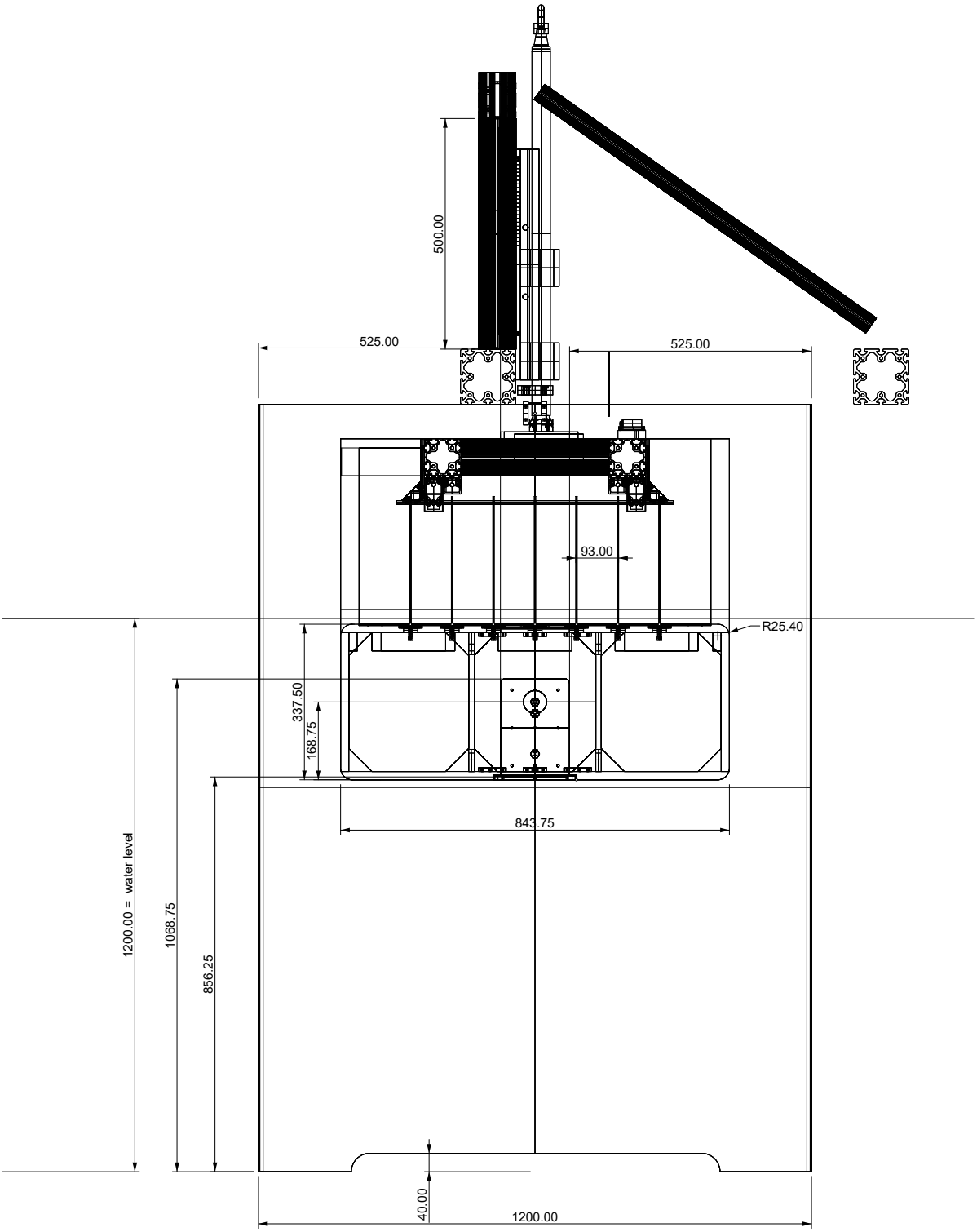

Figure B.2: Side view the model including side plates and structure on top of the tank

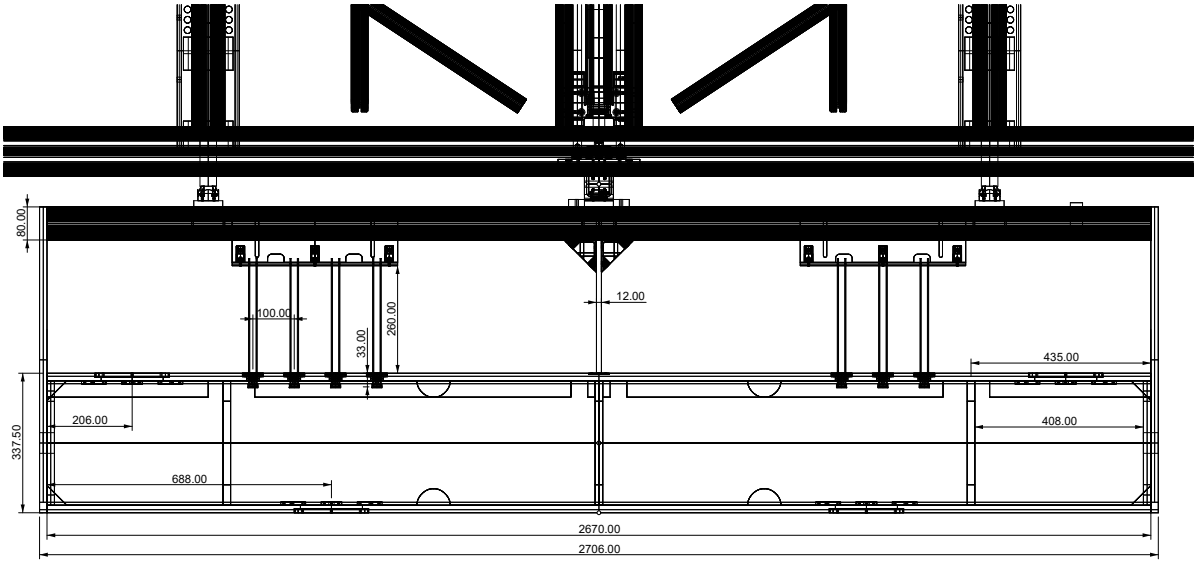

Figure B.3: Front view of the model

Pictures

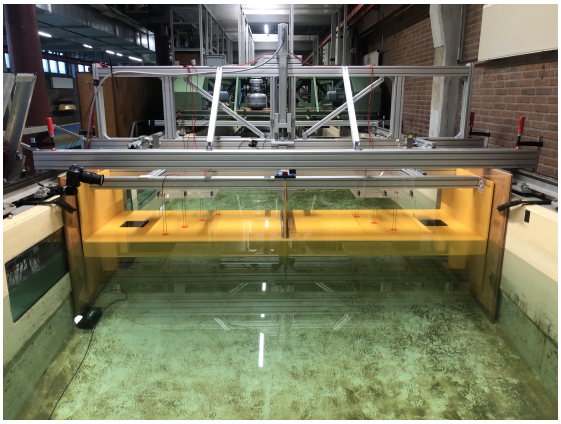

Figure B.4: Overview of setup during pitch tests, shot from wave maker side

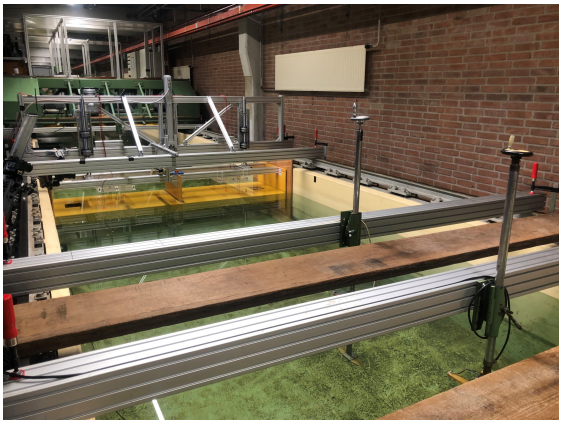

Figure B.5: Overview of setup during wave load tests including two external surface elevation senors, shot from wave maker side

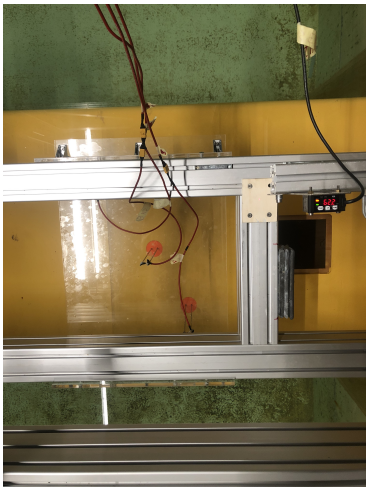

Figure B.6: Top view of surface elevation sensors on top of model (orange), laser can be seen at right side as well as additional weight to compensate the tilt of the model

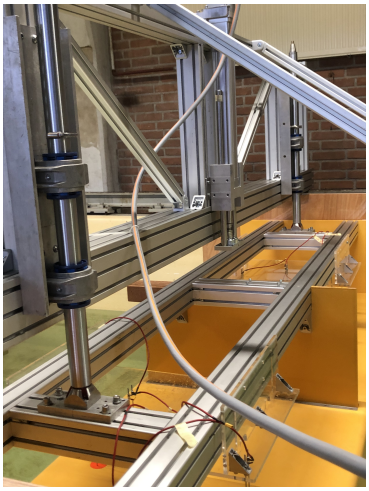

Figure B.7: Clear view of the actuator and linear guides during installation

Figure B.8: The large plates located at the side

Figure B.9: Gap between the model and the side, approximately equal to 6 mm at each side

Figure B.10: Hatch with transparent lid at top of the picture. Two of these hatches located at floater top, two at bottom

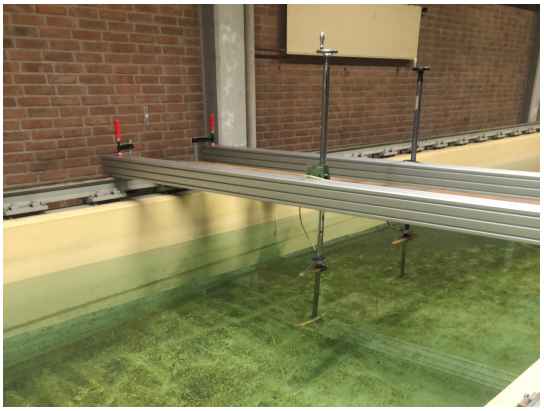

Figure B.11: Two of the three external surface elevation sensors

C

Pendulum tests

Pendulum tests have been performed in collaboration with Jasper den Ouden. The used method is originally worked out by Jasper. In Figure C.1, an overview of the test setup can be seen. First the center of gravity of the setup should be determined, then the pendulum test can be performed.

To determine the center of gravity of the model, a heeling test has been performed. During this tests, a mass is placed on the model such that it starts tilting. Then, the rotation is measured from which the center of gravity can be determined. On top of one of the hinges, a laser is placed to measure the displacement with the help of a ruler on the wall as shown in Figure C.2. The distance between the laser and the ruler on the wall, L_{angle}, was 1.611 m. The mass of the model including 2.36 kg for the two hinges, is 151.46 kg. The vertical length, Hinge_K, from the center of rotation during the pitch tests to the hinge was 0,701 m.

As can be seen on Figure C.3. Mass is added near the point of application of the oscillator during pitch tests. The horizontal distance L_{mass} from the center of rotation to point of application and the vertical distance b between the point of application and hinge are also shown on the figure. The heeling mass, is the mass applied at the point of application and will vary during the tests. In Table C.1, all data related to this test is given, The vertical height H1 is the initial measurement of the laser and vertical H2 is the height of the laser at the wall when the heeling mass is applied.

By using trigonometry, Equation C.1 to determine the heeling angle is determined. As well, Equation C.2 can be derived to calculate the distance between the hinge and center of gravity, Hinge_G'. A prime indicates that the value still includes the weight of the hinges. Lastly, the KG'_{model} is determined using Equation C.3.

Figure C.1: Overview of setup for the pendulum tests

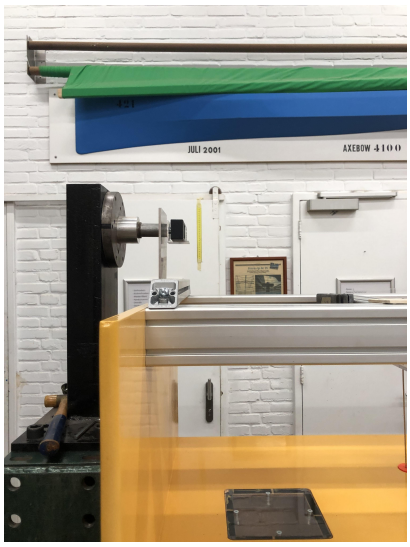

Figure C.2: Close up of the hinge at which the laser for measurements was attached

Table C.1: Heeling test data

Heeling tests					
Axis	Y-Y				[-]
Mass model'	151.46				[kg]
$Hinge\_K$	0.701				[m]
Heeling mass	3.913	5.913	7.913	12.913	[kg]
L_{mass}	0.530	0.530	0.530	0.530	[m]
b	0.280	0.280	0.280	0.280	[m]
L_{angle}	1.611	1.611	1.611	1.611	[m]
H1	0	0	0	0	[m]
H2	-0.043	-0.064	-0.085	-0.136	[m]
α	1.53	2.27	3.02	4.83	[deg]
$Hinge\_G'$	0.506	0.510	0.510	0.511	[m]
KG'_{model}	0.195	0.191	0.191	0.190	[m]

Table C.2: Pendulum test data

Pendulum tests		
Axis	Y-Y	[-]
10 oscillations	17.8	[sec]
10 oscillations	17.8	[sec]
10 oscillations	17.8	[sec]
T	1.78	[sec]
Hinge_G'	0.509	[m]
I_{yy}_model'	60.73	$[kgm^2]$
I_{yy}_model	21.45	$[kgm^2]$

$$\alpha = \tan^{-1}\left(\frac{H2 - H1}{L_{angle}}\right) \tag{C.1}$$

$$Hinge\_G' = \frac{\text{Heeling mass} \cdot ((L_{mass}\cos(\alpha) - b\sin(\alpha))}{\text{Mass model'} \cdot \sin(\alpha)} \tag{C.2}$$

$$KG'_{model} = Hinge\_K - Hinge\_G' \tag{C.3}$$

Now the pendulum tests can be performed. The heeling mass is removed and the model is at $\alpha = 0$. From here, the model is pushed such that it starts oscillating. In total three times the time has been measured that it takes to reach 10 oscillations. The results are shown in Table C.2. From these results the average oscillation period T has been determined.

The moment of inertia in the hinges is then determined using Equation C.4. In this formula the average value for Hinge_G' is used. The moment of inertia in the center of gravity can then be calculated using the Steiner rule, as shown in Equation C.5. The final step is to include the mass of the water in the model and exclude the hinges that were added to execute this test.

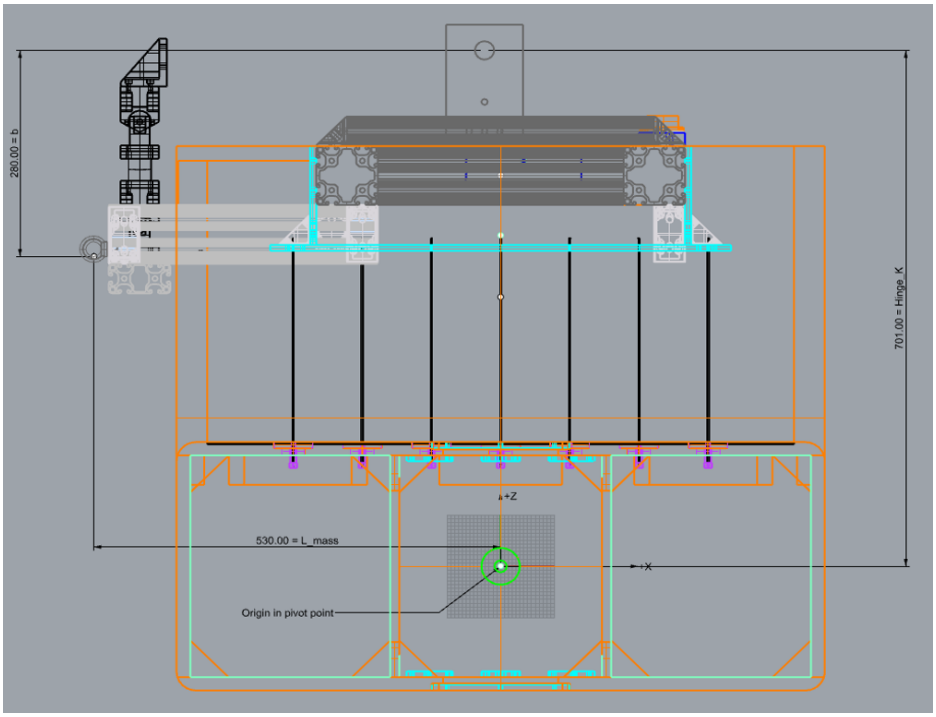

Figure C.3: Dimensions between the center of rotation, hinge and point of application for heeling mass, required for the heeling test

$$I_{yy}\_model' = \left(\frac{T}{2\pi}\right)^2 \cdot \text{Mass model'} \cdot g \cdot Hinge\_G' \tag{C.4}$$

$$I_{yy}\_model = I_{yy}\_model' - (\text{Mass model'} \cdot (Hinge\_G')^2) \tag{C.5}$$

The mass moment of inertia in the center of gravity is found to be 21.45 kgm^2. The center of gravity is located 21 mm horizontally towards the point of application of the heeling mass and 190 mm above the center of rotation. Applying the Steiner rule once again, it can be found that the moment of inertia in the center of rotation is 27.08 kgm^2. In Table C.3, the data for the objects which should be added or subtracted from the moment of inertia in the center of gravity to ultimately get the moment of inertia in the center of rotation during pitch tests. The negative masses represent that the weight not present during pitch forced oscillation tests. The data for the water has been determined in Rhinoceros, the computed mass moment of inertia for the water is 39.11 kgm^2 . Finally, when using the Steiner rule it can be calculated that the mass moment of inertia in the center of rotation during pitch tests was 65.33 kgm^2.

Table C.3: Mass and center of gravity for objects for which moment of inertia should be adjusted, measured from the center of rotation

Object:	mass [kg]	x_g [m]	y_g [m]	z_g [m]
Model	151.46	-0.021	0.00	0.19
Hinges	-1.76	-0.004	0.00	0.603
Brackets to connect hinges	-0.51	0.000	0.00	0.584
Water	618.26	0.000	0.00	0.000
Sum	767.45	-0.0041	0.00	0.03606

D

Graphical representation of experimental and numerical data

In this appendix the resultant graphs including both experimental and numerical data are given without a limited range. The data figure for RAO has already been given in the main body, thus is not repeated in this appendix.

Heave hydrodynamic coefficients

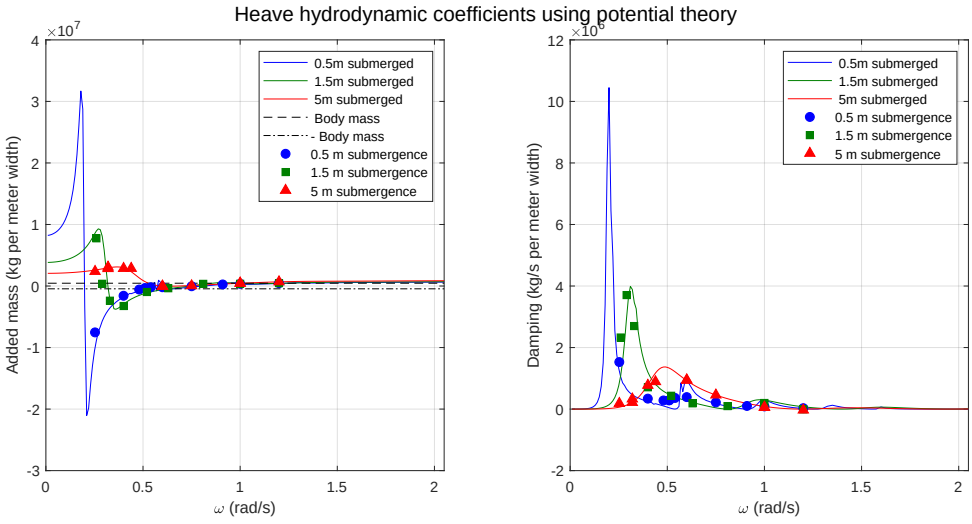

Figure D.1: Heave hydrodynamic coefficients, experimental results are displayed with markers, and numerical results using potential theory are displayed with solid lines

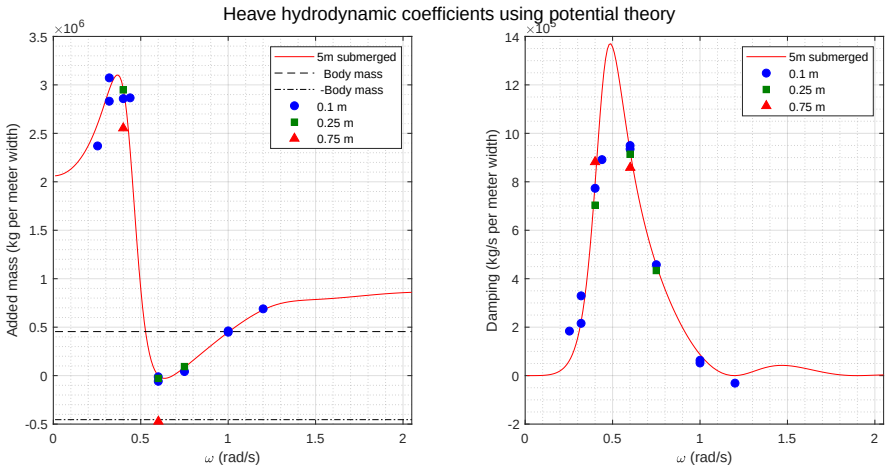

Figure D.2: Heave hydrodynamic coefficients at a submergence of 5 m, including the experimental results with a larger amplitude

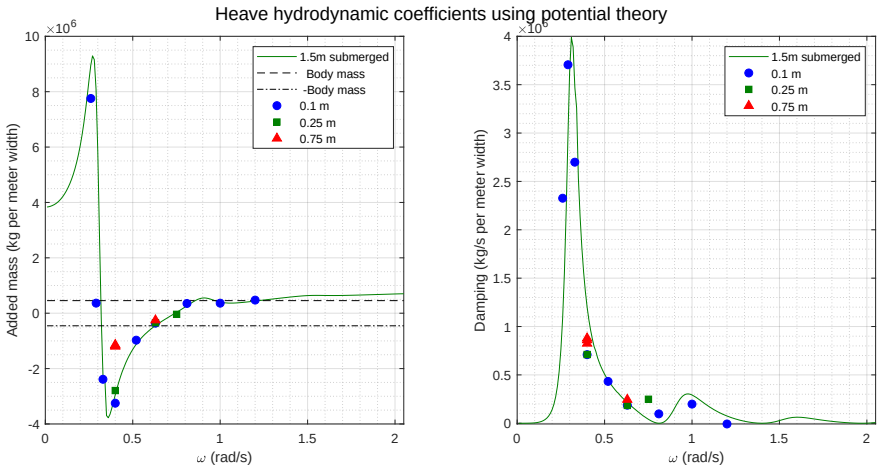

Figure D.3: Heave hydrodynamic coefficients at a submergence of 1.5 m, including the experimental results with a larger amplitude

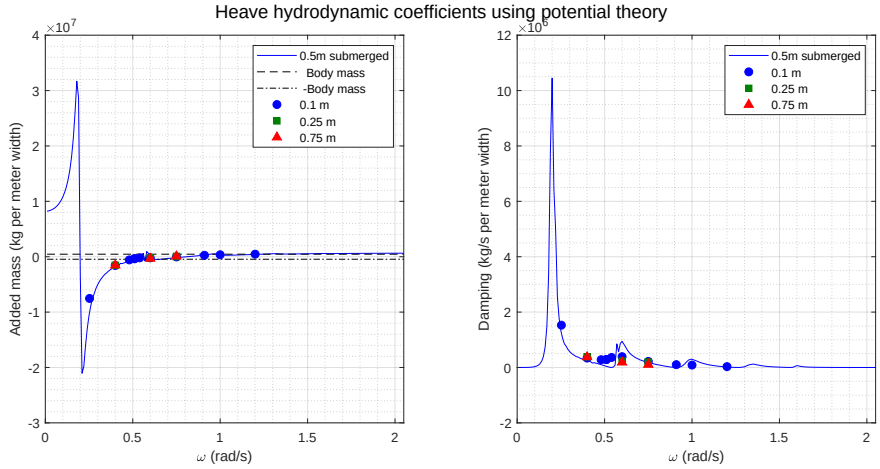

Figure D.4: Full scale heave hydrodynamic coefficients at a submergence of 0.5 m, including the experimental results with a larger amplitude

Pitch hydrodynamic coefficients

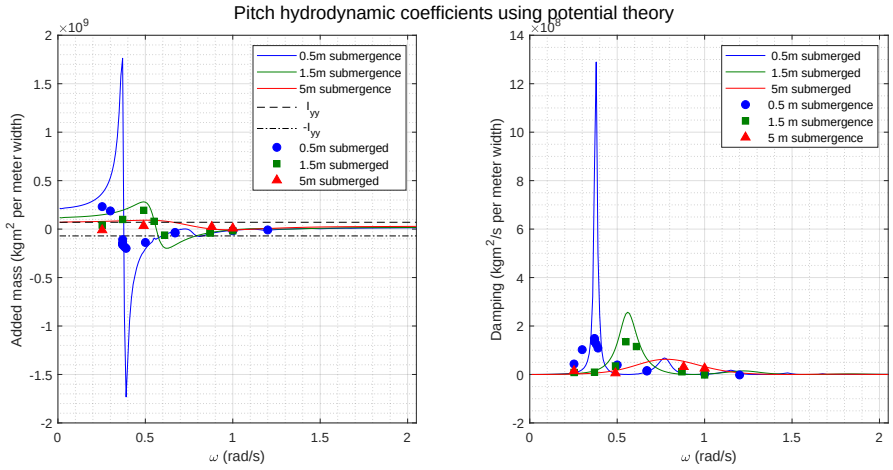

Figure D.5: Heave hydrodynamic coefficients, experimental results are displayed with markers, and numerical results using potential theory are displayed with solid lines

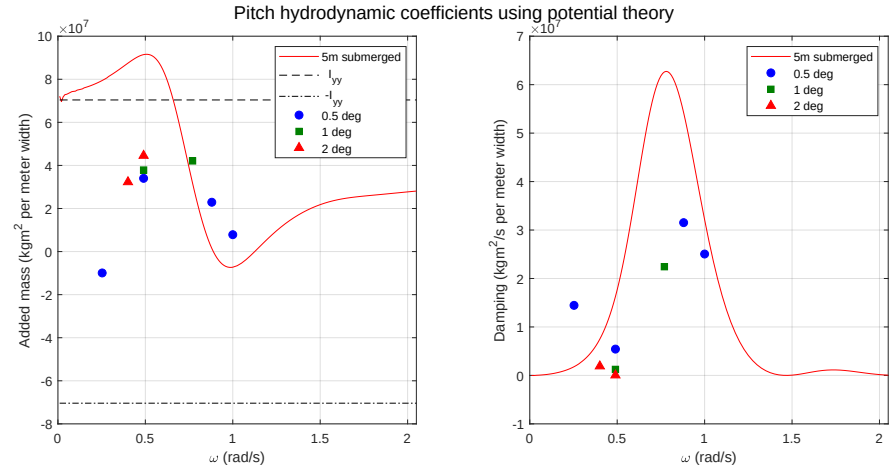

Figure D.6: Pitch hydrodynamic coefficients at a submergence of 5 m, including the experimental results with a larger amplitude

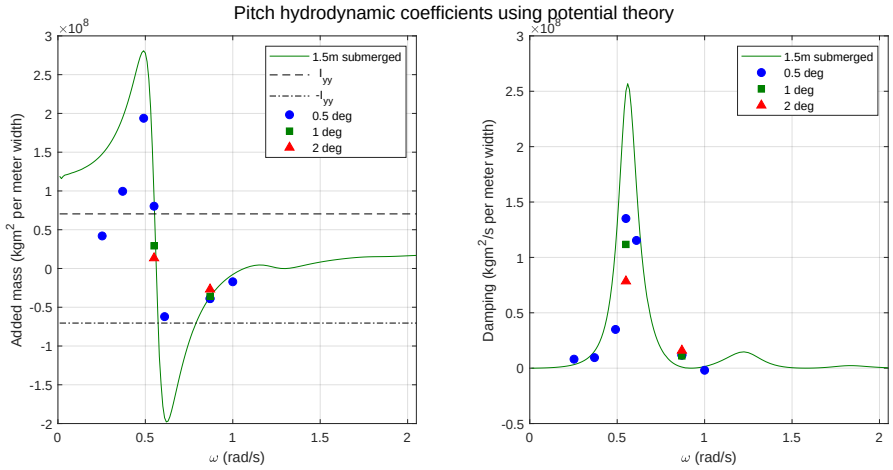

Figure D.7: Pitch hydrodynamic coefficients at a submergence of 1.5 m, including the experimental results with a larger amplitude

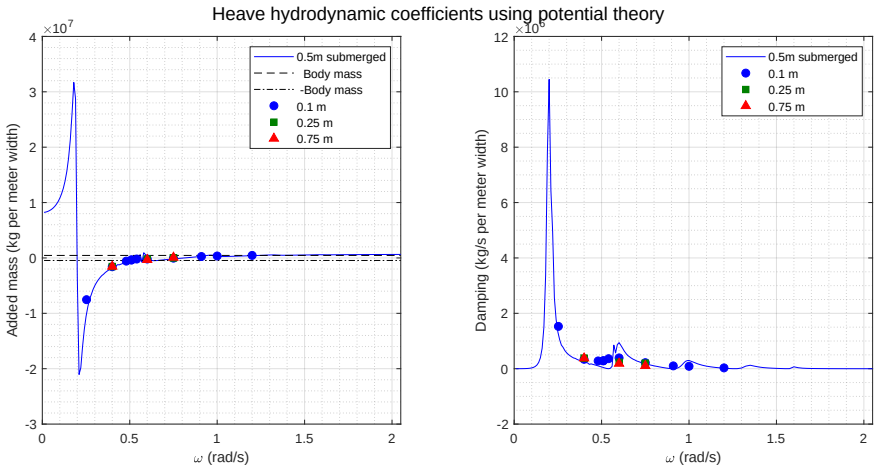

Figure D.8: Pitch hydrodynamic coefficients at a submergence of 0.5 m, including the experimental results with a larger amplitude

Wave loads

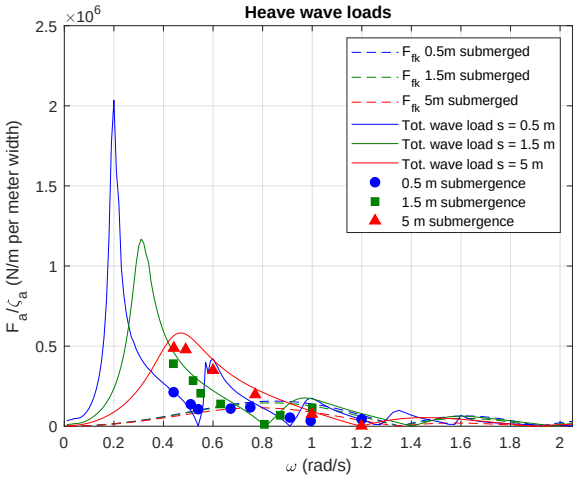

Figure D.9: Full scale heave wave loads over submergence range, including the experimental results with a larger amplitude

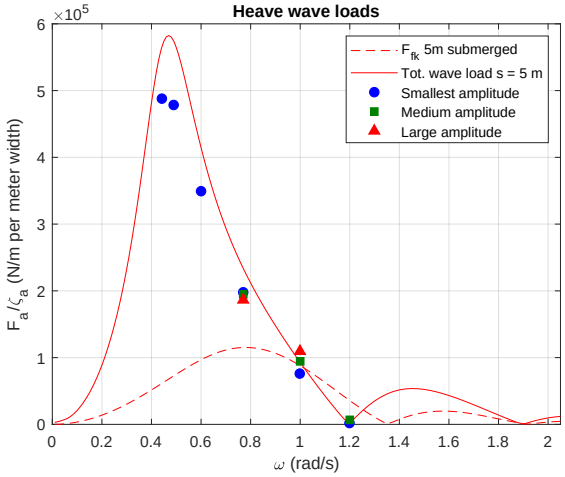

Figure D.10: Full scale heave wave loads at a submergence of 5 m, including the experimental results with a larger amplitude

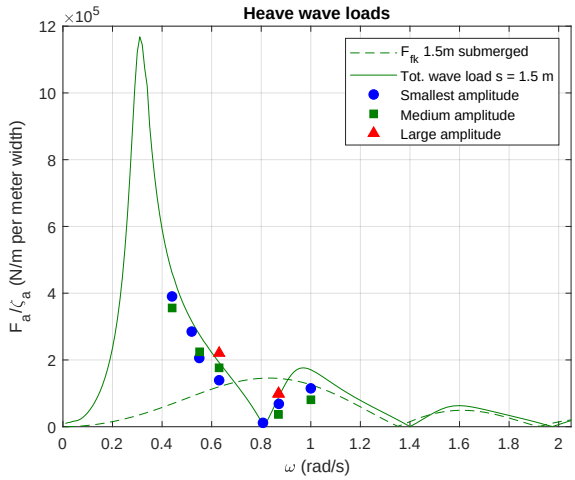

Figure D.11: Full scale heave wave loads at a submergence of 1.5 m, including the experimental results with a larger amplitude

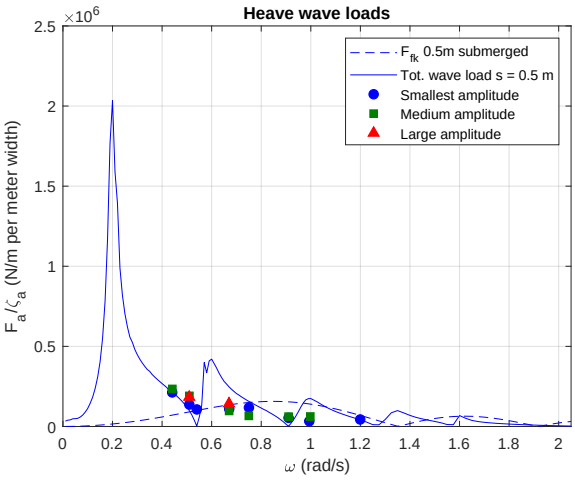

Figure D.12: Full scale heave wave loads at a submergence of 0.5 m, including the experimental results with a larger amplitude

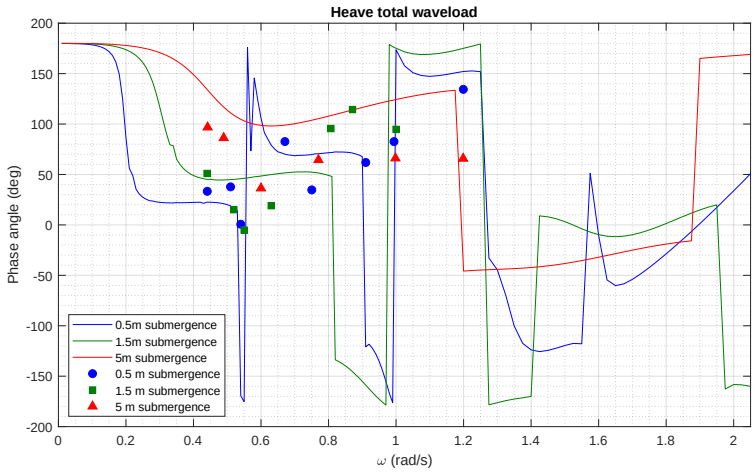

Figure D.13: Comparison of the phase angles of the experimental data with the phase angles over frequency domain for the full scale numerical data